Stony Brook University

Tau Neutrino Appearance via Neutrino Oscillations in Atmospheric Neutrinos

A Dissertation Presented

by

Tokufumi Kato

to

The Graduate School

in Partial Fulfillment of the

Requirements

for the Degree of

Doctor of Philosophy

in

Physics

Stony Brook University

May 2007

Stony Brook University

The Graduate School

Tokufumi Kato

We, the dissertation committee for the above candidate for the Doctor of Philosophy degree, hereby recommend acceptance of the dissertation.

Dr. Chang Kee Jung
Advisor
Professor of Physics and Astronomy
Stony Brook University

Dr. Maria Concepcion Gonzalez-Garcia
Chairperson of Defense
Associate Professor of Physics and Astronomy
Stony Brook University

Dr. Thomas C. Weinacht
Assistant Professor of Physics and Astronomy
Stony Brook University

Dr. Walter Toki
Professor of Physics
Colorado State University

This dissertation is accepted by the Graduate School.

Lawrence Martin
Dean of the Graduate School

Abstract of the Dissertation

Tau Neutrino Appearance via Neutrino Oscillations in Atmospheric Neutrinos

by

Tokufumi Kato

Doctor of Philosophy

in

Physics

Stony Brook University

2007

A search for the appearance of tau neutrinos from $\nu_\mu \leftrightarrow \nu_\tau$ oscillations in the atmospheric neutrinos has been conducted using the atmospheric neutrino data from the Super-Kamiokande-I and the Super-Kamiokande-II experiment. A tau neutrino enriched event sample is selected by using the event topologies of the decay of tau leptons produced in charged-current weak interactions. An excess of tau neutrino signals is observed, and a best-fit tau neutrino appearance signal of 162 ± 59 (stat.) $^{+21}_{-56}$ (sys.), which disfavors the no tau neutrino appearance hypothesis by 2.1 sigma. This is consistent with the expected number of tau neutrino events, 121 ± 39 (sys.) for $\Delta m^2 = 2.4 \times 10^{-3}\mathrm{eV}^2$, assuming the full mixing in $\nu_\mu \leftrightarrow \nu_\tau$ oscillations. The Super-Kamiokande atmospheric neutrino data are consistent with tau neutrino appearance from $\nu_\mu \leftrightarrow \nu_\tau$ oscillations.

Dedicated to my parents.

Contents

List of Figures

List of Tables

Acknowledgements

After spending six years in graduate school, I owe a debt of gratitude to many people. Without their support, this thesis could never have reached completion.

First, I would like to thank my advisor, Chang Kee Jung. I have been his student for a long time. I came to Stony Brook as a sophomore student and soon joined his research group (Stony Brook Nucleon decay and Neutrino (NN) Group). Chang Kee gave me a great opportunity to work on both Super-Kamiokande and K2K experiments. In my senior year when I was considering which graduate schools to apply for, Chang Kee kindly asked me if I would have wanted to stay in Stony Brook for graduate study. Because a thesis experiment (Super-Kamiokande) was very interesting and because I was sure that it would have been hard to find a better advisor than Chang Kee, I decided to stay and continued working in Chang Kee's group. I must say how lucky I am to have been working with Chang Kee. He gave me his advice not only to be a good physicist but also to be a fine person. Chang Kee's dedication to physics and education, vision, care, patience, and criticism is simply something I give a great respect for and something I strive for.

I owe a large debt to Clark McGrew. He has directly helped me with my analysis work since Clark is the one who originally started tau neutrino appearance analysis at Super-K. I would like to thank Clark for invaluable discussions on physics as well as statistics with his unique humor.

Besides Chang Kee and Clark, I also want to thank the other members of the NN group, Chiaki Yanagisawa, Peter Paul, Antony Sarrat and Kenkou Kobayashi for their help and guidance. Although I did not spent much time together, I would like to thank the former NN group students; Brett Viren, Eric Sharkey, Christopher Mauger, Matthew Malek, and Markus Ackerman for their assistant and advice. Brett was my mentor, who taught me particle physics and Linux with great patience. I was very happy to have had him when I joined the NN group without any knowledge about doing research in particle physics or computer skills. I thank my fellow NN group students who joined the NN group after me; Ryan Terri, Lisa Whitehead, Le Phuoc Trung,

Glenn Lopez, and Dima Beznosko for their friendship and good memories from the nights when we went out for a few drinks.

I am happy to have Concha Gonzalez-Garcia, Tom Weinacht, and Walter Toki as committee members. They gave me good feedbacks and comments, which were incorporated into this thesis. I thank Walter for flying from Colorado to NY to be at my defense.

I am grateful to our spokesperson of the Super-Kamiokande experiment, Yoichiro Suzuki for showing his leadership. I was in the atmospheric neutrino (ATMPD) group, which has been led by Takaaki Kajita and Ed Kearns. With their generous effort, this group is well organized, and physics analyses have been conducted smoothly.

I would like to thank all of the members in the tau neutrino appearance analysis group; Takaaki Kajita, Ed Kearns, Chang Kee Jung, Clark McGrew, Chris Walter, and Choji Saji for numerous invaluable discussions and their guidance as well as their great contributions to this thesis. Working in this group has been a pleasure. In particular, I have worked very closely with Choji Saji on the analysis and would like to thank him for his help with endless patience. We became good friends and went snowboarding together many times.

I would also like to sincerely thank Masato Shiozawa and Yusuke Koshio for important discussions as well as their technical support. I have been benefitted very much from those discussions. I would like to thank Shoei Nakayama and Masaki Ishitsuka for their great help on Super-K software and their friendship. I would have had much more difficult time in my analysis work without their support. I also want to thank Masayuki Nakahata, Bill Kropp, Kenji Kaneyuki, Shigetaka Moriyama, Yasuo Takeuchi, Mark Vagins, Makoto Miura, Kimihiro Okumura, Yoshinari Hayato, Yoshihisa Obayashi, Jun Kameda, Itaru Higuchi, Seo Hyun Kwan, Yumiko Takenaga for their assistance.

I have spent a good amount of time at Super-K working with graduate students from other US institutions. I would like to give my thanks to Parker Cravens from UCI, Wei Wang and Aaron Herfurth from BU, Yosh Shiraishi from UW for their friendship and companion. While I was staying at Super-K for a long time, Parker and I often went to Izakaya for beer.

Also, I would like to express my gratitude to Peter Kahn, who is a professor at Stony Brook. Peter originally introduced Chang Kee to me before I joined the NN group. Peter has e-mailed me once in a while to find out how I was doing and took me out for lunch when I was in Stony Brook.

Although they did not contribute to this thesis directly, I would like to thank all of my friends in Stony Brook. Without them, my graduate life would have been really boring.

I would like to thank administrative staff, Joan Napolitano and Alice Dugan in the Stony Brook High Energy Group, Pat Peiliker and Diane Siegel in the department of Physics and Astronomy, and Kiyoko Hirose, Eri Okada, and Yukari Maeda in Super-K. I am grateful for their help.

Finally, I must give my thanks to my family. I wish to thank Keishi Kato for his advice and support as my father and as a scientist. I decided to study physics because of his influences. I would also like to thank my mother, Yoko Kato for her sacrifices and support. Without their encouragement and trust, I could never have made through graduate school and come to this point. Thank you very much.

Chapter 1

Introduction

1.1 Neutrinos

Neutrinos are everywhere and are one of the most common particles around us, yet we know the least about them. This elusive particle comes from many different sources, such as human body via the β-decay of ^{40}K to ^{39}K, natural radioactive materials on the Earth, nuclear reactors around the world, the upper atmosphere of the Earth, the Sun, and the Universe (e.g. Supernovae and the Big Bang). Although neutrinos are abundant in nature, they were only first postulated theoretically by Wolfgang Pauli in 1930 [1]. In β-decay, the measured energy spectrum of the emitted electrons was continuous instead of the expected monoenergetic distribution in two body decay. This observation seemed to violate the law of energy conservation. As a solution to the problem, Pauli proposed that there could exist another neutral particle emitted in β-decay, which carried away the missing energy and made the electron energy spectrum continuous. He wrote his famous letter, "Liebe Radioaktive Damen und Herren (Dear Radioactive Ladies and Gentlemen"to the Tubingen congress on 4th December 1930.

> Dear Radioactive Ladies and Gentlemen,
>
> As the bearer of these lines, to whom I graciously ask you to listen, will explain to you in more detail, how because of the "wrong" statistics of the N and ^{6}Li nuclei and the continuous beta spectrum, I have hit upon a desperate remedy to save the "exchange theorem" of statistics and the law of conservation of energy. Namely, the possibility that there could exist in the nuclei electrically neutral particles, that I wish to call neutrons[1], which have spin 1/2

[1]This is what he called the neutrino when he first came up with the idea. The

> and obey the exclusion principle and which further differ from light quanta in that they do not travel with the velocity of light. The mass of the neutrons should be of the same order of magnitude as the electron mass and in any event not larger than 0.01 proton masses. The continuous beta spectrum would then become understandable by the assumption that in beta decay a neutron is emitted in addition to the electron such that the sum of the energies of the neutron and the electron is constant...
>
> I agree that my remedy could seem incredible because one should have seen those neutrons very earlier if they really exist. But only the one who dare can win and the difficult situation, due to the continuous structure of the beta spectrum, is lighted by a remark of my honoured predecessor, Mr Debye, who told me recently in Bruxelles: "Oh, It's well better not to think to this at all, like new taxes". From now on, every solution to the issue must be discussed. Thus, dear radioactive people, look and judge. Unfortunately, I cannot appear in Tubingen personally since I am indispensable here in Zurich because of a ball on the night of 6/7 December. With my best regards to you, and also to Mr Back.
>
> Your humble servant
> . W. Pauli

Enrico Fermi named this particle the "neutrino" meaning a little neutral object in Italian represented by a Greek alphabet ν. The neutrino was incorporated in his successful theory of β-decay [3].

It took 25 years until the existence of neutrinos was verified experimentally. In 1956, the neutrino was discovered by Frederick Reines and Clyde L. Cowan [2, 4]. The experiment[2] took place at the Savannah River nuclear reactor in South Carolina, where the neutrinos were detected from the inverse β-decay reaction of the neutron :

$$p + \bar{\nu_e} \rightarrow n + e^+ \tag{1.1}$$

The detector consisted of a water tank with dissolved $CdCl_2$ surrounded by liquid scintillator. They detected the coincidence of gamma rays from pair

neutron that we now know was discovered by Chadwich in 1932. What we presently call neutron had not yet been discovered so the name was available for this use. Enrico Fermi later proposed the now accepted name of neutrino.

[2]Their first plan was to detect neutrinos emitted from a nuclear explosion.

annihilation of a positron and a subsequent gamma ray from the neutron capture. Reines was awarded the Nobel Prize in 1995 for this discovery.

In 1959, Bruno Pontecorvo postulated the existence of muon neutrinos (ν_μ) different from the neutrinos emitted in the β-decay of nuclei. In 1962, Leon Lederman, Melvin Schwartz and Jack Steinberger discovered muon neutrinos by detecting muons from the following interactions :

$$\nu_\mu + N \rightarrow \mu^- + X \tag{1.2}$$

using a neutrino beam at the Brookhaven National Laboratory (BNL). For their discovery, they were awarded the Nobel Prize in 1988. The discovery of the tau lepton (τ) in 1975 [5] implied the existence of the third family of neutrino, the tau neutrino (ν_τ). In 2000, the tau neutrino was directly observed by the DONUT experiment at the Fermi National Accelerator Laboratory (FNAL) as expected [6].

Discovery of the neutrinos from outer space followed the discoveries of three generations of neutrinos. In 1968, the neutrinos from the Sun were observed by Ray Davis and his collaboration [7]. The neutrinos from the supernova explosion SN1987a were observed by the Kamiokande [8, 9] and IMB [10, 11] experiments in 1987. Raymond Davis Jr. and Masatoshi Koshiba were awarded the Nobel Prize in 2002 for their discovery of cosmic neutrinos.

1.2 Neutrinos in the Standard Model

In the Standard Model of particle physics, all elementary particles are categorized into two groups: fermions and bosons. Among fermions, there are quarks and leptons, which come in three generations or flavors, and the bosons act as force mediators for strong, electromagnetic, and weak interactions as shown in Table 1.1. Neutrinos have three flavors : ν_e, ν_μ, and ν_τ and are paired with their corresponding charged lepton, the electron, the muon, and the tau. The number of light neutrino flavors are confirmed to be three by LEP experiment [12].

Since neutrinos are electrically neutral and colorless [3], they interact only through the weak force. There are two types of weak interactions: charged current (CC) and neutral current (NC) interactions. The force mediators for CC and NC interactions are the charged W and neutral Z bosons, respectively. Figure 1.1 shows example Feynman diagrams of the CC and NC interactions.

[3] Only quarks have color charges to participate in strong interactions.

Table 1.1: Table of elementary particles and forces in the Standard Model.

Particles	Flavor			Charge
Quark	u	c	t	$+\frac{2}{3}$
	d	s	b	$-\frac{1}{3}$
Lepton	e	μ	τ	-1
	ν_e	ν_μ	ν_τ	0

Force	Strong	Electromagnetic	Weak
Mediator	gluon	photon	W and Z

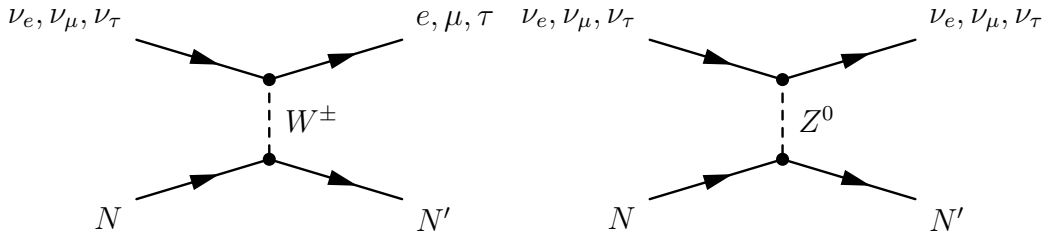

Figure 1.1: The feynman diagrams of the weak CC (left) and NC (right) interactions of neutrinos with a nucleon (N, N').

In the SM, neutrinos are considered to be massless. One implies that all neutrinos are left-handed and all anti-neutrinos are right-handed characterized by the helicity. Neutrino's helicity was measured by M. Goldhaber *et al.* [13].

1.3 Neutrino Mass and Neutrino Oscillations

Despite the masslessness of neutrinos in the SM, the mass of neutrinos have been questioned since Fermi developed his theory of neutrinos. Several experiments have attempted to measure the mass of ν_e, ν_μ, and ν_τ directly via β-decay, pion decay, and τ-lepton decay respectively, but were only successful to set the upper limits to $m_{\nu_e} < 2.2\,\text{eV}$ [14, 15], $m_{\nu_\mu} < 170\,\text{keV}$ [16], $m_{\nu_\tau} < 15.5\,\text{MeV}$ [17]. The mass of neutrinos is also constrained by cosmological observations, which put upper limits on the sum of neutrino masses $\sum m_\nu < 0.42\,\text{eV}$ [18].

Another way to probe neutrino mass is to search for neutrino oscillations. In 1957, B. Pontecorvo proposed an idea of neutrino oscillations between neutrinos and anti-neutrinos [19]. In 1962, Z. Maki, M. Nakagawa, and S. Sakata formulated a theory for neutrino flavor oscillation [20], and in 1967, Pontecorvo also developed a theory of neutrino oscillations [21]. If neutrinos have non-zero mass and their flavor eigenstates are not identical to their mass eigenstates, the neutrinos can change their flavor. This phenomenon is called neutrino oscillations.

The neutrino flavor eigenstate $|\nu_\alpha\rangle$ can be expressed as a superposition of the mass eigenstates $|\nu_i\rangle$ with a unitary mixing matrix, U, known as Maki-Nakagawa-Sakata (MNS) neutrino mixing matrix[4], which is analogous to the Cabibbo-Kobayashi-Maskawa (CKM) matrix for the quark sector. :

$$|\nu_\alpha\rangle = \sum_{i=1}^{3} U^*_{\alpha i} |\nu_i\rangle\,, \qquad \alpha \;=\; e, \mu, \tau. \tag{1.3}$$

Assuming that a neutrino is produced at time $t = 0$ in the state of ν_α in Eq. 1.3, the time evolution of neutrino flavor states can be given by :

$$|\nu_\alpha(t)\rangle = \sum_{i=1}^{3} U^*_{\alpha i} e^{-iE_i t} |\nu_i\rangle \tag{1.4}$$

Similarly, the neutrino in the state of ν_β is :

$$|\nu_\beta\rangle = \sum_{i=1}^{3} U^*_{\beta i} |\nu_i\rangle \qquad \text{or} \qquad |\nu_i\rangle = \sum_{i=1}^{3} U_{\beta i} |\nu_\beta\rangle \tag{1.5}$$

[4]The matrix U is also sometimes called PMNS matrix to include Pontecorvo.

then, $|\nu_\alpha(t)\rangle$ can be expressed in the basis of weak flavor $|\nu_\beta\rangle$:

$$|\nu_\alpha(t)\rangle = \sum_\beta \sum_{i=1}^{3} U_{\beta i}\, e^{-iE_i t}\, U^*_{\alpha i}\, |\nu_\beta\rangle \tag{1.6}$$

The amplitude of $\nu_\alpha \to \nu_\beta$ transitions at time t is :

$$\mathcal{A}_{\nu_\alpha \to \nu_\beta}(t) = \langle \nu_\beta | \nu_\alpha(t)\rangle = \sum_{i=1}^{3} U_{\beta i}\, e^{-iE_i t}\, U^*_{\alpha i} \tag{1.7}$$

The probability of $\nu_\alpha \to \nu_\beta$ transition is given by :

$$P_{\nu_\alpha \to \nu_\beta} = |\mathcal{A}_{\nu_\alpha \to \nu_\beta}(t)|^2 = \left| \sum_{i=1}^{3} U_{\beta i}\, e^{-iE_i t}\, U^*_{\alpha i} \right|^2 . \tag{1.8}$$

In the analysis presented in this thesis, the two flavor neutrino oscillations are assumed, where there are two mass eigenstates and two flavor eigenstates with a single mixing angle. In this assumption, the MNS matrix is written in terms of a mixing angle θ :

$$U = \begin{pmatrix} \cos\theta & \sin\theta \\ -\sin\theta & \cos\theta \end{pmatrix} \tag{1.9}$$

And, the flavor oscillation probability is given by :

$$P(\nu_\alpha \to \nu_\beta) = \sin^2 2\theta \sin^2 \left(\frac{1.27 \Delta m^2(\mathrm{eV}^2) L(\mathrm{km})}{E_\nu(\mathrm{GeV})} \right) \tag{1.10}$$

where θ is the neutrino mixing angle, $\Delta m^2 \equiv m_j^2 - m_i^2$ is the mass-squared difference of neutrino mass eigenstates in eV^2, L is the distance traveled by neutrinos in km, E_ν is neutrino energy in GeV, and the factor 1.27 comes from $1/\hbar c$ in the conversion of units to km and GeV. The survival oscillation probability $P(\nu_\alpha \to \nu_\alpha)$ is simply $P(\nu_\alpha \to \nu_\alpha) = 1 - P(\nu_\alpha \to \nu_\beta)$, that is :

$$P(\nu_\alpha \to \nu_\alpha) = 1 - \sin^2 2\theta \sin^2 \left(\frac{1.27 \Delta m^2(\mathrm{eV}^2) L(\mathrm{km})}{E_\nu(\mathrm{GeV})} \right) \tag{1.11}$$

Figure 1.2 shows the survival probability and oscillation probability as a function of L(km)/E(GeV).

The neutrino oscillation discussed in this thesis concerns $\nu_\mu \leftrightarrow \nu_\tau$ oscillations. Therefore, the flavor term is $(\alpha, \beta) = (\mu, \tau)$ and the mass term is $(i, j) = (2, 3)$ throughout the thesis unless mentioned specifically otherwise.

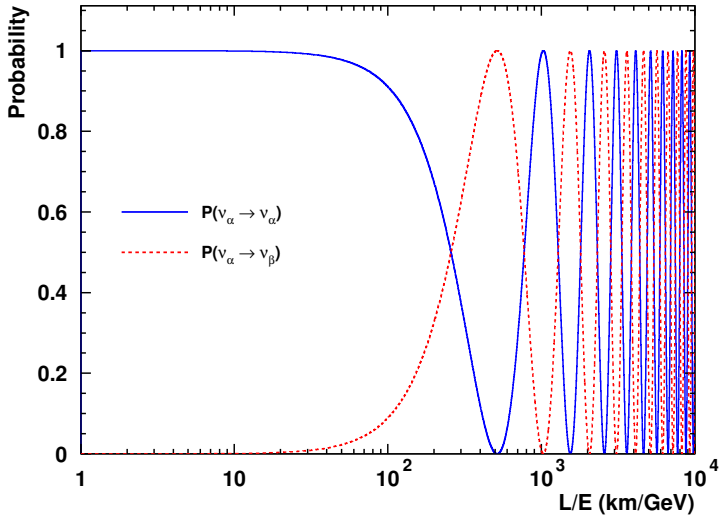

Figure 1.2: The survival $P(\nu_\alpha \rightarrow \nu_\alpha)$ (solid line) and oscillation $P(\nu_\alpha \rightarrow \nu_\beta)$ (dotted line) probability for $\sin^2 2\theta = 1$ and $\Delta m^2 = 2.4 \times 10^{-3}$ eV^{2}as a function of L(km)/E(GeV).

1.3.1 Detection of Neutrino Oscillations

The oscillation parameters, a mixing angle θ and the mass-squared difference Δm^2, are measured with known neutrino path length L and energy E in neutrino oscillation experiments (Eq. 1.10 and Eq. 1.11). If there is no mixing ($\theta = 0$) and/or (Δm^2 L/E) $\ll 1$, the oscillation probability becomes zero and hence nulling all oscillations.

There are two ways to detect neutrino oscillations of $\nu_\alpha \rightarrow \nu_\beta$. The first technique is to detect ν_β in a known neutrino flux of ν_α, which is known as the "appearance" of ν_β. For example, in a test of $\nu_\mu \leftrightarrow \nu_\tau$ oscillation hypothesis, ν_τ is detected in the ν_μ flux. Since neutrinos are observed by detecting the charged lepton produced in their CC interactions, they must have sufficient energy to produce the lepton. Thus, the energy of ν_τ must be greater than 3.5 GeV to produce τ-leptons through ν_τ interactions with a fixed target nucleon. We would then look for τ-lepton events.

The second technique is to observe "disappearance", where the detected neutrino flux of ν_α is less than the expected flux in the absence of oscillations. In the previous example of $\nu_\mu \leftrightarrow \nu_\tau$ oscillations, if the energy of ν_τ is less than the threshold of τ-lepton production, instead of the observation of ν_τ, the depletion of ν_μ would be an evidence for such oscillations.

As described in the next section, the positive signatures for the atmospheric neutrino oscillations of $\nu_\mu \leftrightarrow \nu_\tau$ was observed through ν_μ disappearance by various experiments. In this thesis, an analysis to search for ν_τ appearance is described in detail.

1.4 Atmospheric Neutrinos and Neutrino Oscillation Experiments

Using atmospheric neutrinos produced in the atmosphere of the Earth, several experiments have studied neutrino oscillations. In 1998, the first compelling evidence for neutrino oscillations was announced by the Super-Kamiokande collaboration [45]. The results from other experiments are also consistent with Super-K, and all observations favor $\nu_\mu \leftrightarrow \nu_\tau$ oscillations in the atmospheric neutrinos.

1.4.1 Atmospheric Neutrinos

Atmospheric neutrinos are produced through cascade of interactions originating from cosmic rays bombarding the atmosphere nuclei. When primary cosmic rays (mostly protons and helium) from the space travel through the atmosphere of the Earth, they interact with air nuclei such as nitrogen, oxygen, and carbon and create hadronic showers mostly consisting of pions ($\pi^\pm$). These pions decay into muons and muon-neutrinos. The muons then further decay into electrons and electron-neutrinos and muon-neutrinos :

$$\begin{aligned} \pi^+ &\rightarrow \mu^+ + \nu_\mu \\ &\quad \hookrightarrow e^+ + \nu_e + \overline{\nu}_\mu \end{aligned} \tag{1.12}$$

$$\begin{aligned} \pi^- &\rightarrow \mu^- + \overline{\nu}_\mu \\ &\quad \hookrightarrow e^- + \overline{\nu}_e + \nu_\mu \end{aligned} \tag{1.13}$$

The flavor ratio of muon-neutrinos to electron-neutrinos is defined as :

$$N_\mu / N_e = (\nu_\mu + \overline{\nu}_\mu)/(\nu_e + \overline{\nu}_e) \tag{1.14}$$

is expected to be approximately two. The more precise flavor ratio depends on the energy of muons and Kaons ($K^\pm$) produced in the hadronic showers. It is important to note that tau neutrinos produced in the atmosphere are negligible (see Section 4.1). The travel distance of atmospheric neutrinos to a underground detector varies from 15 km to 13,000 km depending on their production location as shown in Figure 1.3. It is related to a zenith angle, which

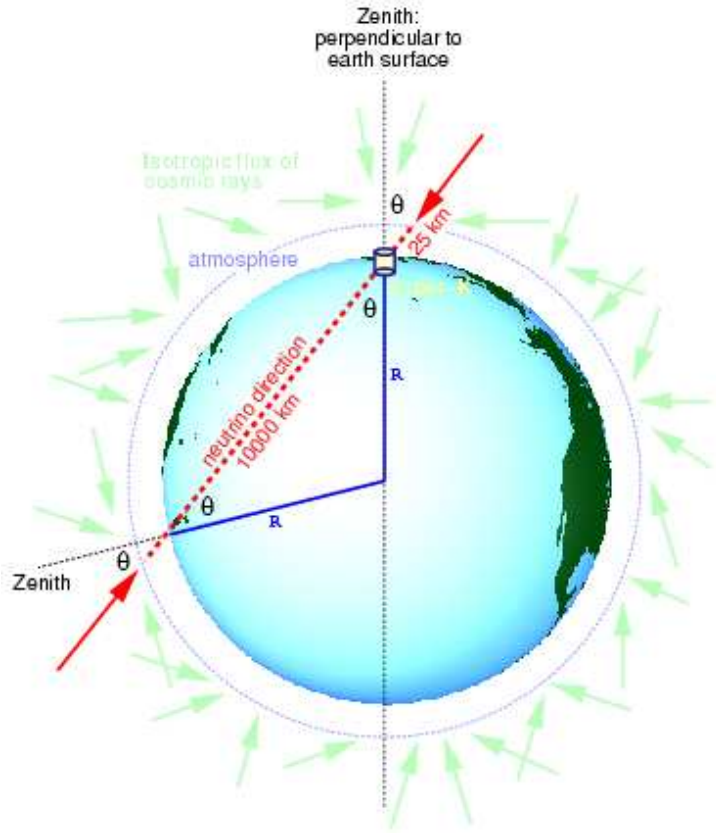

Figure 1.3: A schematic view of the atmospheric neutrino production. Cosmic rays hit the atmosphere of the Earth isotropically, and neutrinos are produced. Atmospheric neutrinos travel from 15 km to 13,000 km before reaching the surface of the earth.

is defined to be the angle between the neutrino direction and a line perpendicular to the ground. The cosine of a zenith angle, $\cos\theta = -1$ corresponds to the upward-going direction, $\cos\theta = 0$ to the horizontal direction, and $\cos\theta = +1$ to the downward-going direction. Further details of atmospheric neutrinos are described in Chapter 4.

1.4.2 Neutrino Oscillation Experiments

The first atmospheric neutrino experiments were two water Cherenkov experiments, Irvine-Michigan-Brookhaven (IMB) [22, 23] and Kamiokande [24, 25]. Although their primary scientific goals were to search for proton decay

Table 1.2: List of the flavor ratio $R(\mu/e)$ measured by various experiments.

Experiment	Method	Exposure (kt·year)	Flavor Ratio $R(\mu/e)$
IMB	Water Cherenkov	7.7	$0.54 \pm 0.05 \pm 0.012$ (Sub-GeV)
		2.1	$1.40\ ^{+0.41}_{-0.30} \pm 0.3$ (Multi-GeV)
Kamiokande	Water Cherenkov	7.7	$0.60\ ^{+0.06}_{-0.05} \pm 0.05$ (Sub-GeV)
		8.2	$0.57\ ^{+0.08}_{-0.07} \pm 0.07$ (Multi-GeV)
NUSEX	Iron Calorimeter	0.74	$0.96\ ^{+0.32}_{-0.28}$
Fréjus	Iron Calorimeter	1.56	$1.00 \pm 0.15 \pm 0.08$
Soudan-2	Iron Calorimeter	5.1	$0.68 \pm 0.11 \pm 0.06$
Super-K	Water Cherenkov	92	$0.658 \pm 0.016 \pm 0.05$ (Sub-GeV)
		92	$0.702\ ^{+0.032}_{-0.030} \pm 0.101$ (Multi-GeV)

and the atmospheric neutrinos were found to be their main "backgrounds", these backgrounds quickly became a topic of interest to study. Both experiments found the measured flavor ratio that was different from two. In practice, they measured the double ratio R of the observed flavor ratio (N_{Data}) to the expected ratio (N_{MC}), to cancel the detector systematics and the uncertainties in the flux calculations, where the uncertainty in the absolute atmospheric neutrino flux is about 20 % and the error in the flavor ratio is expected to be within 5 %. The double ratio R is defined as :

$$R(\mu/e) \equiv (N_\mu/N_e)_{Data}/(N_\mu/N_e)_{MC} \tag{1.15}$$

where the ratio should be unity without oscillations. Both IMB and Kamiokande experiments measured R that was much less than unity as listed in Table 1.2. This became the "atmospheric neutrino anomaly" in the 1980's and was interpreted as a possible indication for neutrino oscillations. Later experiments, NUSEX [26] and Frejus [27] using iron calorimeters, have reported no deviation from unity but using smaller data samples. However, Soudan 2, also an iron tracking calorimeter, measured smaller flavor ratio with higher statistics later [28, 29]. A successor of Kamiokande, Super-Kamiokande, also measured smaller flavor ratio with much larger data sample [41, 42]. Table 1.2 lists the flavor ratios measured by various experiments. In addition to the flavor ratio, Kamiokande measured a zenith angle dependence of R [30]. Using upward-going muons induced by atmospheric neutrinos, Kamiokande [31], Soudan 2 [34], and MACRO (composed of liquid scintillation counters) [32, 33] found the zenith angle dependent deficit of muon

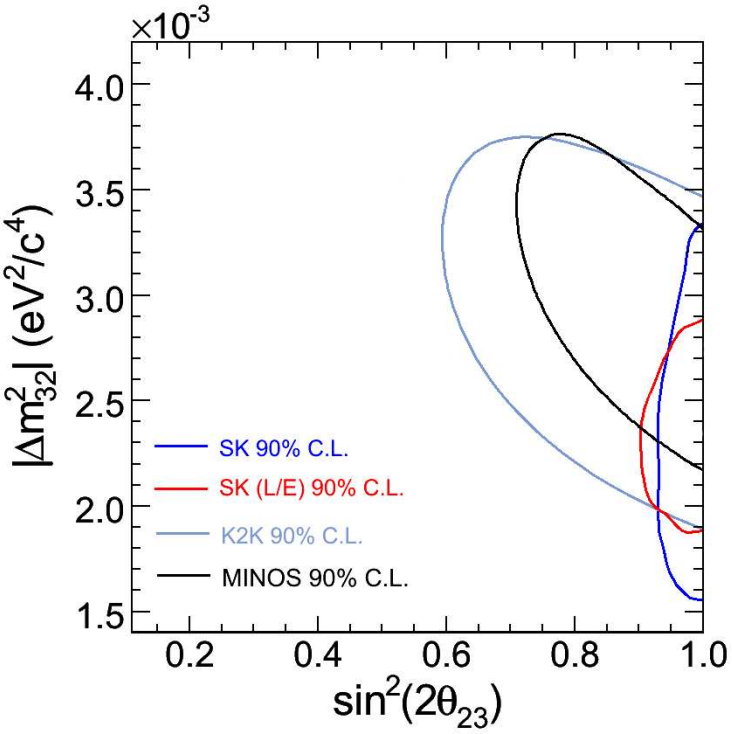

Figure 1.4: A contour plot of allowed regions of oscillation parameters, $\sin^2 2\theta$ and Δm^2 for $\nu_\mu \leftrightarrow \nu_\tau$ oscillations. The results from Super-Kamiokande [46, 49], K2K [39] and MINOS [40] experiments are shown.

neutrinos. Recently, the atmospheric neutrino results from the MINOS experiment have also shown the consistent results with previous measurements [38]. All observations indicated the neutrino oscillations, and the measured Δm^2 and $\sin^2 2\theta$ by Kamiokande [30, 31], MACRO [33, 35, 37], Soudan 2 [34, 36], and MINOS [38] in the $\nu_\mu \leftrightarrow \nu_\tau$ analyses were consistent with each other.

The results from atmospheric neutrino experiments have been examined and confirmed by two accelerator-based long-baseline experiments, K2K [39] and MINOS [40]. They observed the disappearance of muon neutrinos, and the allowed regions of $\sin^2 2\theta$ and Δm^2 are shown in Figure 1.4 [40].

1.5 Super-Kamiokande

The Super-Kamiokande (Super-K or SK) is a water Cherenkov detector. After the operation started in 1996, Super-K also observed the flavor ratio

much smaller than the unity with much larger statistics [41, 42] (see Table 1.2) and the zenith angle dependent deficit of muon neutrinos using upward-going muons induced by atmospheric neutrinos [43, 44].

In 1998, the Super-K announced the first evidence for neutrino oscillations by observing a strong zenith angle dependent deficit of muon neutrinos [45]. Figure 1.5 shows the zenith angle distributions [46], and the depletion of muon neutrinos is seen clearly in the upward-going directions (the zenith angle, $\cos\theta < 0$). The precise measurements of oscillation parameters using the atmospheric neutrino data have been made [46, 47, 48], and the evidence for an oscillatory signature in the atmospheric neutrino oscillations have been observed [47, 49] as shown in Figure 1.6. The Super-K atmospheric neutrino data favor $\nu_\mu \leftrightarrow \nu_\tau$ oscillations and have excluded $\nu_\mu \leftrightarrow \nu_e$ [45] and pure $\nu_\mu \leftrightarrow \nu_{sterile}$ oscillations [50] as a dominant source of the deficit of muon neutrinos.

From these analyses, the allowed regions of $\sin^2 2\theta$ and Δm^2 for $\nu_\mu \leftrightarrow \nu_\tau$ oscillations are obtained as shown in the contours in Figure 1.4.

1.5.1 Super-Kamiokande Collaboration

The Super-Kamiokande collaboration consists of 35 institutions and about 140 physicists from Japan, the United States, Korea, Poland, and China. The host institution is the Kamioka Observatory of the Institute for Cosmic Ray Research (ICRR), University of Tokyo, which provides the facilities.

Stony Brook University (Nucleon decay and Neutrino (NN) Group lead by Professor Chang Kee Jung) has made a significant contribution to the experiment for the hardware, software, and physics analyses.

1.6 Motivation of the analysis in this thesis

Neutrino oscillations in the atmospheric neutrinos have been discovered. Precise measurements of oscillation parameters have been made by several experiments. The deficit of muon neutrinos in the atmospheric neutrino flux is observed leading to a favored $\nu_\mu \leftrightarrow \nu_\tau$ oscillation scenario. However the observation of appearance of tau neutrinos from such oscillations, which has not been explicitly observed, would be unambiguous confirmation of the $\nu_\mu \leftrightarrow \nu_\tau$ oscillation. In this thesis, the search for the appearance of tau neutrinos is explored using the atmospheric neutrino data from Super-Kamiokande experiment.

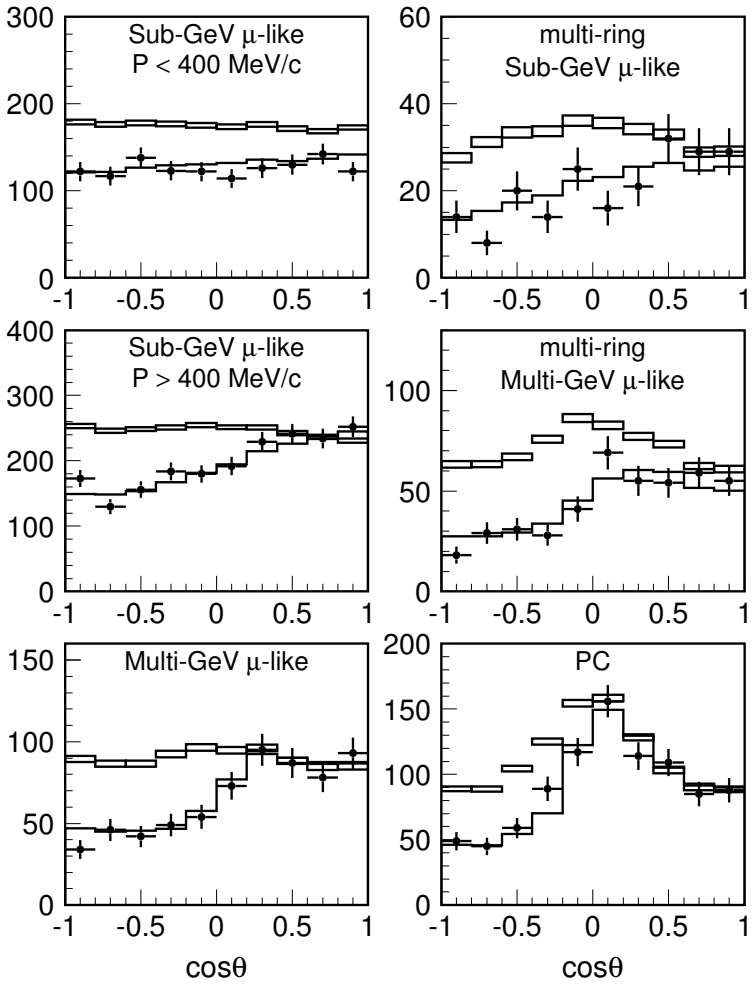

Figure 1.5: The zenith angle distributions. The points show data, box histograms show the MC prediction without oscillation, and the lines show the best-fit expectations for $\nu_\mu \leftrightarrow \nu_\tau$ oscillations with ($\sin^2 2\theta$, Δm^2) = (1.0, 2.1 $\times$ 10^{-3} eV^2) [46].

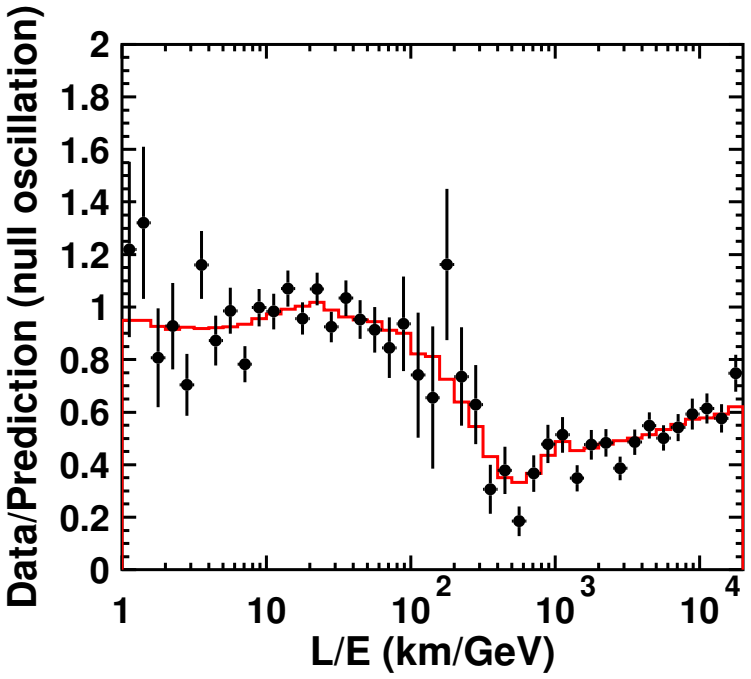

Figure 1.6: The ratio of the data to MC without oscillation as a function of L/E [49]. The dots are data and the solid line is the best-fit. The sinusoidal signature of muon neutrino disappearance is observed.

Chapter 2

Super-Kamiokande Detector

This chapter describes the Super-Kamiokande (Super-K or SK) detector and each component as well as the data acquisition system of the detector. The Super-Kamiokande detector is a multi-purpose detector. The scientific goals includes studies of neutrinos from the atmosphere, the Sun, supernovae, gamma ray bursts, other astrophysical sources, and accelerator-generated neutrino beams. Various searches for proton decay, ultra-high energy cosmic ray, exotic physics such as Q-Balls and Monopoles have also been carried out. The first phase of the experiment, from April 1996 to July 2001, is defined as Super-Kamiokande-I (SK-I); the second phase, from December 2002 to October 2005 is defined as Super-Kamiokande-II (SK-II); and the present phase since June 2006 is defined as Super-Kamiokande-III (SK-III).

2.1 Overview

The Super-Kamiokande is a large water Cherenkov detector and is located at the Kamioka Observatory, the Institute of Cosmic Ray Research, University of Tokyo, in a zinc mine[1] owned and operated by Kamioka Mining and Smelting Company under Mt. Ikeno in Kamioka, Hida-city, Gifu prefecture in Japan, approximately 250 km west of Tokyo (Figure 2.1). The geographic location is at 36°25′33″ N, 137°18′37″ E and 371.8 m above sea level. This area is a part of the Japanese Alps, where there are many hot springs and ski resorts.

The experiment is a successor of Kamiokande experiment [24], which was named after the town, "Kamioka"and **N**ucleon **D**ecay **E**xperiment for their

[1]Several other physics experiments such as gravitational wave search , Dark Matter Search as well as another neutrino experiment, KamLand have been conducted in the same mine.

Figure 2.1: The location of Super-Kamiokande detector in Japan.

primary physics goal, nucleon decay search. But for Super-Kamiokande, the primary scientific research goals are not only nucleon decay search but also neutrinos, thus the name implies Super-Kamioka **N**ucleon **D**ecay **E**xperiment as well as **N**eutrino **D**etection **E**xperiment. The Super-K detector has an average of 1000 m (2700 m water equivalent) of rock overburden (Figure 2.2), which reduces the rate of cosmic ray background muons[2] by about five orders of magnitude compared to that on the surface of the earth. The rate at Super-K is approximately 2.2 Hz. In the detector region, there is a control room located near the detector, where the shift members monitor the detector during day, and in the dome area called the "SK dome" directly above the tank are the four quadrant electronics huts and calibration equipments. The exposed mine rock surfaces around the detector are coated with Mineguards, a spray-applied polyurethane membrane, to prevent radon emitted by the surrounding rock from entering the detector. An over-pressure of fresh air of low radon content is piped in from outside the mine, and radon-reduced air is also produced in the mine and pumped into the region above the water inside the detector tank, at a slight over-pressure as further described in a section 2.4. In order to keep radon out of the detector itself, the Super-K tank is tightly sealed. There are also air-tight doors between the Super-K detector area and the mine tunnel. The Super-K detector started operating in April 1996, and after 5 years of data-taking, the detector was shut down in July 2001 for upgrade and maintenance. This period is now called as Super-K-I or SK-I. After the completion of upgrade, while being filled with water on November 12, 2001, about 60% of the 50cm PMTs were destroyed in a few seconds due to the chain reaction of the implosion of PMTs. The reconstruction was completed within a year, and the 2nd phase, Super-K-II, was started with about half the number of PMTs. More details are described in Appendix A. The restoration work for a full PMT coverage has began in October 2005, and the 3rd phase of data-taking has started in June 2006 as Super-K-III. The detector has been operated by the Super-Kamiokande Collaboration, a joint collaboration of Japan, US, Korea, Poland, and China, in which there are about 140 physicists and engineers, and the data-taking is monitored continuously by collaboration members 24 hours a day.

[2]These muon events are "useful" backgrounds for detector calibrations as described later in Chapter 3.

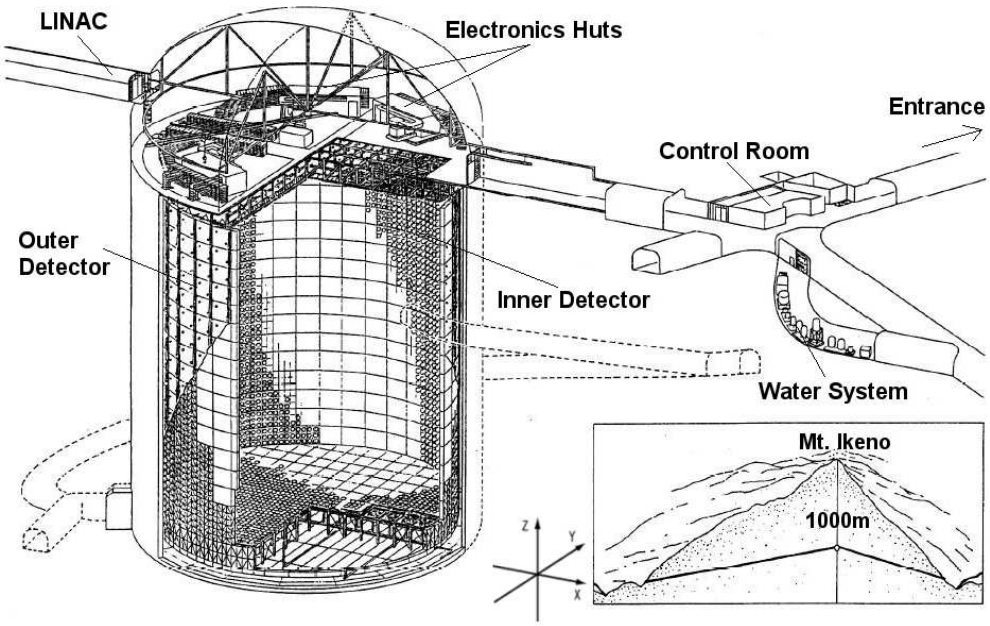

Figure 2.2: An overview of the Super-Kamiokande detector and its location under Mt. Ikeno. The inner detector and the outer detector regions and also the local coordinate are shown.

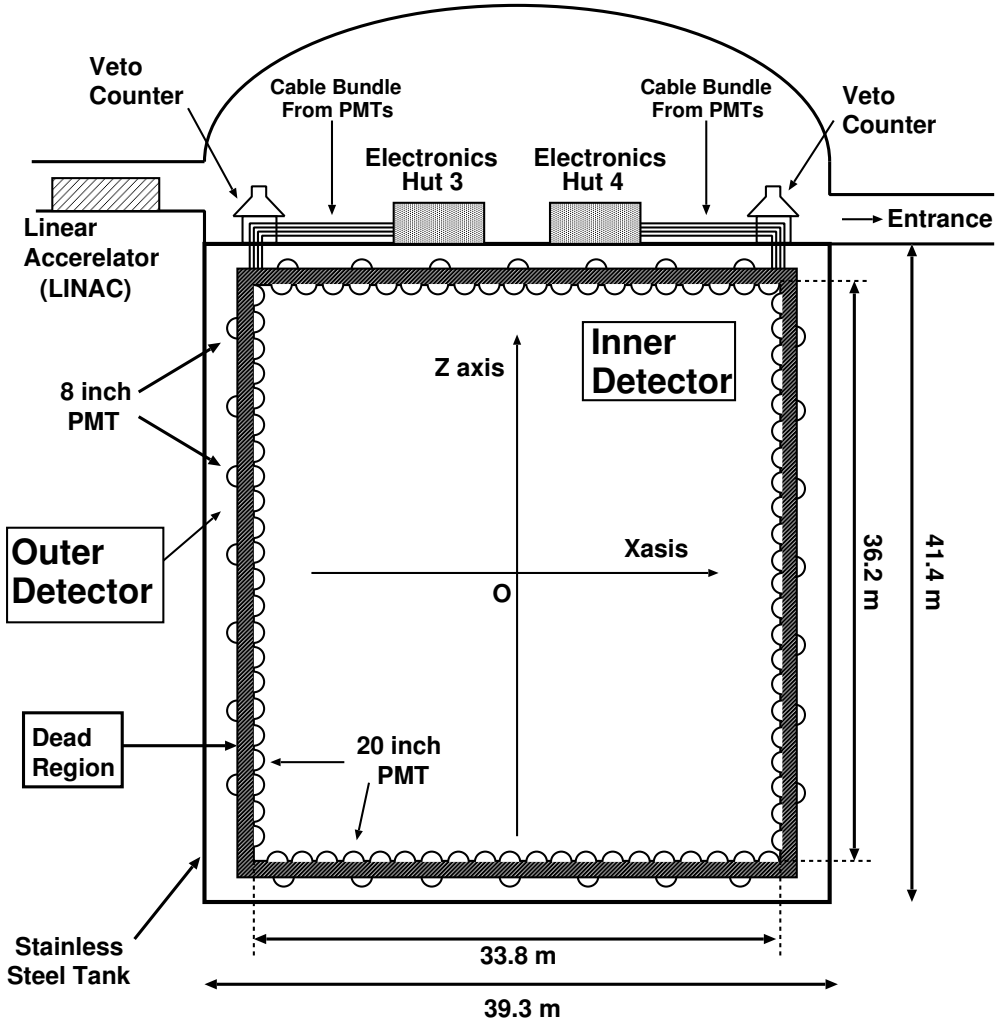

Figure 2.3: A side-view of the Super-Kamiokande detector and the dorm area where the four quadrant electronics huts and calibration equipments are located.

2.1.1 Cherenkov Radiation

The primary physical phenomenon that a water Cherenkov detector such as Super-K utilizes to detect charged particles is Cherenkov radiation. The effect was discovered by P. A. Cherenkov[3] in 1934 [51, 52]. Cherenkov radiation is electromagnetic radiation emitted when a charged particle travels through a medium with the velocity v greater than the speed of light in that medium (i.e. $v > c/n$), where c is the speed of light in vacuum and n is the index of refraction of the medium [53, 54]. Super-K contains ultra-pure water, of which the refraction index is $n = 1.34$. The Cherenkov threshold momentum for electrons/positrons ($e^{\pm}$), muons ($\mu^{\pm}$), and pions ($\pi^{\pm}$) are 0.58, 120, and 159 MeV/c respectively.

The emitted Cherenkov photons form a cone with an opening angle θ_C with respect to the direction of the particle. The opening angle θ_C is given by:

$$\cos\theta_C \;=\; \frac{1}{n(\lambda)\beta} \tag{2.1}$$

where $\beta = v/c$. The number of Cherenkov photons (dN) radiated per unit wavelength ($d\lambda$) per unit distance (dx) the charged particle travels is given by :

$$\frac{d^2N}{dxd\lambda} = \frac{2\pi\alpha}{\lambda^2}\left(1 - \frac{1}{(n(\lambda)\beta)^2}\right) = \frac{2\pi\alpha}{\lambda^2}\sin^2\theta_c, \tag{2.2}$$

where α is the fine structure constant.

For relativistic charged particles ($\beta \approx 1$) in pure water, the Cherenkov angle is $\approx 42°$, and the number of photons emitted is approximately 340 per cm over the Cherenkov spectrum between the wavelength of 300 nm to 600 nm, where the photomultiplier tubes (PMTs) are sensitive. In the SK detector, Cherenkov photons are detected to observe charged particles. The position, direction, energy, and the type of charged particles are reconstructed by measuring the number of Cherenkov photons and the timing, which is described in Chapter 6.

2.2 Water Tank: Detector

The Super-K detector is a cylindrical stainless-steel tank with 41.4 m in height and 39.3 m in diameter, containing 50 ktons of pure water. The tank is self-supporting, with concrete backfilled against the rough-hewn stone walls

[3]The 1958 Nobel Prize winner for this discovery.

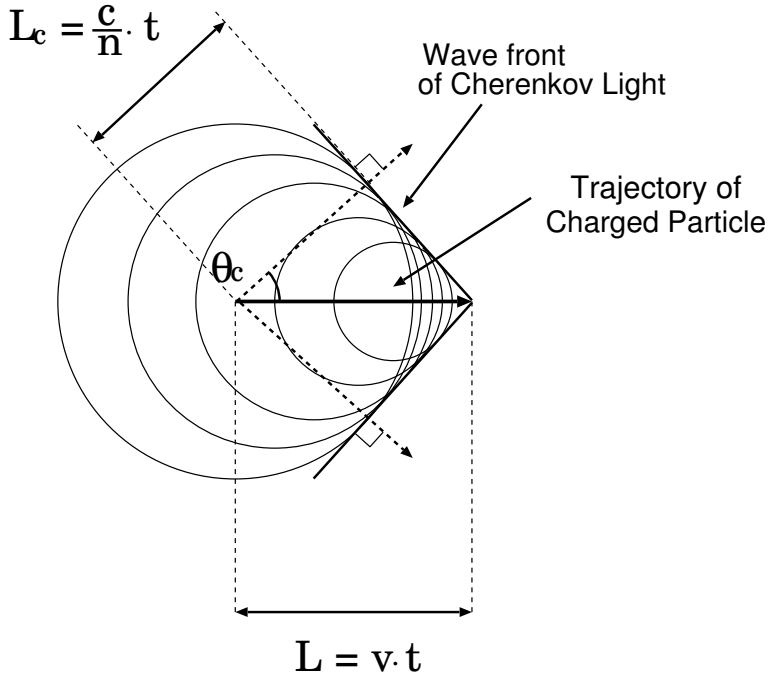

Figure 2.4: A diagram of Cherenkov light propagation. Each circle represents the light emitted successively by a charged particle moving with the speed of v. The wavefront of the emitted light travels with the speed of c/n. θ_c is the Cherenkov angle.

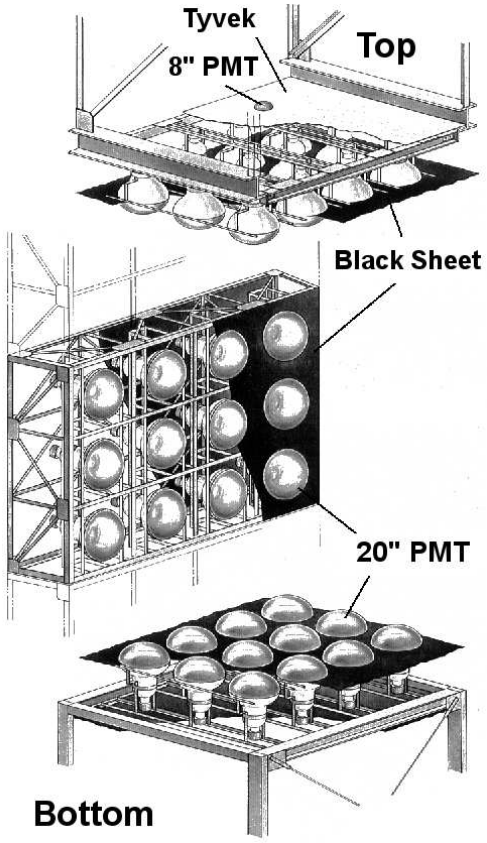

Figure 2.5: The layout of the PMT mounting structure. PMTs are mounted in frames called "super-modules." Each super-module holds twelve ID PMTs and two OD PMTs.

to counteract water pressure when the tank is filled with water. The detector consists of two separated detector regions: the inner detector (ID) and the outer detector (OD). These regions are optically divided by a welded stainless-steel framework of thickness 55 cm, which support the arrays of inward-facing ID and outward-facing OD PMTs. The water is able to flow between these regions. All of the cables for each PMTs run on the support structure to the quadrant electronics huts. Once the tank is filled with water, all of the regions are under water. The average geomagnetic field at the detector site is about 450 mG, and to maintain the PMT performance, 26 Helmholtz coils are arranged around the inner surfaces of the tank to compensate for the geomagnetic field. The reduced average field is approximately 50 mG.

2.2.1 Inner Detector

The inner detector is a cylinder with 36.2 m in height and 33.8 m in diameter and contains 32 ktons of water. This volume is viewed by the total of 11,146 inward-facing 50 cm PMTs (Hamamatsu R3600). A detailed description of the ID PMTs are described in the section 2.3.1. The ID PMTs are mounted on a 70 cm grid, with 7650 on the barrel (side walls), 1748 on the top and 1748 on the bottom. Thus, the effective photocathode coverage of the ID surface is 40 %. The remaining 60 % of the ID surface area, i.e. gaps between the ID PMTs, are covered by opaque black polyethylene telephthalate sheets (Figure 2.5). These sheets improve the optical separation between the ID and OD and suppress unwanted low-energy events due to residual radioactivity occurring behind the PMTs. The fiducial volume (2 m from the ID PMT surface), which is used for the analysis in this thesis, is 22.5 ktons of water.

For SK-II, the number of the ID PMTs are 5181 and the photocathode coverage is 19 %. The remaining area are covered by the black sheets. Also, each PMT is covered by an acrylic shield (Appendix A).

2.2.2 Outer Detector

The outer detector is a cylindrical shell surrounding the ID region and the framework structure. The thickness of the OD is about 2.05 m on the top and the bottom, and 2.2 m on the barrel wall. The OD contains about 18 ktons of water. On the outside wall of the framework, 1,885 outward-facing 20 cm PMTs (Hamamatsu R1408) are mounted with 302 on the top, 308 on the bottom, and 1275 on the barrel wall. The main purpose of the OD volume is to serve as an active veto counter against incoming particles such as cosmic ray muons, to tag an exiting charged particles from the ID, and to act as a passive radioactivity shield for neutrons and γ rays from the surrounding rocks. The entire surface of the OD is lined with reflective white Tyvek sheets, which has the reflectivity of more than 80 % for Cherenkov photons, and each OD PMT is attached to a acrylic wavelength shifting plate to enhance the light collection efficiency. The Section 2.3.2 describes the details of the OD PMTs.

For SK-II, the OD configuration is the same as for SK-I.

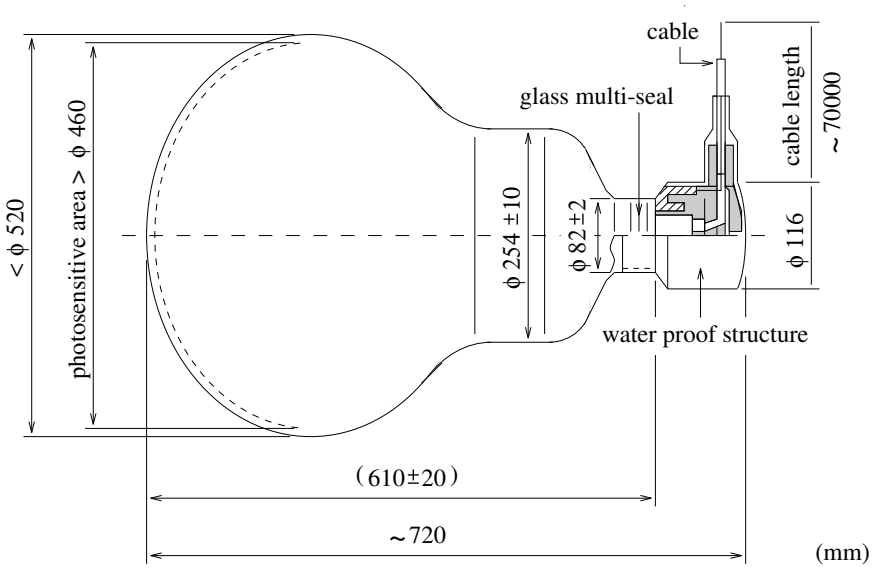

Figure 2.6: An overview of the 20 inch PMT used in the Super-K inner detector.

2.3 Photomultiplier Tube (PMT)

2.3.1 Inner Detector PMT

The ID photomultiplier tubes are Hamamatsu R3600 model and have photocathode with a diameter of 50 cm (20 inch). This PMT was originally developed by Hamamatsu Photonics K.K. with Kamiokande collaborators for the use in Kamiokande experiment [56]. It was later improved for the use in Super-Kamiokande experiment [57]. An overview of the ID PMT is shown in Figure 2.6, and the specifications are summarized in Table 2.1. The photocathode is made from 5mm thick borosilicate glass for its transmittance and water durability and is coated with Bialkali (Sb-K-Cs) to match its peak quantum efficiency (QE) with the Cherenkov spectrum peak as shown in Figure 2.7. The peak QE is about 21 % at the wavelength of 360 nm to 400 nm (Figure 2.8). The dynode structure of the ID PMTs is optimized to accomplish a good energy resolution and fast timing response. The collection efficiency

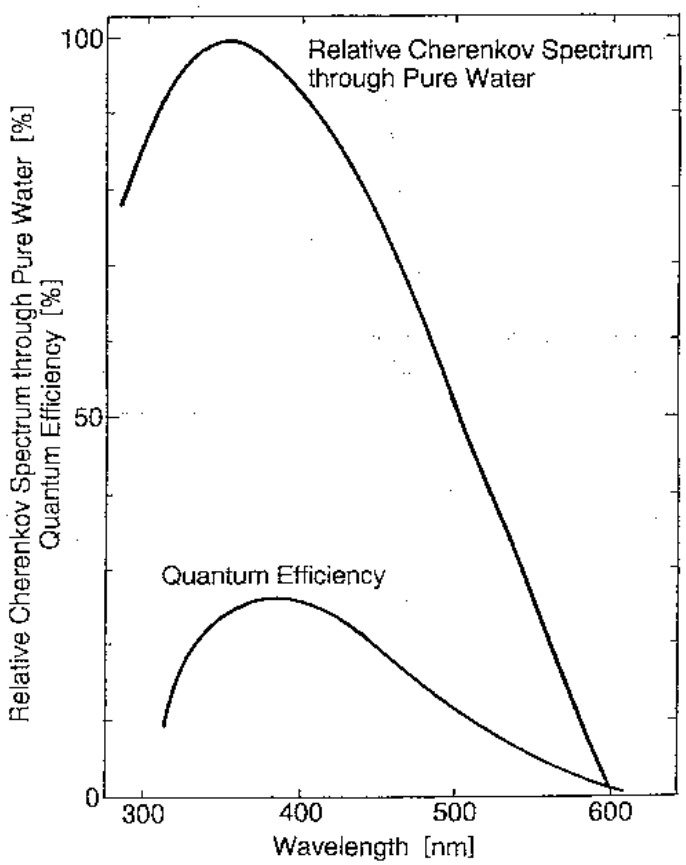

Figure 2.7: The spectrum shape of Cherenkov light travelling through pure water and the quantum efficiency of the ID (20 inch) PMTs as a function of photon wavelength are shown.

for photoelectrons (p.e.) at the first dynode is over 70 % and is uniform over the photocathode within ±7 %. The single p.e. peak can be clearly seen as shown in Figure 2.9, and the timing resolution for a single p.e. signal is approximately 2.2 ns (Figure 2.10). The average rate of dark noise at the 0.25 p.e. threshold used in Super-K is about 3 Hz. The gain of the ID PMTs is 10^7 at a supply high voltage from 1700 V to 2000 V. The neck of each PMT is coated with a silver reflector to block external light. The signal from each PMT is read out via 70 m co-axial cable to one of four quadrant electronics hut located directly above the tank.

In SK-II, each ID PMT is encased in an acrylic cover to prevent a chain reaction of any implosion of ID PMTs (see Appendix A).

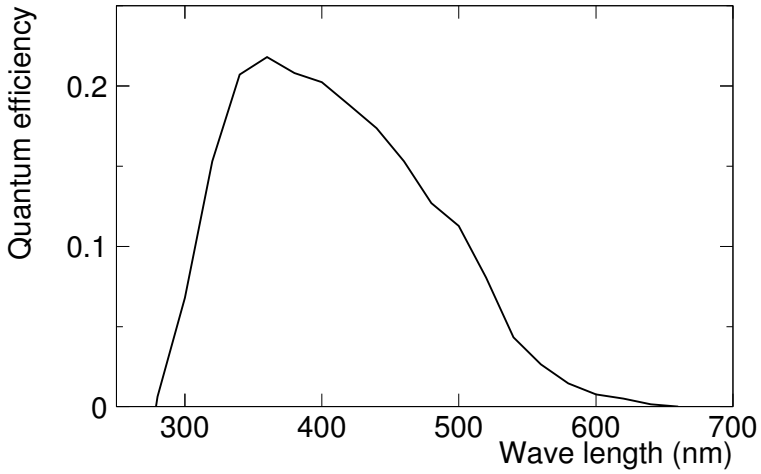

Figure 2.8: The quantum efficiency of the ID (20 inch) PMTs as a function of photon wavelength.

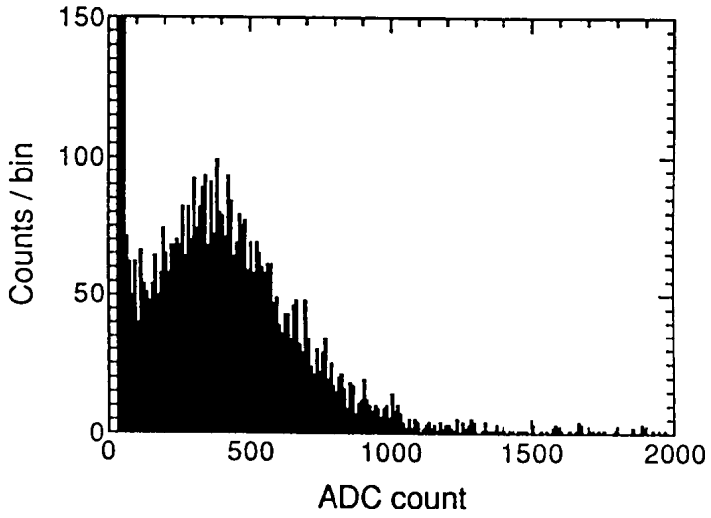

Figure 2.9: The distribution of a single photoelectron pulse peaked around 400 counts. The peak near 0 ADC count is due to PMT dark noise.

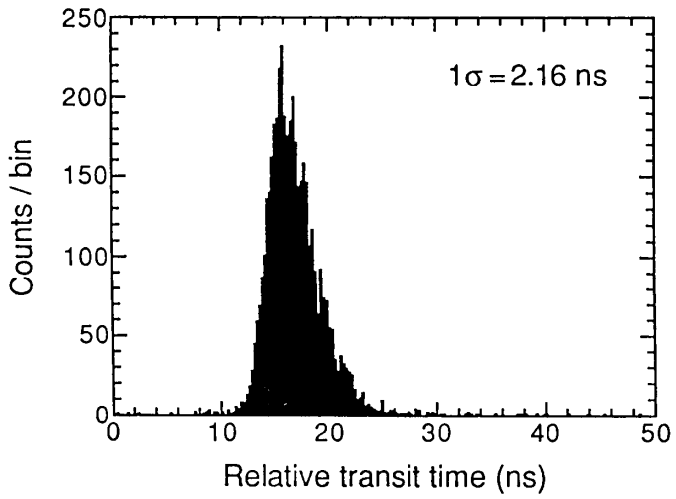

Figure 2.10: Relative transit time distribution for the ID PMT with 410 nm wavelength light at the single photoelectron intensity level.

Table 2.1: Specifications of 20 inch PMT (Hamamatsu R3600 PMT)

Photocathode area	50.8 cm diameter
Shape	Hemispherical
Window material	Pyrex glass ($4 \sim 5$ mm)
Photocathode material	Bialkali (Sb-K-Cs)
Dynodes	11 stage Venetian blind type
Spectral Response	300 nm to 650 nm
Quantum efficiency	22 % at $\lambda = 390$ nm (peak)
Gain	10^7 at ~ 2000 V
Dark current	200 nA at 10^7 gain
Dark noise rate	3 kHz at 10^7 gain
Cathode non-uniformity	< 10 %
Anode non-uniformity	< 40 %
Transit time	90 nsec at 10^7 gain
Transit time spread	2.2 nsec RMS at 1 p.e. levels
Weight	13 kg
Pressure tolerance	6 kg/cm^2 water pressure

2.3.2 Outer Detector PMT

The OD photomultiplier tubes are Hamamatsu R1408 model with photocathode of 20 cm (8 inch) in diameter. For SK-I, the OD PMTs were recycled from the IMB experiment [22] after the completion of the experiment. For SK-II, new OD PMTs were installed. The OD PMT array is sparse and only 1,885 PMTs are mounted in the entire OD. To enhance the Cherenkov light collection efficiency, an acrylic wavelength shifting plate doped with 50 mg/l of bis-MSB (60 cm × 60 cm × 1.3 cm) is attached to the face of each OD PMT [55]. The wavelength shifting plates absorb UV light and emit photons in the blue-green wavelength, which match the peak sensitivity of the PMTs. The efficiency is improved by about a factor of 1.5. The timing resolution of the OD PMTs is about 13 ns without the wavelength shifting place and 15 ns with the plate. This resolution is considerably poorer than the 2 ns resolution of the ID PMTs. However, since the design of the OD was optimized for use as a veto counter, the extra photons are of importance while the poorer timing resolution is of little consequence.

2.4 Water Purification System

It is crucial to have clean water for the Super-Kamiokande experiment to make precise measurements. Any dust, particle, and bacteria in water can reduce the water transparency for Cherenkov photons via absorption and scattering. Radioactive contaminants such as radon ($^{2}22$Rn) can become a source of background for solar neutrinos in the MeV energy range. To minimize these effects, the water purification system is constructed to produce ultra-pure water [60, 61]. In Super-K, a natural spring water in the Kamioka mine is used, and the water is continuously circulated through the purification system with a flow rate of about 35 ton/hour. This corresponds that the entire 50 kton of water in the detector is passed through the purification system once every two months. The purification process takes several steps as follows:

- **1 μm mesh filter:**
  Removes large contaminants such as dust and small particles.

- **Heat exchanger:**
  Cools water that is heated by the pumps of the purification system. Low water temperatures decrease the PMT dark noise rate and suppress the growth of bacteria. Typical water temperatures are 14.2°C before the first heat exchanger and 12.9°C after the second heat exchanger.

- **Cartridge polisher:**
  Eliminates metal heavy ions such as Na^{+}, Cl^{-}, Ca^{+2}.

- **UV sterilizer:**
  Kills any bacteria in the water.

- **Radon-free air dissolving tank:**
  Dissolves air from the radon-free system into the water to improve the radon removal capabilities of the vacuum degasifier.

- **Reverse osmosis filter:**
  Futher removes small contaminants.

- **Vacuum degasifier:**
  Removes dissolved gases (oxygen and radon) from the water, with efficiency of ∼96% for the dissolved radon gas. Oxygen in the water can cause growth of bacteria.

- **Ultra filter:**
  Removes small contaminants down to sizes of 10 nm.

- **Membrane degasifier:**
  Further removes dissolved radon gas with a removal efficiency of 83%.

Before the purification process, a typical number of particles of size greater than 0.2 μm in the water is about 1,000 particles/cc, which is reduced to 6 particles/cc after the purification. The resistivity of water entering the purification system from Super-K is about 11 MΩ·cm. After the purification, the water has an average resistivity of 18.20 MΩ·cm, which is very close to the chemical limit of 18.24 MΩ·cm. The concentration of ^{222}Rn in the water after the purification is reduced to less than 1 mBq/m^3 [58] and is monitored in real-time by several radon detectors [59, 61]. The light attenuation length is achieved to be ∼100 m (Section 3.2).

2.5 Radon Hut and Air Purification System

It is also essential to have clean air in the detector and the experimental area to minimize the radon level in the air. The radon concentration of the mine air in the access tunnel to the experimental site has a strong seasonal variation of 2,000 ∼ 3,000 Bq/m^3 during summer and 100 ∼ 300 Bq/m^3 during winter as shown in Figure 2.12. This is caused by the seasonal variation of the

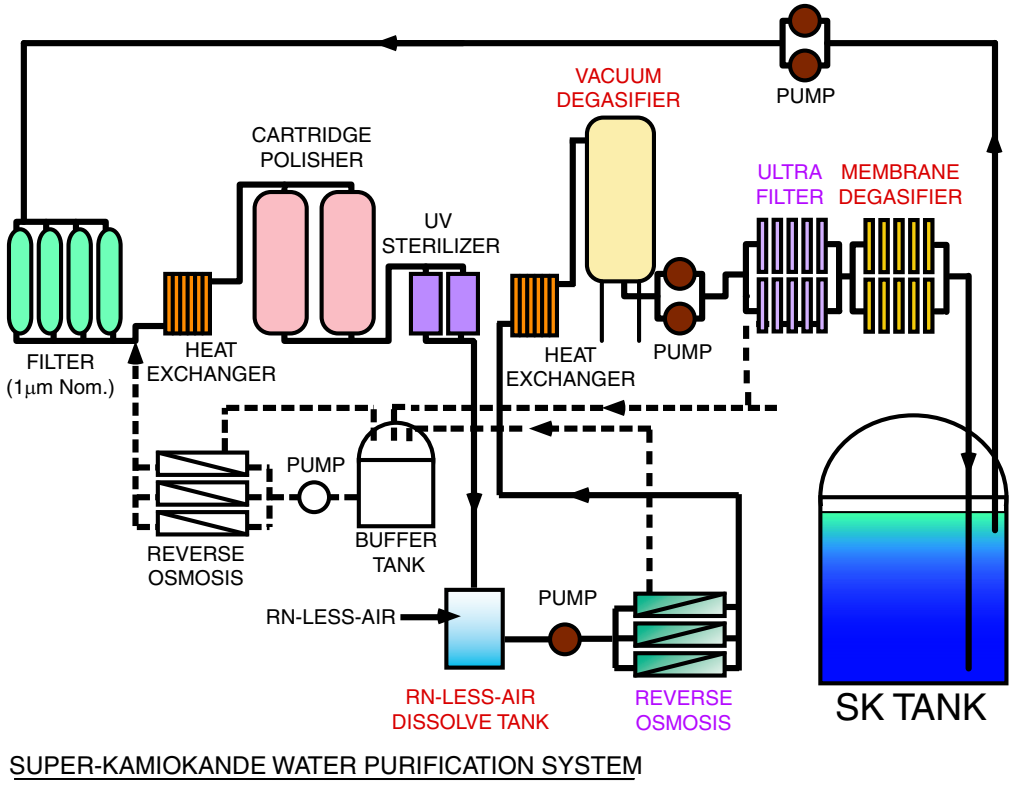

Figure 2.11: A schematic view of the water purification system.

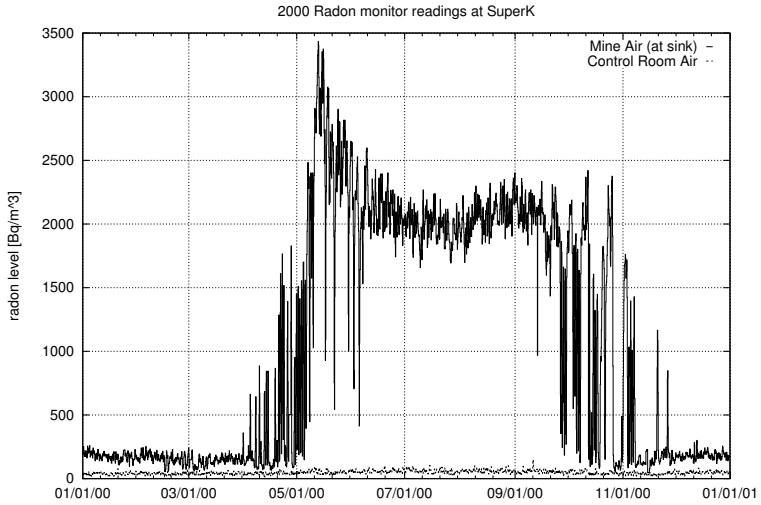

Figure 2.12: The upper histogram (solid curve) shows the measured radon concentration levels in the mine air [58]. The lower histogram (dashed curve) shows the corresponding radon levels in the SK dome. Strong seasonal variations in the flow of mine air affect the radon level in the detector.

air from inside the mine. During summer, air flows out the tunnel and during winter, cold fresh air flows into the mine.

Fresh air from outside the mine is continuously pumped into the SK dome area at the rate of $10\,\mathrm{m}^3$/minute through an air duct along the 1.8 km Atotsu access tunnel to the SK experimental area.

A "Radon Hut" houses the air blowers, air filters and cooler, and is located at the Atotsu tunnel entrance to take the air from approximately 25 meters above the entrance, where the radon level was found to remain at 10 $\sim 30\,\mathrm{Bq/m}^3$ all year long. The fresh air is delivered into the Super-K experimental area at a rate of $10\,\mathrm{m}^3$/minute (in 2002, the flow rate was increased to $50\,\mathrm{m}^3$/min to improve the air quality in the water purification system and to distribute fresh air to newly installed experimental rooms around the SK detector area). As a result, the typical radon concentration in the SK dome air is $20 \sim 30\,\mathrm{mBq/m}^3$.

Furthermore, to keep the radon level inside the detector absolute minimum, radon-free air is produced by the air purification system in the mine and is continuously pumped into the space above the water surface inside the Super-K tank at a positive pressure to prevent radon air from entering the detector and dissolving into the purified water [60]. A schematic view of the air purification

system is shown in Figure 2.13. The radon concentration of the radon-free air is less than $3\,\mathrm{mBq/m^3}$. The air purification system consists of compressors, a buffer tank, driers, and the filters. The air flow rate is about $18\,\mathrm{m^3/hour}$. The process of the air purification system is described as follows:

- **Compressor:**
  Compresses air to $7 \sim 8.5$ atm pressure.
- **Air Filter:**
  Removes dusts in sizes of $\sim 0.3\,\mu$m.
- **Buffer Tank:**
  Stores the air.
- **Air Drier:**
  Dries the air and removes CO_2 gas to improve the radon removal capability in Carbon Columns.
- **Carbon Columns:**
  Removes radon gas as carbon absorbs radon.
- **Air Filter:**
  Further Removes small dust and particles of $0.01\,\mu\mathrm{m} \sim 0.01\,\mu$m.
- **Charcoal Columns:**
  Further removes the remaining radon gas with the charcoal cooled down to –40°C.

2.6 Electronics and Data Acquisition System (DAQ)

The analog signals from each ID PMT and OD PMT are sent to the data aquisition system in one of four quadrant electronics huts in the SK dome area All the data are collected from four electronics hut and sent to the central hut, where the global even trigger is generated. The self-triggering DAQ system collects the analog signals of the time and charge information from each PMT and digitizes them to store as an "event", which is then sent out to the online computer. In this section, the ID and the OD data acquisition systems and the trigger system are described.

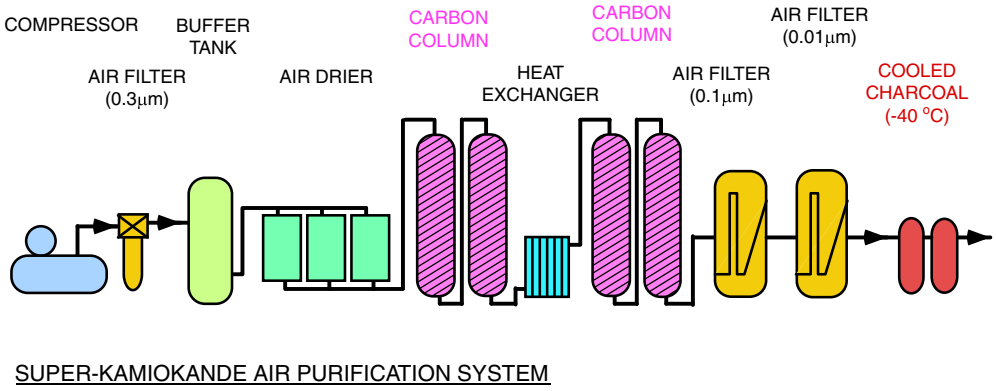

Figure 2.13: A schematic view of the radon-reducing air system.

2.6.1 Inner Detector DAQ

The ID PMT signals are processed by the electronics modules called Analog-Timing-Modules (ATMs), a custom built front-end electronics module of TRISTAN KEK Online (TKO) standard optimized to handle a large number of channels by KEK [62, 63, 64]. The ATM is developped by Super-K collaborators and Toshiba. The ATM has a combined function of Analog to Digital Converter (ADC) and Time to Digital Converter (TDC) and records the integrated charge and the arrival timing information of each PMT signal. One ATM has 12 input channels for 12 PMTs. Each channel of the ATMs has a charge dynamic range of 550 pC with a resolution of 0.2 pC ($\sim$ 0.1 p.e.), and a timing dynamic range of 1.2 μsec with a resolution of 0.3 nsec. To minimize the electronics dead time in the data taking for two successive events, such as a muon followed by its decay electron and supernova neutrino bursts, each input channel of the ATMs is designed to have two Charge to Analog Converters (QAC) and Time to Analog Converter (TAC) [65]. Each ATM board has the following ports on the front panel for:

- HITSUM: the analog sum of signals from "hit" PMTs to be sent to a global trigger module
- TRIGGER: the input port for a trigger signal
- PMTSUM: a sum of analog signals from 12 PMTs, which was not used in SK-I but is fed to Flash ADC in SK-II (See 2.6.4)
- EVENT-COUNTER: takes 8 bit event count signals.

A block diagram of the ATM board is shown in Figure 2.14.

Each PMT signal sent to ATM is first amplified with a gain of 100 and then split into four signals. One is sent out as PMTSUM output signal. One is sent to the discriminator, with a threshold level of 0.25 p.e. for each channel. When a PMT signal exceeds the threshold, a HITSUM signal (200 ns width and 15 mV pulse height) is sent out to the global trigger system. The pulse height of a HITSUM signal is proportional to the number of hit PMTs. Simultaneously, a "gate" signal (400 ns width) for QAC and a "start" signal for TAC are generated to start storing the charge and time information for 1.2 μs. The rest of two splitted signals are fed to QACs. If a global trigger (see section 2.6.3 is issued, a "stop" signal is sent to TAC and then the charge and time information in QAC and TAC is digitized by ADC, which is stored in the internal memory FIFO (First In First Out) in ATM. If no global trigger is not issued within 1.2,μs, all the information in QAC and TAC is discarded. This analog input block of the ATM is shown in Figure 2.15.

As shown in a schematic diagram of the ID DAQ system of Figure 2.16, each ATM board accepts signals from 12 PMTs. Total of 948 ATM boards are housed in 48 TKO crates (i.e. each TKO crate houses 20 ATM boards). 12 TKO crates are built in each of four quadrant electronics hut. A GO/NoGo (GONG) trigger module and a Super Control Header (SCH) also resides in each TKO crate. The GONG module distribute the global trigger signals and the event number to each ATM. The SCH module transfer the digitized data in the ATM FIFO memory to the Super Memory Partner (SMP) in Versa Module Europe (VME) crate. Two VME crates are installed in each electronics hut, and each VME is connected to 6 SMPs. The SMP modules are designed to have two memory buffers, which can switch from one to the other when successive event occurs, to further reduce the electronics dead time. The data is transfered from the SMP modules to server computers, Sun UltraSPARC workstation, (2 workstations per electronics hut) via Bit-3 Sbus-VME interface card. Then finally the data is sent to a online host computer via FDDI (Fiber Distributed Data Interface) optical network. This online host computer assembles the data into "events". Once events are built, the data are sent out to the offline system. More details of the ID DAQ can be found in [58, 65, 66].

2.6.2 Outer Detector DAQ

The OD DAQ are rather simple compared to the ID DAQ. A schematic diagram of the OD DAQ is shown in Figure 2.18. The paddle cards distribute high voltage from each of HV main frame channels to 12 OD PMTs via coaxial

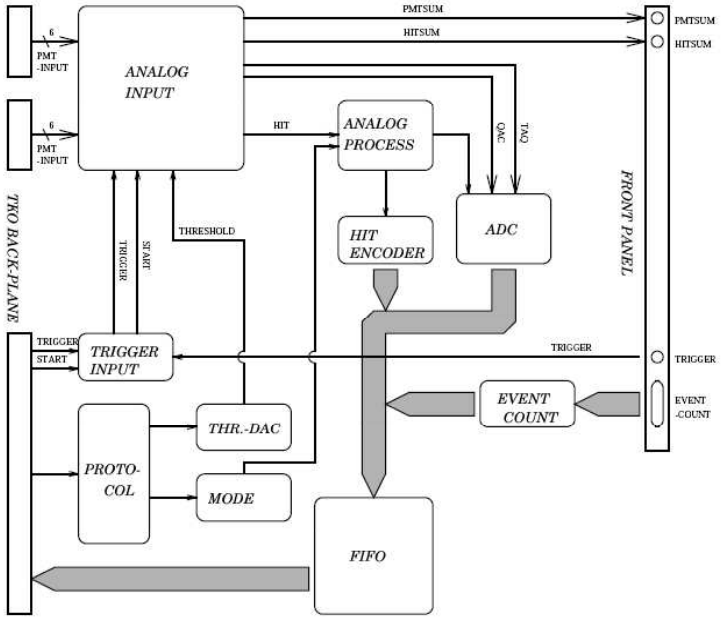

Figure 2.14: A block diagram of the Analog-Timing-Module (ATM).

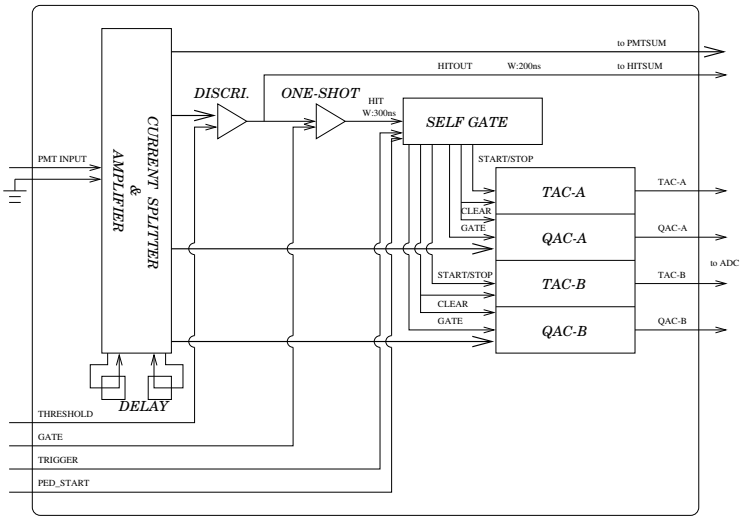

Figure 2.15: A schematic view of the analog input of the ATM for one channel.

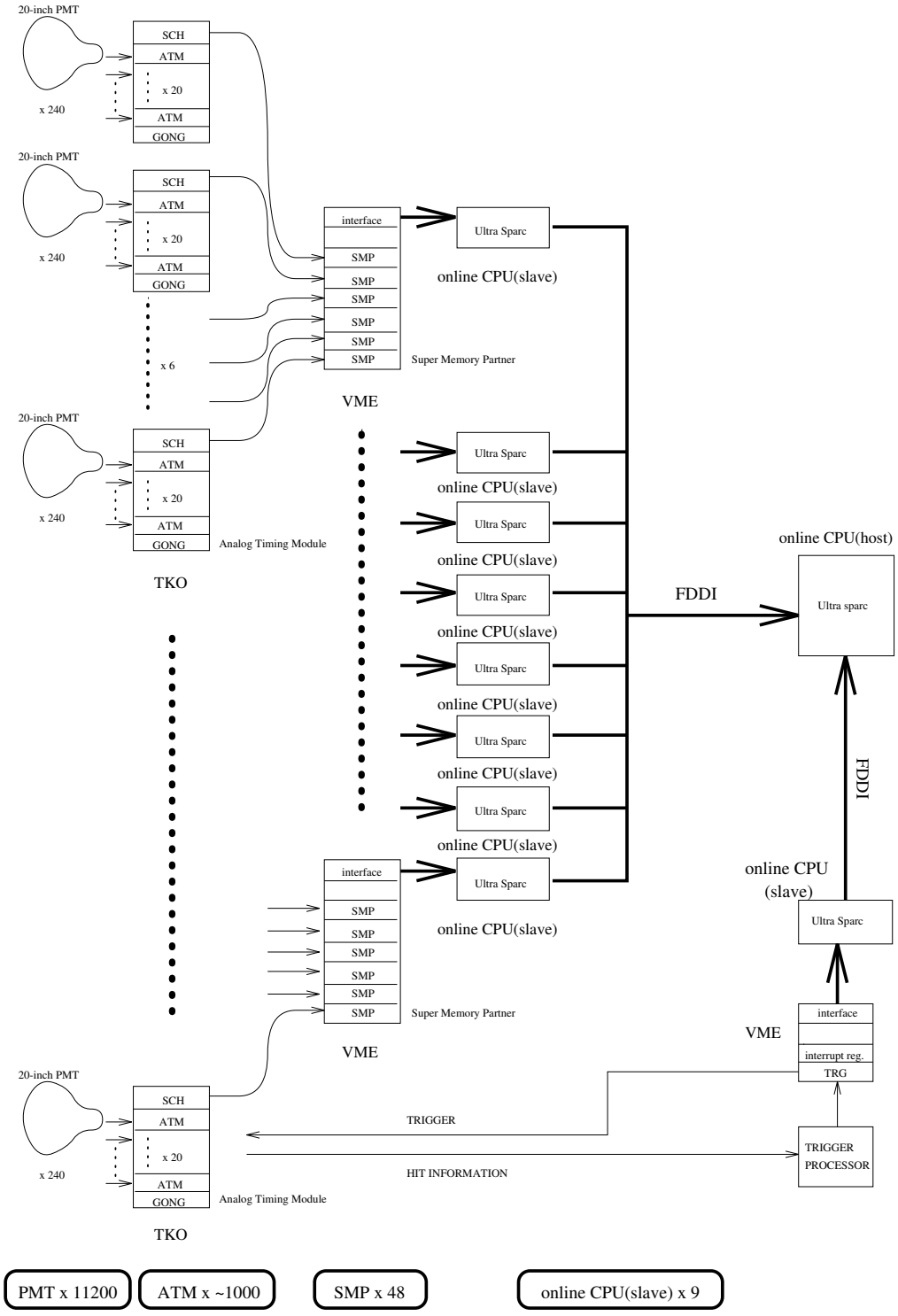

Figure 2.16: A schematic diagram of the ID DAQ

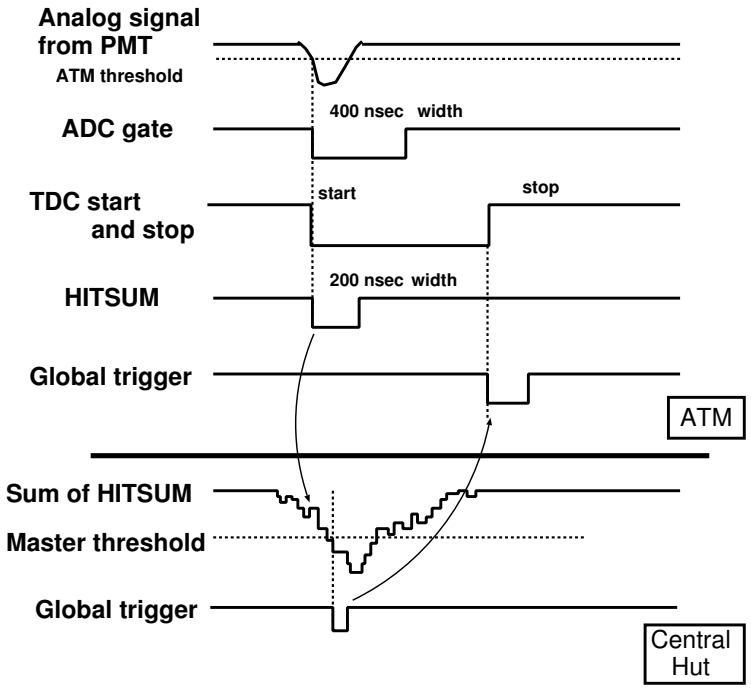

Figure 2.17: An overview of the ID trigger scheme.

cables and pick off the OD PMT signals, which are sent to Charge to Time Converter (QTC) modules. The QTC modules then generate a rectangular HITSUM signal to be sent to the global trigger module. The threshold of QTC modules is set to 0.25 p.e. Once a global trigger is received, the signal is digitized to the timing and charge information by a LeCroy 1877 multi-hit TDC module, which can store up to 8 QTC pulses with a resolution of 0.5 ns. The dynamic range of the TDC is 16 μs, with 10 μs before and 6 μs after the global trigger timing. The digitized TDC data are read by VME memory modules controlled by an online computer and are transfered via FDDI to the online host computer, which merges the OD data with the ID data to form a complete full detector event. More details of the ID DAQ can be found in [58, 66]

2.6.3 Trigger System

The global event trigger signals are sent out to record data from PMTs and are issued by four different ways (three ID triggers and one OD trigger); the high energy (HE) trigger, the low energy (LE) trigger, and the Super low

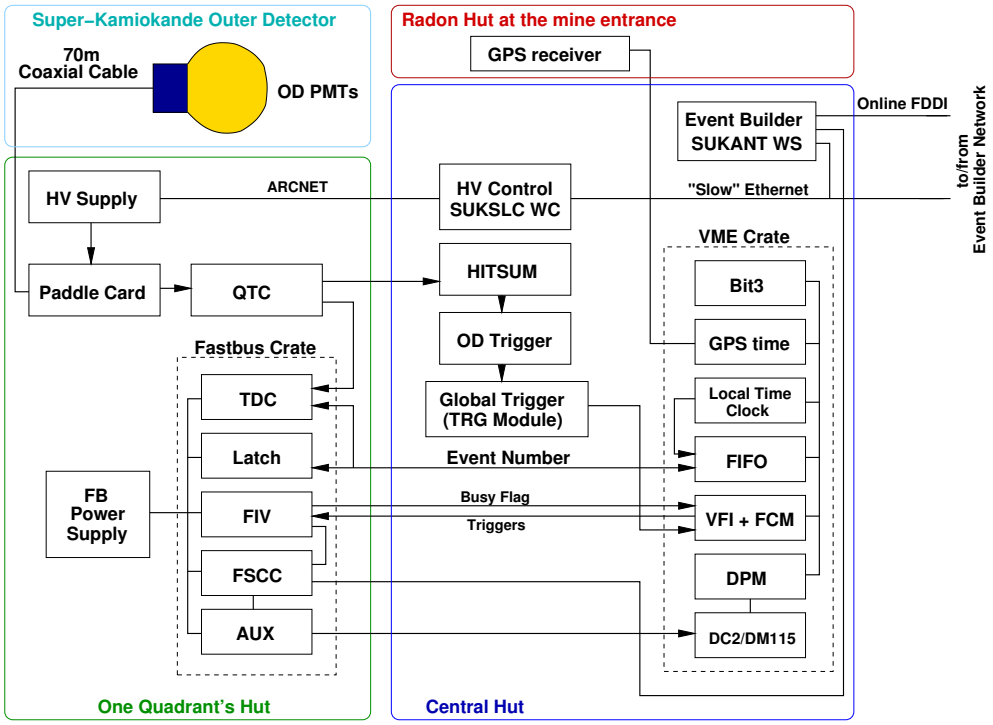

Figure 2.18: A schematic diagram of the Outer Detector DAQ

energy (SLE) trigger, and the outer detector (OD) trigger.

The ID triggers are generated when an ID-HITSUM signal with a 200 ns time window, which is summed over all of the HITSUM signals from ATMs, exceeds the threshold for each trigger. For the HE trigger, the threshold is -340 mV, which corresponds to 31 hit PMTs. For the LE trigger, the threshold is -320 mV (29 hit PMTs), which is equivalent to Cherenkov photons generated by 5.7 MeV electron. The SLE trigger is implemented to lower the threshold for solar neutrino analysis [58], and the threshold is lowered to -186 mV (17 ID PMT hits). The trigger rate is ∼5 Hz, ∼10 Hz, and ∼1000 Hz for the HE, LE, and SLE respectively. Similarly, the OD trigger is generated when an OD-HITSUM signal, which is a sum of the HITSUM signals with a 200 ns time window from QTCs. The threshold is 19 OD PMT hits. When an OD trigger occurs, there is a delay of 100 ns before the global trigger is issued, to see if a coincident ID trigger occurs. If no ID trigger is asserted within this interval, the OD triger issues a global trigger. The OD trigger rate is ∼3 Hz. For the analysis in this thesis and the atmospheric neutrino analyses, only the HE and OD triggers are relevant. There are also external triggers such as periodical trigger to monitor the detector performance, and the calibration trigger for the detector calibration (for the calibration, see Chapter 4). Typically, events generate a combination of these triggers such that high energy events have both of the HE and LE triggers.

If any one of the trigger signals is asserted, the trigger module (TRG) generates a global trigger and a 16-bit event number, which are distributed to all of four quadrant electronics huts, to initiate the data-taking for the current event. The TRG module records the trigger information of an event number, trigger time and the trigger type, which are read by the server computers in each electronics hut. At the end, the trigger information and the PMT data are merged by the online host computer in the central hut.

Each Super-K event has two time stamps of the local time and the absolute time. The local time, which is a relative timing between events, is measured by a 48 bit counter driven by a 50 MHz clock with 20 ns accuracy. During the Super-K data-taking, the run is stopped every 24 hours and restarted to avoid any over-running clock which could assign ambiguous times. The absolute Universal Time Clock (UTC) time of each event is stamped by the Global Positioning System (GPS) receiver provided by the OD electronics with the accuracy of 100 ns [67].

A Super-K event basically consists of a list of hit PMT numbers, ADC/TDC counts for those hit PMTs, and the time stamps.

2.6.4 Flash ADC

As a part of the Super-Kamiokande upgrade for SK-II in early 2003, Flash Analog-to-Digital-Converter (FADC) modules were added to the electronics [68, 69, 70]. The main goal is to reduce the electronics dead-time during data-taking and to improve event reconstruction by measuring PMT signal shapes. One of the improvements for physics analysis we expect from this upgrade is better detection efficiency of electrons from muon decays. An increase in the muon identification probability will improve the detection efficiency for processes such as a proton decay in the mode of $p \to \bar{\nu} K^+$, where $K^+ \to \mu^+ \nu_\mu$ is followed by $\mu^+ \to e^+ \bar{\nu}_\mu \nu_e$. Another important improvement we expect is a more accurate energy measurement for high energy events such as ν_e events from $\nu_\mu \to \nu_e$ neutrino oscillation. For these high energy events, the ADCs in our current electronics often saturates. Since FADCs record the PMT signal waveforms, the energy can be accurately measured [71]. I worked on the installation, debugging and calibration of the FADC system. I also worked on the development and improvement of the software after installing pre-amplifiers for each FADC channel in 2004.

2.6.5 Offline Data Process

Once the data are assembled by the online host machine, the data are sent to the "reformatter" machines to convert the raw data to the platform-independent ZEBRA Bank System (ZBS) format, developed at CERN [72]. The reformatted data are sent over a FDDI optical fiber out of the mine to be stored in a magnetic tape library (MTL) in the research building (so-called Kenkyuto). The disk space of the MTL is 200 TB and the data were written at a rate of $\sim$40 GB/day. The stored data are then processed by the analysis software to convert the ADC and TDC counts to physical quantities, charge (pC) and time (ns), respectively using the calibration tables (see 3).

The reformatted data were also copied on the 20 GB Digital Linear Tapes (DLTs), which were shipped to Stony Brook and used for the U.S. Super-Kamiokande (or offsite [4]) analyses. These "independent" [5] analyses were published and merged into one after the consistent results were obtained. After August 2000, the data copy process was discontinued.

[4] As the name implies, the "onsite" analyses were carried out by Japanese collaborators.

[5] It is not statistically independent because the same data set was used.

Chapter 3

Detector Calibration

A water Cherenkov detector is fairly simple detector. However, it is important to understand the characteristics of each detector component to make precise physics measurements. In order to achieve this, extensive detector calibrations have been carried out. In this chapter, the calibration methods for the PMT response to charge and timing, water transparency, and energy scale are described in detail.

3.1 PMT calibration

The signals, ADC (charge) and TDC(timing) counts, from the events detected by the PMTs are converted to physical quantities in the number of photo-electrons and nano second for analyses. In such conversions, it is essential to have a uniform response for every PMT to aviod any systematic bias. The PMT calibrations are performed to adjust each PMT individually to obtain the uniformity in charge and timing response.

3.1.1 Relative Gain

The uniform gain for all PMTs is necessary to have a good detector response without any systematic bias depending on the direction and positions of the events. The gain of a PMT is approximately proportional to the voltage as V^x, where x is constant (typically ~ 2.1) and V is the voltage applied to the PMT.

To obtain the uniformity, a xenon (Xe) lamp is used to calibrate the relative gain of each ID PMT, and the supply high voltage of each PMT is adjusted. A diagram of the Xe calibration system is shown in Figure 3.1. Light generated by a Xe lamp is passed through two filters: an ultraviolet (UV) filter to transmit only UV light, and a neutral density (ND) filter to adjust the light

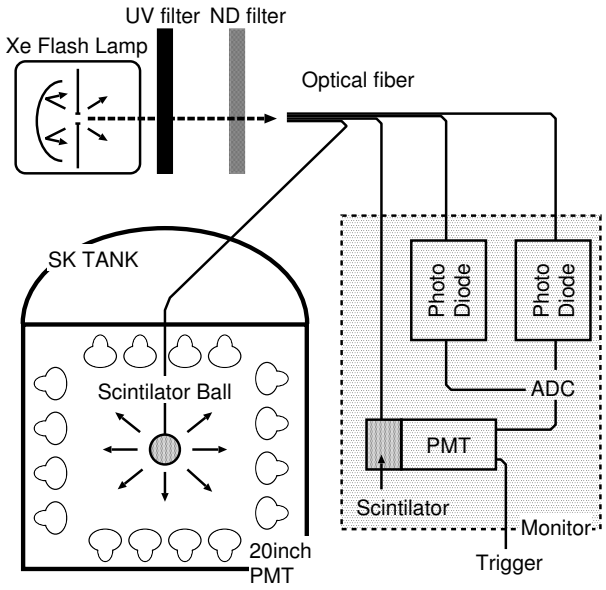

Figure 3.1: An overview of the Xe calibration system for the PMT relative gain measurement.

intensity. The light is then split and sent separately to the monitoring system and to the scintillator ball placed inside the Super-K tank. The scintillator ball is made of an acrylic resin with BBOT as a wavelength shifter and MgO powder as a diffuser. The BBOT is a wavelength shifter which absorbs the UV light and emits light with a peak wavelength of 440 nm. Thus, the wavelength is similar to the wavelength of Cherenkov light. The MgO powder is a diffuser which helps to emit the light uniformly in the tank.

The relative gain G_i of the i-th PMT is obtained by :

$$G_i = \frac{Q_i}{Q_0 f(\theta)} \cdot l_i^2 \cdot \exp\left(\frac{l_i}{L}\right) \tag{3.1}$$

where Q_i is the charge detected by the i-th PMT, Q_0 is a constant normalization factor, l_i is the distance from the light source to the i-th PMT, $f(\theta)$ is the PMT acceptance as a function of the incidence angle θ of light as defined in Figure 3.2, and L is the attenuation length.

The light detected by each PMT is corrected for light attenuation, angular acceptance of the PMT, and uniformity of the scintillator ball and is then normalized by the intensity of the Xe light. The high voltage is adjusted so that the corrected charge is uniform for all PMTs. The Xe calibration is performed for several positions in the tank with different voltages.

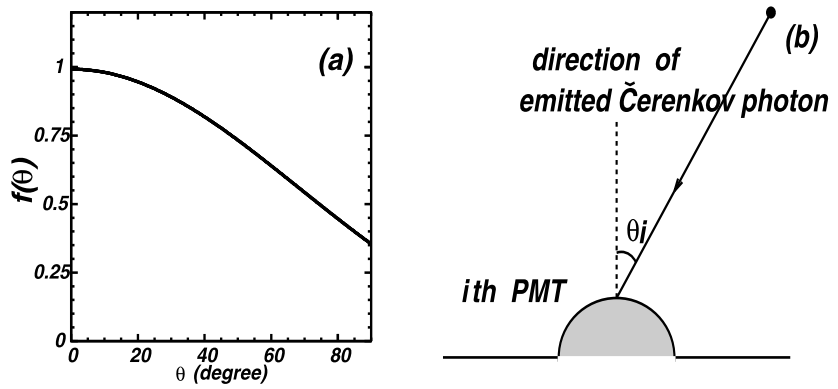

Figure 3.2: Relative photo-sensitivity: (a) Measurement result, (b) Definition of the incident angle

Figure 3.3 shows the distributions of the relative gain for all PMTs after the voltage adjustment. The spread is found to be 7 %. This is corrected in the event reconstruction software.

3.1.2 Absolute Gain

The charge in pico Coulomb (pC) measured by each PMT is converted to the number of photoelectrons (p.e.) for physics analyses. The absolute gain calibration of each PMT is necessary at the single p.e. level so that this conversion can be done correctly. The Ni-Cf source is used for this calibration as shown in Figure 3.4. Fast neutrons are produced by the spontaneous fission of ^{252}Cf and thermalized through elastic scattering off the protons in the water within the polyethylene container. The thermalized neutrons are captured on the Ni wire, and γ-rays of $6 \sim 9$ MeV are emitted. These gamma-rays knocks off electrons in the water via the Compton scattering, which produce Cherenkov light. Since the γ-rays have low energy and the number of hit PMTs is approximately $50 \sim 80$ total, it can be assumed that each PMT is hit by a single photon. The charge distribution of a single p.e. for a typical PMT is shown in Figure 3.5. The mean peak charge of 2.055 pC/p.e. is used for the conversion from pC to the number of p.e.

3.1.3 Relative Timing

It is also crucial to understand the accurate timing response of the PMTs for the reconstruction of vertices and directions of the events. The calibration

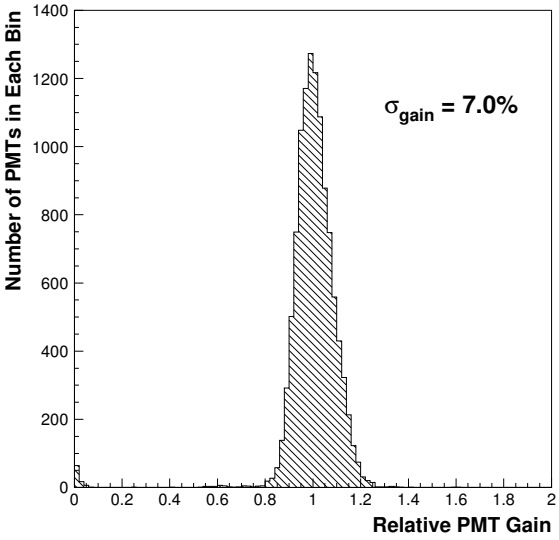

Figure 3.3: The distribution of the ID PMT relative gain for all of the ID PMTs. The horizontal axis is the relative gain normalized by its mean value. The spread is found to be 7 %.

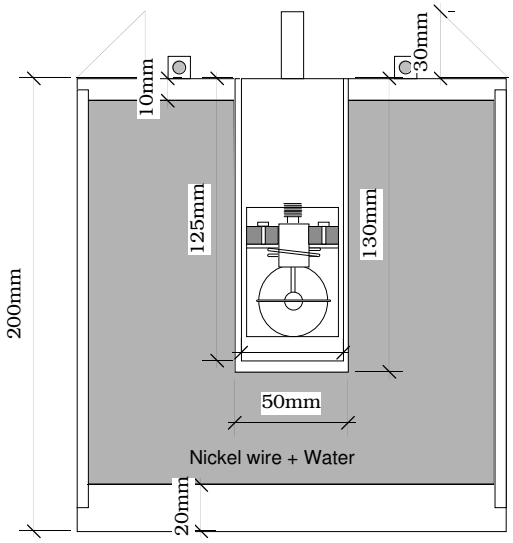

Figure 3.4: An overview of the Ni-Cf calibration system. Note that this is a cross section of a cylindrical container.

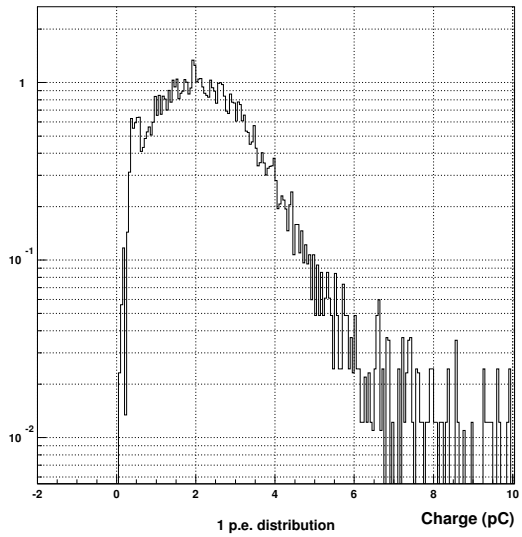

Figure 3.5: The charge distribution of single photo-electrons for the ID PMTs from the Ni-Cf calibration. The mean of the conversion factor is 2.055 pC/p.e.

of relative PMT timing is performed to make necessary corrections to the timing response. The timing difference originates from the length of the PMT signal cables as well as from the measured charge due to the discriminator effect known as slewing effect; a signal with greater light tends to exceed the threshold sooner than that with less light. Figure 3.6 shows a laser calibration system. A N_2 laser generates intense light of wavelength 337 nm with a very short time spread (< 3 ns), and using a dye laser module, the wavelength is shifted to 384 nm, around which the wavelength of Cherenkov light peaks. After the ND filter, the light is split into two; one is sent to the monitoring system and the other is injected via optical fiber into a light-diffuser ball, which is placed inside the Super-K tank. The diffuser ball is composed of a TiO_2 diffuser tip and LUDOX, silica gel made of 20 nm glass fragments as shown in Figure 3.6. The light is diffused by a combination of these two components without introducing significant timing spread. The PMT timing response is measured with various light intensity from 1 p.e. to a few hundreds of p.e. using an adjustable attenuation filter. The results are shown as a scatter plot of the timing and the charge called TQ-map in Figure 3.7. Each dot represents one measurement, and the open circles are the average timing with respect to charge for a PMT. The errors correspond to the timing resolution. Typical

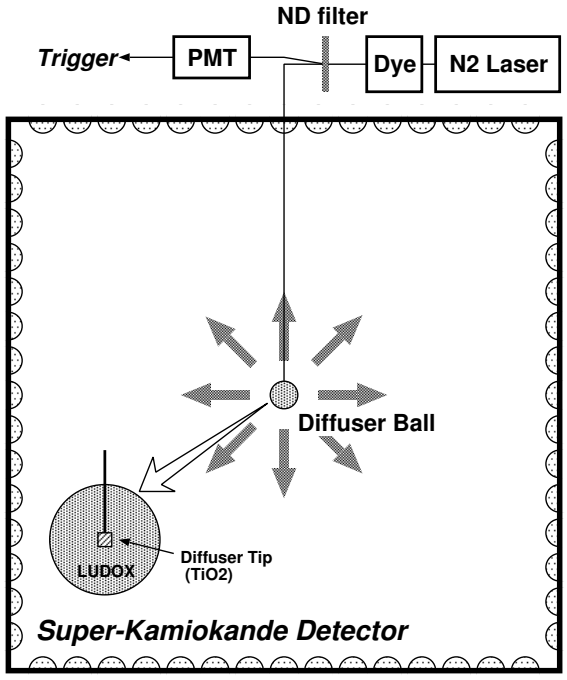

Figure 3.6: A schematic view of the laser calibration system for relative timing of the ID PMTs

timing resolution for a single p.e. is $\sim$3 ns as shown in Figure 3.8.

A TQ-map is made for every ID PMT, and the mean values are used in the data reduction process discussed in Chapter 5.

3.2 Water Transparency Measurement

The water transparency needs to be determined precisely and monitored since the number of Cherenkov photons detected by the PMTs varies through scattering and absorption depending on the transparency, which directly affects the measured energy. The light attenuation length is obtained and the time variation of water transparency is monitored.

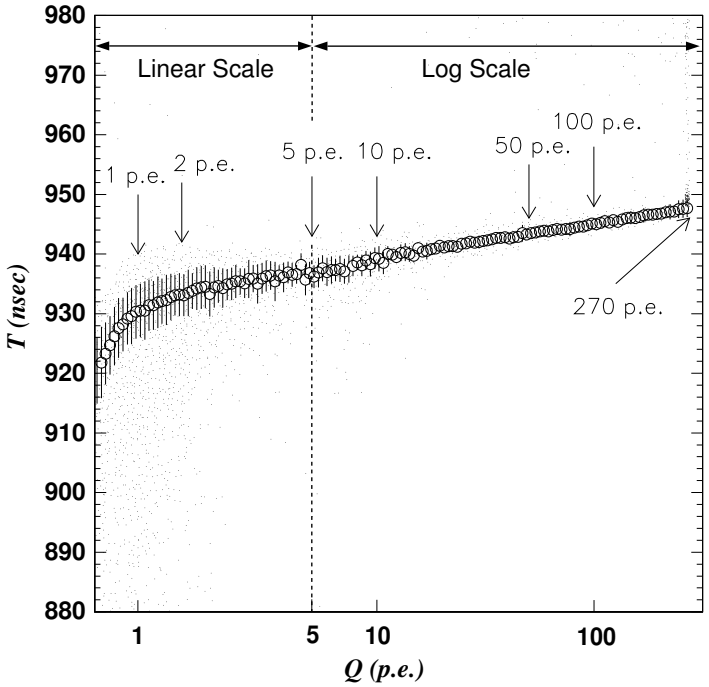

Figure 3.7: A distribution of a PMT timing response as a function of charge, TQ-map.

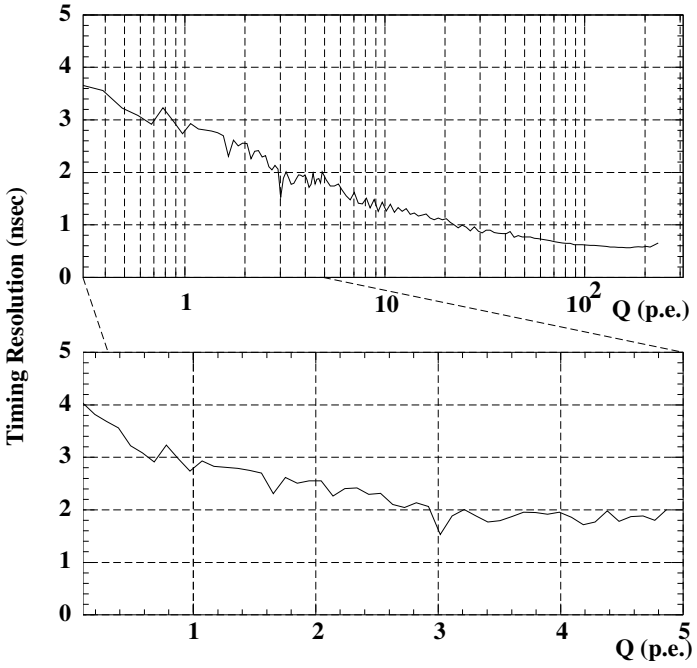

Figure 3.8: The timing resolution of the ID PMT as a function of the number of detected photoelectrons (p.e.). As the number of p.e. increases, the timing resolution gets better.

3.2.1 Light scattering measurement

The optical attenuation length in water is a result of both scattering and absorption :

$$I = I_0 \cdot \frac{1}{l^2} \cdot exp(-l/L_{atten}) \tag{3.2}$$

$$L_{atten} = \frac{1}{\alpha_{abs} + \alpha_{scat}}, \tag{3.3}$$

where I is the light intensity at distance l from a source, L_{atten} is the attenuation length, and α_{abs} and α_{scat} are the coefficient of absorption and scattering, respectively. To measure the coefficients α_{abs} and α_{scat} separately, dye and N_2 lasers with the different wavelengths of 337, 371, 400 and 420 nm are used as light sources. A schematic view of the setup is shown in Figure 3.9. The light from the laser is brought via optical fibers into the Super-K tank. Each laser fires every 6 seconds during normal data-taking. A typical laser event is also shown in Figure 3.9. Unscattered photons hit the PMTs directly at the bottom of the tank, which is observed as a cluster of hit PMTs. The total charge in this cluster is used for normalization. The remaining PMT hits on the barrel and top of the tank are due to the photons, which are scattered in the water and/or reflected by the PMTs on the bottom of the tank. For the measurement, the detector is divided into 6 regions; top and five equally divided barrel regions. The time distribution of the hit PMTs are compared between data and the Monte Carlo simulation (the Monte Carlo simulation will be described in Chapter 4). The plots in Figure 3.10 show the photon arrival-time distributions for both data and the MC. The first broad peaks are from scattered photons, and the second peaks around 1,100 ns are from photons reflected by the bottom PMTs or the black sheets. In the Monte Carlo simulations, both the scattering and absorption coefficients are tuned so that the data and the Monte Carlo agree, and with these measured (tuned) coefficients, the attenuation length in water is calculated by Equation 3.3. The attenuation length coefficients (L^{-1}) for each wavelength are plotted in Figure 3.11.

3.2.2 Time variation of Water Transparency

The water transparency is also monitored continuously by using cosmic ray muons passing through the detector, "through-going muons". The rate of cosmic ray muons at Super-K is about 2.2 Hz. Since these muons are abundant and energetic enough to deposit almost constant ionization energy per unit path length ($\sim$2 MeV/cm), they can be used as a good calibration source.

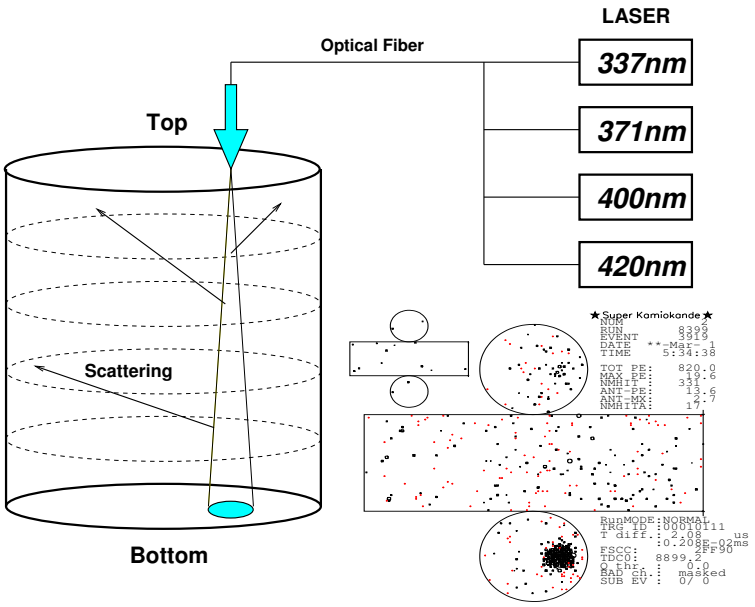

Figure 3.9: A schematic view of the laser calibration system for water transparency measurement (scattering and absorption), and a typical laser event.

Assuming that Cherenkov light emitted by muons is not scattered, the charge Q_i observed by the i-th PMT is given by:

$$Q_i = Q_0 \cdot \frac{f(\theta_i)}{l} \cdot \exp\left(-\frac{l_i}{L}\right) \tag{3.4}$$

where Q_0 is a constant, $f(\theta_i)$ is the PMT acceptance (see Figure 3.2), l_i is the photon path length, and L is the attenuation length.

Figure 3.12 shows the effective observed charge ($Ql/f(\theta)$) as a function of the path length l for the data obtained in a typical run. The resulting attenuation length is found to be 105.4 ± 0.5 m. Also, Figure 3.13 shows the time variation of the water attenuation length monitored continuously during the period for SK-I. For physics analyses, the time variations are corrected with the calibration data during the event reconstruction process.

3.3 Absolute Energy Calibration

The energy of charged particles is determined by the number of Cherenkov photons detected by each hit PMTs. Since there are no mono-energetic calibration sources for a few tens of MeV to GeV energy range, i.e. for atmospheric

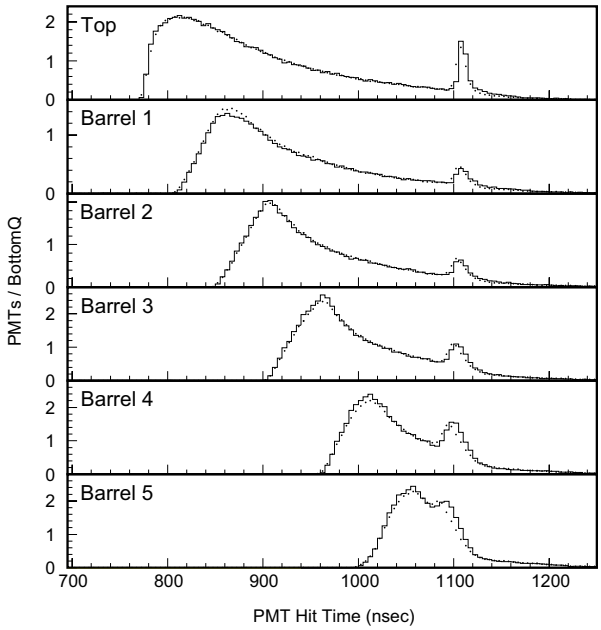

Figure 3.10: The arrival-time distributions for 337 nm-laser events in each region of the detector for the data (dots) and the Monte Carlo (histograms) events. The first peaks are from scattered photons, and the second peaks near 1,100 nm are from reflections by the bottom PMTs and the black sheets.

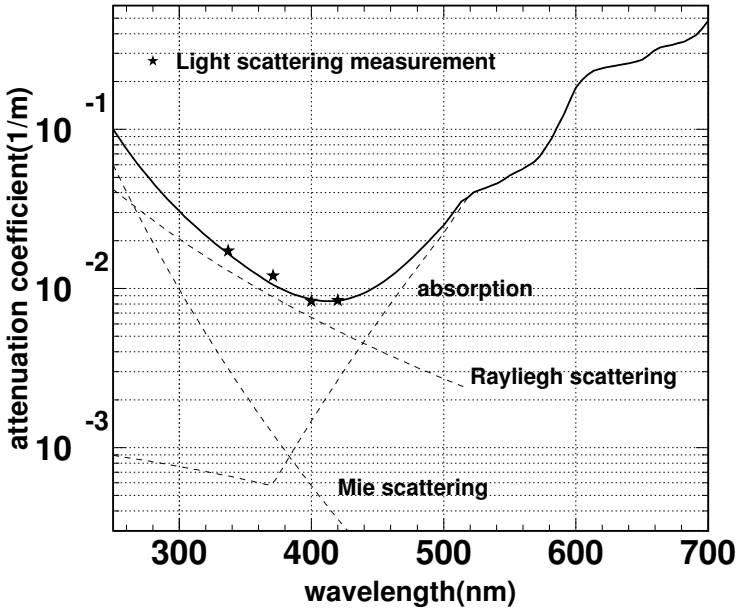

Figure 3.11: Attenuation coefficients ($L_{\rm atten}^{-1}$) as a function of wavelength for data (star) and the Monte Carlo (solid line), which is a combination of absorption and scattering (dotted lines).

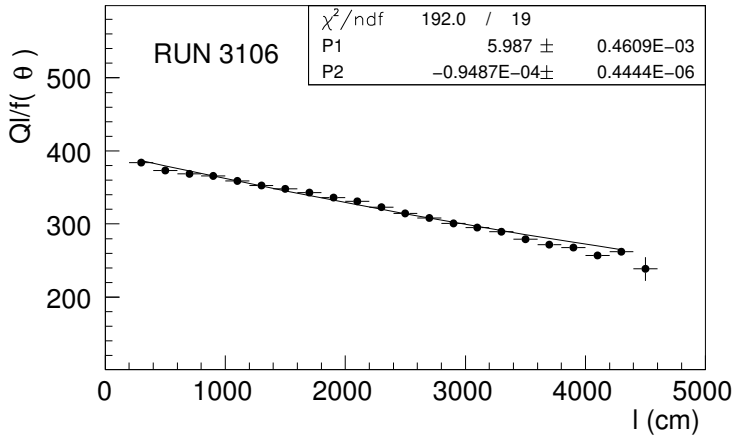

Figure 3.12: Effective observed charge as a function of the path length.

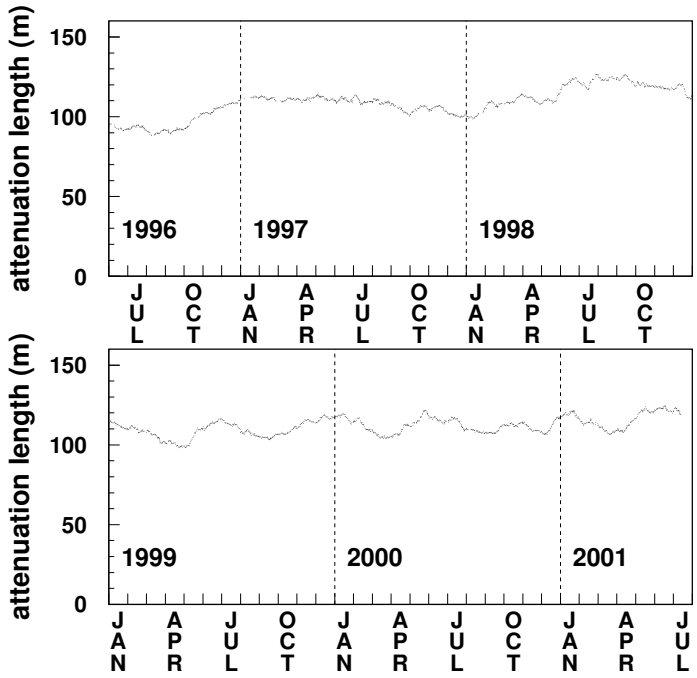

Figure 3.13: Time variation of water attenuation length.

neutrino analyses, such an estimate must rely on Monte Carlo simulations. For low energy events such as solar/supernova neutrinos events, an electron linear accelerator is used as a calibration source of mono-energetic electrons as briefly described in Section 3.4. The absolute energy calibration can provide precise tuning for Monte Carlo simulations to estimate the energy (or momentum) of the events. There are four sources for these calibrations; decay electrons from cosmic ray muons, which stop inside the ID detector, neutrino-induced π^0's, low and high energy cosmic ray muons.

3.3.1 Decay electron measurement

When cosmic ray muons stop inside the Super-K detector, "decay electrons" (electrons or positrons) are produced via decay of:

$$\mu^- \rightarrow e^- + \bar{\nu}_e + \nu_\mu$$

$$\mu^+ \rightarrow e^+ + \nu_e + \bar{\nu}_\mu$$

These decay electrons have the energy of $30 \sim 50$ MeV and are used to determine the absolute energy scale by comparing the energy spectrum for the data and the Monte Carlo simulation. The momentum spectrum of decay electrons is shown in Figure 3.14. In the Monte Carlo simulation, the measured μ^+/μ^- ratio of 1.37 is used [73], and also the effect of μ^- capture by oxygen nuclei is taken into account.

3.3.2 Neutrino-induced π^0 measurement

Neutral pions (π^0) produced in the interactions of the atmospheric neutrinos with water are used for the energy scale calibration in the energy range of several hundred MeV. Since π^0 decay immediately into two γ's, the invariant mass of π^0 can be reconstructed by obtaining the momentum of two γ's and the angle between them as:

$$M^2_{\pi^0} = 2p_{\gamma 1}p_{\gamma 2}(1 - cos\theta) \tag{3.5}$$

where $p_{\gamma 1}$ and $p_{\gamma 2}$ are the momentum of each γ. The distribution of the neutrino-induced π^0 invariant mass is shown in Figure 3.15. The difference of the π^0 peak positions for data and the Monte Carlo is within 2 %.

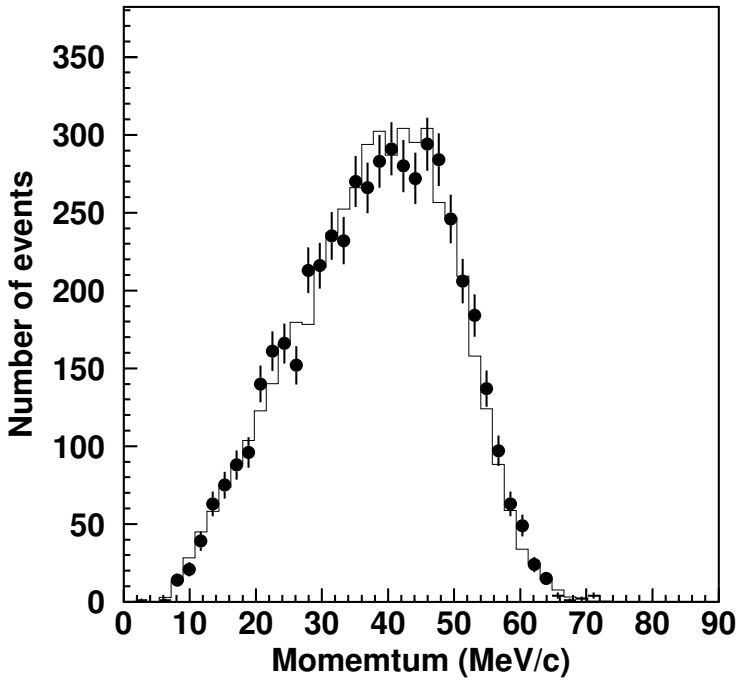

Figure 3.14: The momentum spectrum of decay electrons for the data (dots) and the Monte Carlo simulation (line).

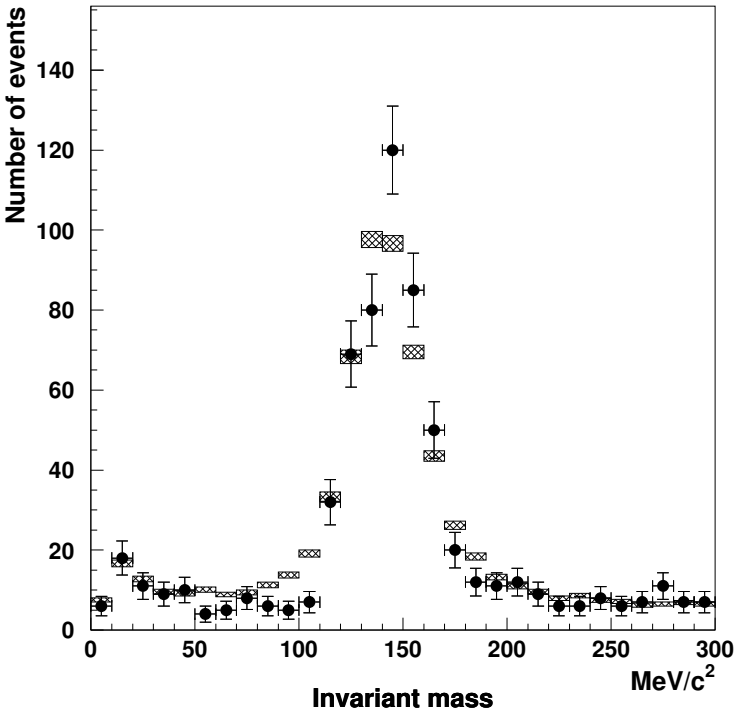

Figure 3.15: The distribution of neutrino-induced π^0 invariant mass for the data (dots) and the Monte Carlo predictions (boxes).

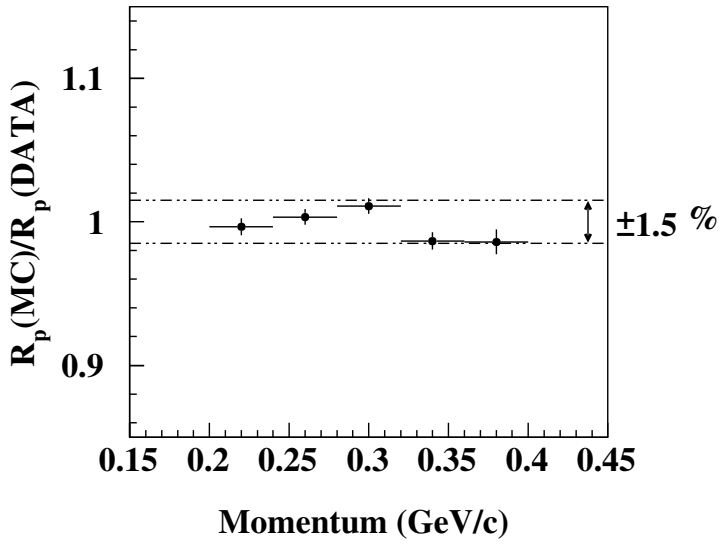

Figure 3.16: The double ratio of R, the momentum measured from charge information to that calculated from the Cherenkov angle, for the data and the Monte Carlo prediction.

3.3.3 Cosmic ray stopping muon measurement

Low energy stopping muon

The Cherenkov angle, θ_c of charged particles can be expressed as a function of momentum :

$$\cos\theta_c = \frac{1}{n\beta} = \frac{1}{n}\sqrt{1+\frac{m^2}{p^2}} \tag{3.6}$$

where θ_c, n, β, m and p are the Cherenkov angle, the index of refraction for water, v/c, mass and momentum. For low energy stopping muons with the momentum $< 400\,\mathrm{MeV/c}$, the Cherenkov angle has a large dependence on their momenta, and thus the momentum can be estimated by measuring the Cherenkov angle. For high energy muons ($\beta \approx 1$), the angle reaches the maximum ($\approx 42^\circ$).

The ratio of the momentum measured from detected charge to the momentum calculated from the Cherenkov angle can be compared between the data and the expectations from Monte Carlo simulation. Figure 3.17 shows the ratio of the momenta as a function of the momentum calculated from the Cherenkov angle. The agreement is within 1.5 %.

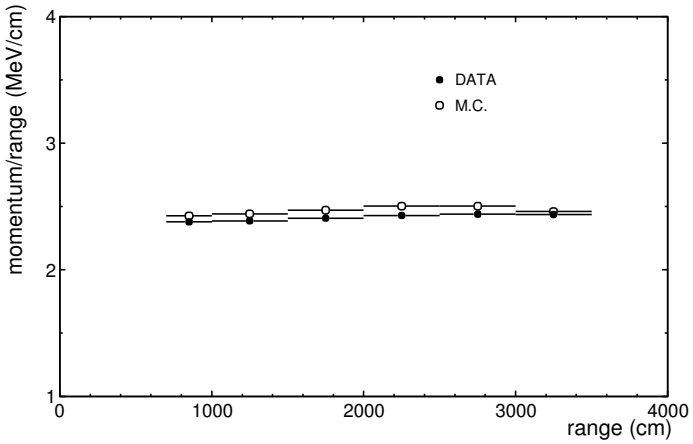

Figure 3.17: The ratio of the momentum to the range as a function of the range for high energy stopping muons.

High energy stopping muon

The momentum for high energy stopping muons can be calculated by their track length (range) in the Super-K detector since the range is approximately proportional to the momentum. The energy scale, which can be calibrated by this measurement, is from 1 GeV/c to 10 GeV/c. This calibration is most relevant for the tau neutrino appearance analysis since the energy of the events used in the analysis is greater than a few GeV. The range of stopping muons is the estimated distance from the entry point of a muon to the stopping point, which is obtained by finding a vertex position of the subsequent decay electron. Figure 3.17 shows the ratio of momentum to range as a function of range. Although the measured ratio is lower than the Monte Carlo expectations, the deviation over the range is less than 1 %.

All of the four absolute energy calibrations are summarized in Figure 3.18. The energy scale is calibrated for the energy range from a few tens MeV to 10 GeV. The data agree with the Monte Carlo predictions within 2 %.

3.3.4 Time variation of energy scale

The stability of the energy scale is also monitored continuously using stopping muons and the decay electrons. Figure 3.19 shows the time variation of the ratio of the average estimated energy of stopping muons to the range and

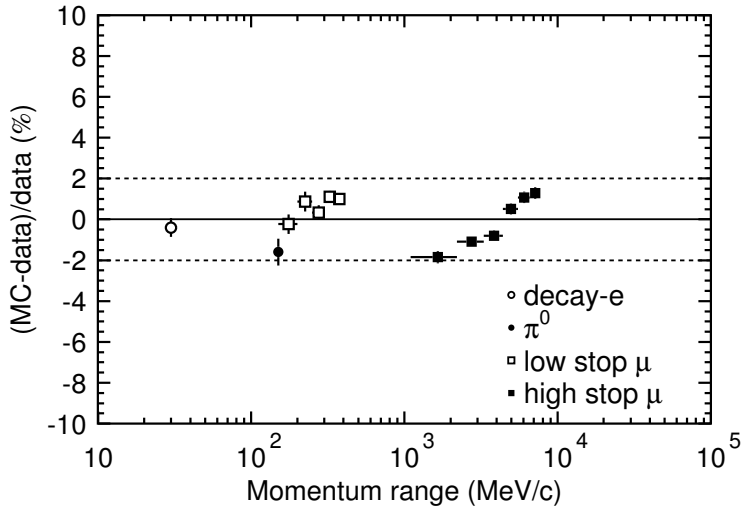

Figure 3.18: The absolute energy scale calibration from each calibration source. The difference between data and the Monte Carlo is within 2 %.

the mean decay electron energy as a function of elapsed days. For each plot, the energy is normalized to the mean values. The RMS of the energy scale variation is $\pm 0.9\%$.

3.4 Calibrations for low energy events

For low energy events such as solar, supernova, and supernova relic neutrinos, the energy scale calibrations need to be performed in the range of a few MeV. Since these calibrations are not relevant in this thesis, the details are not discussed. The following list summarizes the calibration methods and energy range. The precise calibrations at low energy show good agreement in the absolute energy scale within <1 %. The details can be found in Ref. [58].

- LINAC (Electron linear accelerator) [75]: Energy, angular, and vertex resolution for the energy range of $5 \sim 16$ MeV
- Cosmic ray muon spallation events: Time variation, position and directional dependence for the energy range of $3 \sim 21$ MeV.
- DTG (Deuterium-tritium neutron generator) (^{16}N) [76]: Directional dependence for the energy range of $5 \sim 10$ MeV.

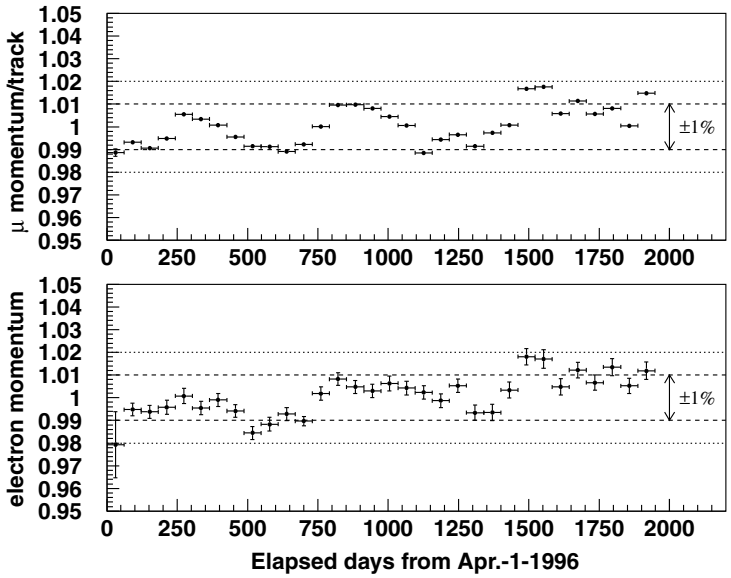

Figure 3.19: The time variation for the ratio of the average estimated energy of stopping muons to the range (top) and the mean decay electron energy (bottom) as a function of elapsed days. The vertical axis is the energy normalized by the mean value.

Chapter 4

Simulation

Atmospheric neutrino and tau neutrino events in Super-Kamiokande are modeled using Monte Carlo (MC) simulations. The MC simulations consists of three components; atmospheric neutrino flux, neutrino interactions, and detector simulation. The neutrino flux calculated by a few theoretical groups are used in the simulation. For neutrino interactions, a program called NEUT, originally developed for the Kamiokande experiment is used to simulate various neutrino interactions. The cross section for each interaction is taken from previous experimental results and theoretical models. The detector simulation is composed of the propagation of particles, the generation and propagation of Cherenkov photons, and the PMT response as well as the Super-K electronics.

Although tau neutrinos (ν_τ) from neutrino oscillations are originating from "atmospheric"neutrinos, throughout the thesis, atmospheric neutrinos refer to only ν_e and ν_μ. Tau neutrinos discussed in this thesis indicate those from the atmospheric neutrino oscillations. Tau neutrinos produced in the atmosphere are negligible as described in Section 4.1. The MC simulation procedures are the same for SK-I and SK-II.

4.1 Atmospheric Neutrinos

Atmospheric neutrinos are produced through successive interactions originating from the cosmic rays flying into the atmosphere of the Earth as explained in Chapter 1. For the precise atmospheric neutrino flux calculations, the primary cosmic ray flux, the atmospheric density structure, the hadron interactions, the geomagnetic effect, and solar modulations need to be taken into account. In this section, the mechanism of atmospheric neutrino production, how the atmospheric neutrino flux is calculated, is described.

There have been several atmospheric neutrino flux models developed by

theoretical groups such as Honda flux (M. Honda *et al.*) [77, 78, 79], Bartol flux (G. Barr *et al.*) [80, 81], and Fluka flux (G. Battistoni *et al.*) [82]. In our Monte Carlo simulation program, the Honda flux [79] is used primarily, and two other flux calculations [81, 82] are used to estimate the systematic uncertainty in the flux calculation. These models are developed specifically for the Kamioka site.

The primary cosmic rays are the ionized nuclei: protons ($\sim 95.2\,\%$), helium ($\sim 4.5\,\%$), and CNO nuclei ($\sim 0.3\,\%$) for the energy above 2 GeV/nucleus [77]. Figure 4.1 shows the summary of many experimental measurements for the flux of the primary cosmic ray protons [79]. The atmospheric neutrinos with energy of $\sim$1 GeV ($\sim$10 GeV) originate from the primary cosmic rays with $\sim$10 GeV ($\sim$100 GeV). The cosmic ray flux changes depending on the turbulence of the solar wind (solar modulation), which is higher when the solar activities are high (solar maximum) than when the solar activities are low (solar minimum). The difference in the flux between the solar maximum and the solar minimum is approximately a factor of two for 1 GeV protons and 10 % for 10 GeV protons. This causes about a few % difference in the absolute neutrino flux in 1 GeV energy range. The geomagnetic field is also a source of the modulation in the cosmic ray flux. Since the primary cosmic rays are charged, the geomagnetic field can filter out lower energy (< 10 GeV) particles by the rigidity (= momentum/charge) cutoff. Figure 4.2 shows the rigidity cutoff viewed from the Kamioka site [83]. For high energy cosmic rays above 100 GeV, the flux is not affected by the rigidity cutoff nor the geomagnetic field. The geomagnetic field produces a strong azimuthal asymmetry at the Kamioka site, called "East-West effect", (which was the first indicator for the positive charge of the cosmic rays [84, 85]) as shown in Figure 4.2. Using the atmospheric neutrinos, the East-West effect was observed by Super-K, which confirmed the effect of the geomagnetic field [86].

The US standard Atmosphere model [101] is employed for the density structure of the atmosphere of the Earth, and the structure gives the zenith angle dependence of the atmospheric neutrinos.

For the hadronic interactions of the cosmic rays with air nuclei, the two theoretical models, NUCRIN [102] and DPMJET-III [103] are used for the cosmic ray energies less than 5 GeV and greater than 5 GeV respectively [79]. Through the interactions, mostly charged pions and some kaons are produced. Then, they decay into muons and neutrinos. The propagation and the decay of the secondary cosmic rays are also simulated. The flux of these secondary cosmic ray muons have been measured by several experiments such as BESS [104]. The hadronic interaction model used in the Honda flux calculation agree with the observation as shown in Figure 4.3.

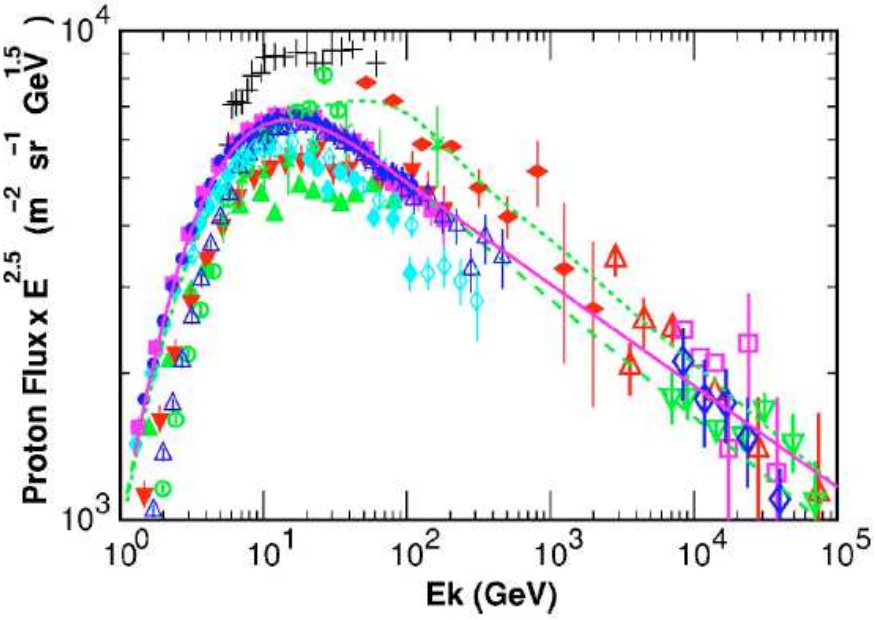

Figure 4.1: Primary cosmic ray measurements and the model used in Honda flux calculation [79]. The data are taken from Webber *et al.* [87] (crosses), MASS [88] (open circles), LEAP [89] (closed upward triangles), IMAX [90] (closed downward triangles), CAPRICE-94 [91] (closed vertical diamonds), CAPRICE-98 [92] (open vertical diamonds), BESS [93] (closed circles), BESS-TeV [94] (open upward triangle), AMS [95] (closed horizontal diamonds), Ryan *et al.* [96] (closed horizontal diamonds), JACEE [97] (open downward triangles), RUNJOB [98] (open diamonds) Ivanenko *et al.* [99] (open upward triangles), and Kawamura *et al.* [100] (open squares). The solid line is the spectrum used in Honda flux.

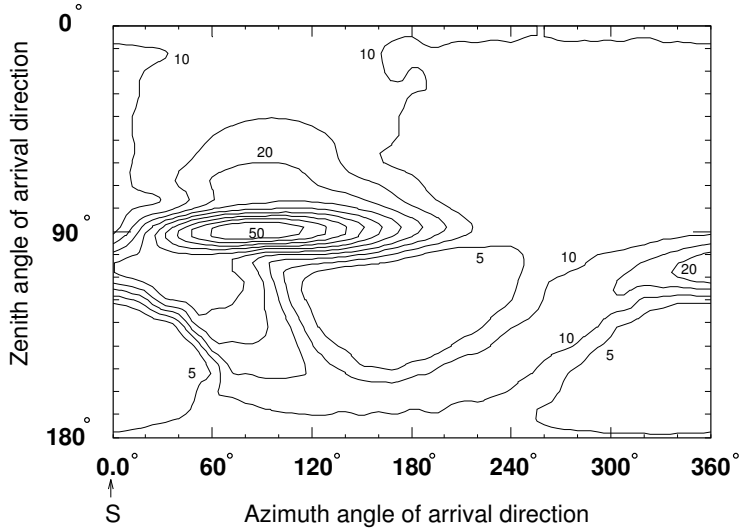

Figure 4.2: The rigidity cutoff viewed from the Kamioka site [83]. Azimuthal angles of 0°, 90°, 180°, 270° show direction to the south, east, north and west of the detector, respectively.

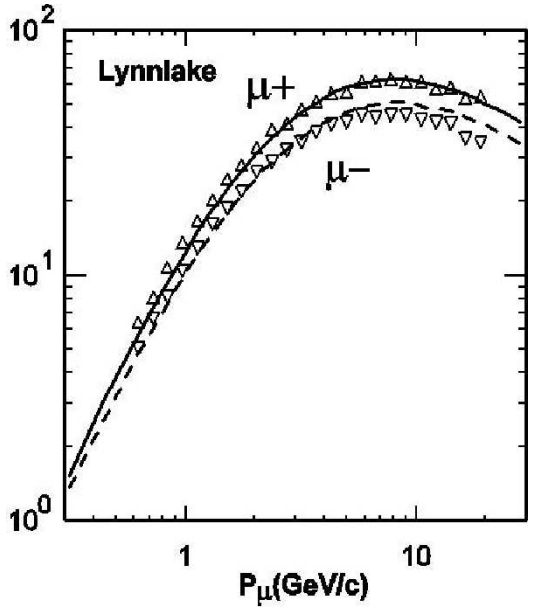

Figure 4.3: The flux of cosmic ray muons at Lynnlake. The data (triangle) are measured by the BESS experiment [104] and the prediction are calculated by the Honda flux [78].

The calculated energy spectrum of atmospheric neutrinos at Super-K for the Honda flux, Fluka flux, and Bartol flux is shown in Figure 4.4. The flavor ratio of $\nu_\mu + \overline{\nu}_\mu$ to $\nu_e + \overline{\nu}_e$ averaged over all of the directions as a function of neutrino energy is also shown in Figure 4.4. The flavor ratio is approximately two up to a few GeV energy regions as described in Section 1.4.1. As the neutrino energy increases, the flavor ratio becomes larger than two because more cosmic ray muons reach the ground before decaying. Although the absolute flux has a large uncertainty ($10\,\% \sim 20\,\%$), which is mostly due to the uncertainty in the absolute primary cosmic ray flux, the uncertainty in the flavor ratio is only a few %. For neutrinos with higher energy ($\sim 10\,\mathrm{GeV}$), the contribution of kaon decay in neutrino production is not negligible, and the uncertainty in the flavor ratio increases.

The zenith angle dependence of the atmospheric neutrino flux is shown in Figure 4.5, where $\cos\theta = -1$ refers to upward-going neutrinos and $\cos\theta = -1$ refers to downward-going neutrinos, and the characteristics of the flux distributions are the key for the atmospheric neutrino analyses in the Super-Kamiokande experiment. First, the enhancement of the flux near horizontal directions ($\sim \cos\theta = 0$) are due to the larger decay volume of cosmic ray muons. The cosmic ray muons coming in the horizontal direction travel for a longer distance than those in the vertical directions, and thus have higher probability to decay into neutrinos. Second, for higher energy neutrinos, the flux distribution is symmetric in upward-going and downward-going directions (up-down symmetry) as one would expect because the primary cosmic rays are coming into the atmosphere isotropically. This feature is crucial and independent of the details of the cosmic ray flux and their hadronic interactions in the atmosphere. For lower energy neutrinos, the flux shows up-down asymmetry. This is caused by the the geomagnetic field at the Kamioka site. The primary cosmic rays of the lower energy neutrinos are deflected by the rigidity cutoff. In the Super-K, the enhancement around the horizontal directions and slight up-down asymmetry for low energy neutrinos can not be observed since the angular correlation between neutrinos and leptons is small.

The atmospheric tau neutrinos, which are produced in the atmosphere (i.e. not from the oscillations), can be produced through the leptonic decay of D_s mesons produced in the interactions of the cosmic rays with air nuclei:

$$\begin{aligned} p(He) + A_{air} \;\; &\rightarrow \;\; D_s \;\; + X \\ &\quad\;\; \hookrightarrow \;\; \tau + \nu_\tau \\ &\qquad\;\; \hookrightarrow \;\; \nu_\tau + X' \end{aligned} \tag{4.1}$$

where X and X' are hadrons. The branching fraction of $D_s \rightarrow \tau + \nu_\tau$ is about

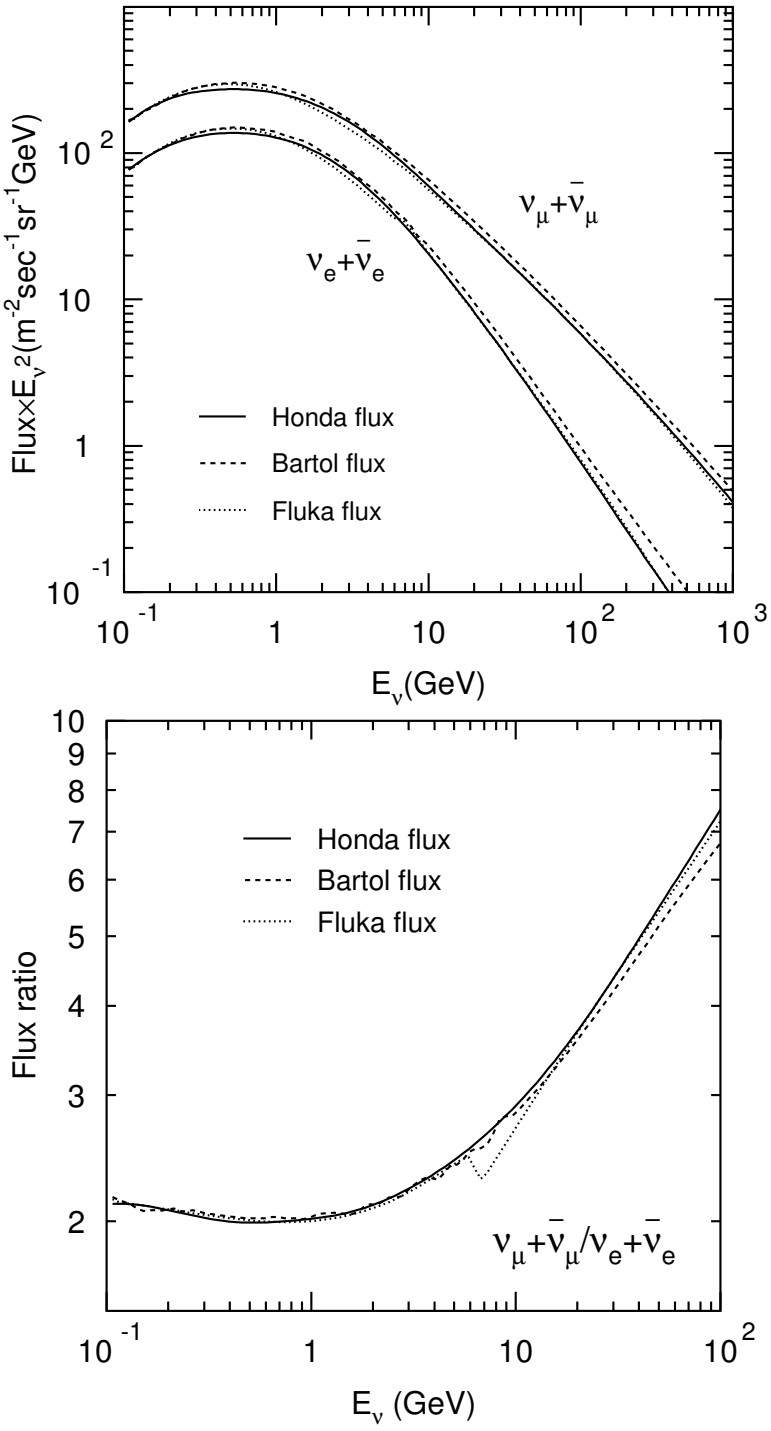

Figure 4.4: The absolute flux of atmospheric neutrinos for $\nu_\mu + \overline{\nu}_\mu$ and $\nu_e + \overline{\nu}_e$ and the flavor ratio of $\nu_\mu + \overline{\nu}_\mu$ to $\nu_e + \overline{\nu}_e$ averaged over all of the directions as a function of neutrino energy for the Honda flux (solid line), the Bartol flux (dashed line), and the Fluka flux (dotted line).

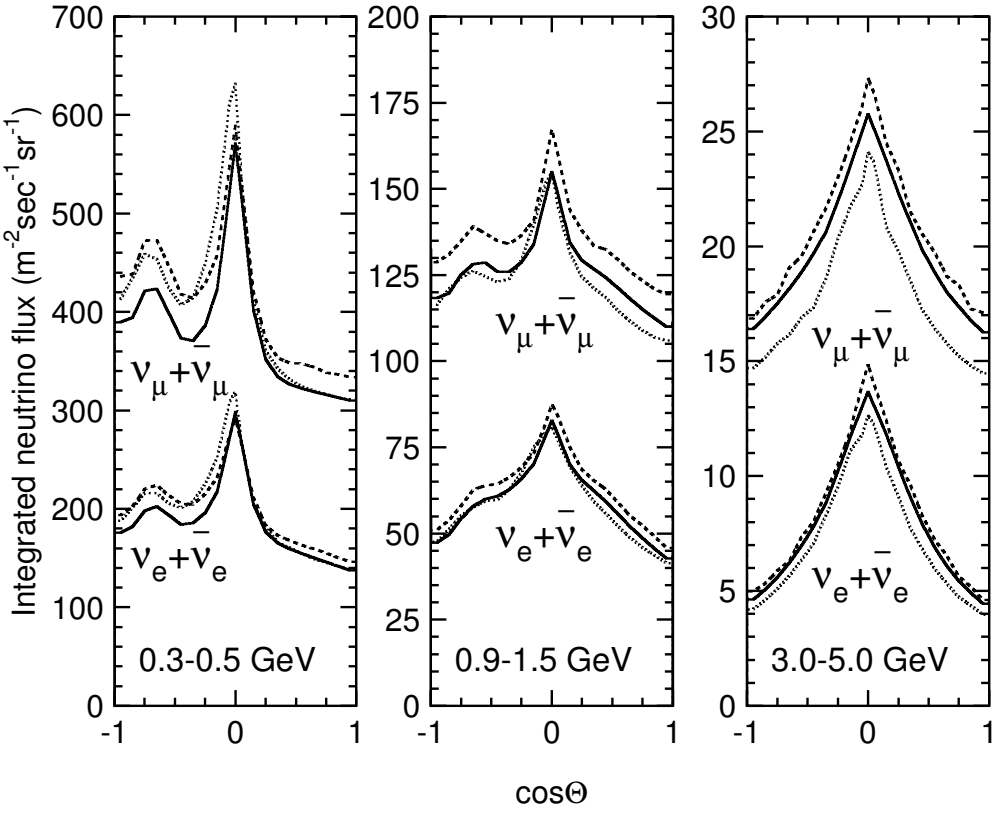

Figure 4.5: The atmospheric neutrino flux as a function of zenith angle for the Honda flux (solid line), the Bartol flux (dashed line), and the Fluka flux (dotted line). Zenith angle $\cos\Theta = -1(+1)$ indicates upward-going (downward-going).

4% [105]. The flux of atmospheric tau neutrinos is estimated to be about 10^{-6} times lower than that of muon neutrinos and electron neutrinos [106], and is negligible for the atmospheric neutrino oscillations and the tau neutrino appearance analyses. That is, tau neutrinos, if they were to be observed by an atmospheric neutrino experiment, would come from the atmospheric neutrino oscillations.

4.2 Neutrino Interactions (Cross Section)

Atmospheric neutrinos interact with water (i.e. nucleus, free protons, electrons) via weak interactions. In our Monte Carlo simulation, neutrino interactions are simulated by the neutrino interaction simulation library, NEUT [107], which was originally developed for the Kamiokande experiment. In this section, the details of cross section calculations in NEUT library are described. For consistency checks, another neutrino interaction model, NUANCE, is also employed in the analysis, its details can be found elsewhere [108].

In NEUT, the following charged and neutral current neutrino interactions are considered:

CC quasi-elastic scattering	$\nu + N \rightarrow\ l^{\pm} + N'$
CC single-meson production	$\nu + N \rightarrow\ l^{\pm} + N' + \text{meson}$
CC deep inelastic scattering	$\nu + N \rightarrow\ l^{\pm} + N' + \text{hadrons}$
CC coherent pion production	$\nu +\ ^{16}\text{O} \rightarrow\ l^{\pm} +\ ^{16}\text{O} + \pi^{\mp}$
NC elastic scattering	$\nu + N \rightarrow\ \nu + N$
NC single-meson production	$\nu + N \rightarrow\ \nu + N' + \text{meson}$
NC deep inelastic scattering	$\nu + N \rightarrow\ \nu + N' + \text{hadrons}$
NC coherent pion production	$\nu +\ ^{16}\text{O} \rightarrow\ \nu +\ ^{16}\text{O} + \pi^{0}$

where N and N' are nucleons, $l^{\pm}$ is a charged lepton. The calculation of the cross sections for each interaction is described in this sections. In our simulations, neutrino-electron elastic scattering is neglected since the cross section of neutrino-electron interactions is about 10^3 times smaller than neutrino-nucleon interaction cross sections at neutrino energy of $\sim$1 GeV.

4.2.1 Elastic and Quasi-elastic Scattering

The differential cross section of the charged current quasi-elastic scattering for free protons (i.e. hydrogen atom in water) is given by [109, 110] :

$$\frac{d\sigma^{\nu(\bar{\nu})}}{dq^2} = \frac{M^2 G_F^2 \cos^2\theta_c}{8\pi E_\nu^2}\left[A(q^2) \mp B(q^2)\frac{s-u}{M^2} + C(q^2)\frac{(s-u)^2}{M^4}\right] \tag{4.2}$$

where E_ν is the neutrino energy, M is the mass of the target nucleon, G is the Fermi coupling constant, θ_c is the Cabbibo angle, q is the four-momentum transfered of the lepton, and s and u are Mandelstam variables [109]. The factors A, B and C are :

$$\begin{aligned} A(q^2) &= \frac{m^2-q^2}{4M^2}\left[\left(4-\frac{q^2}{M^2}\right)|F_A|^2 - \left(4+\frac{q^2}{M^2}\right)|F_V^1|^2 \right. \\ &\quad - \frac{q^2}{M^2}|\xi F_V^2|^2\left(1+\frac{q^2}{4M^2}\right) - \frac{4q^2 F_V^1 \xi F_V^2}{M^2} \\ &\quad \left. - \frac{m^2}{M^2}\left((F_V^1+\xi F_V^2)^2 + |F_A|^2\right)\right] \qquad (4.3) \\ B(q^2) &= \frac{q^2}{M^2}\left(F_A(F_V^1+\xi F_V^2)\right) \qquad (4.4) \\ C(q^2) &= \frac{1}{4}\left(|F_A|^2 + |F_V^1|^2 - \frac{q^2}{4M^2}|\xi F_V^2|^2\right) \qquad (4.5) \end{aligned}$$

where m is the lepton mass, $\xi \equiv \mu_p - \mu_n = 3.71$. The vector form factors, $F_V^1(q^2)$ and $F_V^2(q^2)$, and the axial vector form factor, $F_A(q^2)$ are determined experimentally and are given by :

$$\begin{aligned} F_V^1(q^2) &= \left(1-\frac{q^2}{4M^2}\right)^{-1}\left[G_E(q^2) - \frac{q^2}{4M^2}G_M(q^2)\right] \qquad (4.6) \\ \xi F_V^2(q^2) &= \left(1-\frac{q^2}{4M^2}\right)^{-1}\left[G_E(q^2) - G_M(q^2)\right] \qquad (4.7) \\ F_A(q^2) &= -1.23\left(1-\frac{q^2}{M_A^2}\right)^{-2} \qquad (4.8) \\ G_E(q^2) &= (1+\xi)^{-1}G_M(q^2) = \left(1-\frac{q^2}{M_V^2}\right)^{-2} \qquad (4.9) \end{aligned}$$

where G_E and G_M are the electric and magnetic form factor, the vector mass M_V is set to be 0.84 GeV and the axial vector mass M_A is set to be 1.11 GeV from experimental data [111].

For scattering off nucleons in ^{16}O, the Fermi motion of the nucleons and Pauli exclusion principle must be considered [112]. Since nucleons are fermions, the outgoing momentum of the nucleons in the interactions is required to be greater than the Fermi surface momentum to allow quasi-elastic scattering to occur. In NEUT, the Fermi surface momentum is set to be 225 MeV/c.

The cross section for neutral current elastic scattering are estimated from the following relations [113, 114] :

$$\sigma(\nu p \to \nu p) = 0.153 \times \sigma(\nu n \to e^- p) \quad (4.10)$$

$$\sigma(\bar{\nu} p \to \bar{\nu} p) = 0.218 \times \sigma(\bar{\nu} p \to e^+ n) \quad (4.11)$$

$$\sigma(\nu n \to \nu n) = 1.5 \times \sigma(\nu p \to \nu p) \quad (4.12)$$

$$\sigma(\bar{\nu} n \to \bar{\nu} n) = 1.0 \times \sigma(\bar{\nu} p \to \bar{\nu} p) \quad (4.13)$$

Figure 4.6 shows the cross section of the quasi-elastic scattering for the experimental data and the calculation by the NEUT.

4.2.2 Resonant Single-Meson Production

The resonant single-meson production of π, K, and η are simulated by the Rein & Sehgal's model [121, 122], in which the intermediate baryon resonance is produced as :

$$\begin{array}{c} \nu + N \to l + N^* \\ N^* \to \text{meson} + N' \end{array} \quad (4.14)$$

where N and N' are nucleons and N^* is a baryon resonance. The dominant resonance and single-meson production is :

$$\begin{array}{c} \nu_\mu + p \to \mu^- + \Delta^{++}(1232) \\ \Delta^{++} \to p + \pi^+ \end{array} \quad (4.15)$$

The differential cross section of single-meson production is a product of the amplitude of each resonance production and the probability of the baryon resonance decay. For negligible decay width of a baryon resonance (N^*), the differential cross section is :

$$\frac{d^2\sigma}{dq^2 dE_\nu} = \frac{1}{32\pi M E_\nu^2} \cdot \frac{1}{2} \sum_{j,spin} \left| T(\nu N \to l N_j^*) \right|^2 \delta(W^2 - M_j^2) \quad (4.16)$$

where M is the mass of the target nucleon, E_ν is neutrino energy, W is the invariant mass of the hadronic system (or the mass of the intermediate baryon

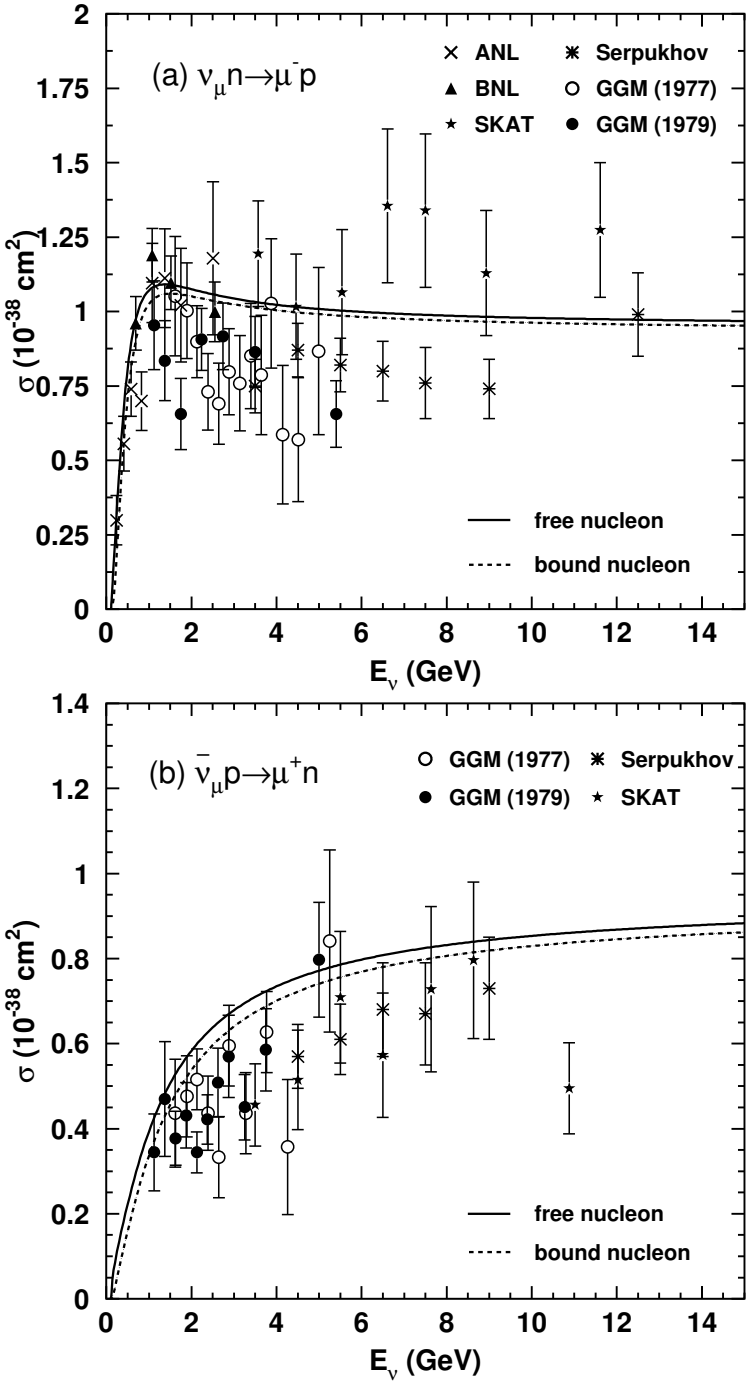

Figure 4.6: Cross sections of ν_μ and $\overline{\nu}_\mu$ for free nucleon target (solid lines) and bound nucleon target in ^{16}O. The experimental data are from ANL [115], Gargamelle [116, 117], BNL [118], Serpukhov [119] and SKAT [120].

resonance), M_j is the mass of the baryon resonance (N_j^*), and $T(\nu N \to lN^*)$ is the amplitude of resonance production, which is calculated using the FKR (Feynman-Kislinger-Ravndal) model [123]. The invariant mass, W, is restricted to be less than $2\,\mathrm{GeV/c^2}$. For W larger than $2\,\mathrm{GeV}$, the interactions are simulated as deep-inelastic scattering as described in Section 4.2.3. The differential cross-section for the resonance with finite decay width Γ can be derived by replacing the δ-function with a Breit-Wignar factor :

$$\delta(W^2 - M_j^2) \quad \to \quad \frac{1}{2\pi} \cdot \frac{\Gamma}{(W - M_j)^2 + \Gamma^2/4} \tag{4.17}$$

For a single-meson production, the axial vector mass M_A is also set to be $1.11\,\mathrm{GeV}$ experimentally [111]. Total of 18 resonances are simulated in our simulation. The Pauli blocking effect in the decay of the baryon resonance is considered by requiring the momentum of the nucleon to be greater than the Fermi surface momentum. Pion-less decay of Δ resonance in ^{16}O nuclei, where about 20 % of the events don't have a pion in the decay, is also simulated [124]. Figure 4.7 and Figure 4.8 show the cross sections of charged current and neutral current resonant single-meson productions for our calculations and the experimental data.

4.2.3 Deep-inelastic Scattering

The cross section of deep-inelastic scattering is calculated by the GRV94 parton distribution function [131]. The differential cross section of charged current deep-inelastic scattering for the hadronic invariant mass $W > 1.3\,\mathrm{GeV/c^2}$ is [133] :

$$\begin{aligned}
\frac{d^2\sigma^{\nu,\bar{\nu}}}{dxdy} &= \frac{G_F^2 M E_\nu}{\pi}\left((1 - y + \frac{y^2}{2} + C_1)F_2(x,q^2) \pm y(1 - \frac{y}{2} + C_2)xF_3(x,q^2)\right) \\
C_1 &= \frac{yM_l^2}{4ME_\nu x} - \frac{xyM}{2E_\nu} - \frac{m_l^2}{4E_\nu^2} - \frac{m_l^2}{2ME_\nu x} \\
C_2 &= -\frac{m_l^2}{4ME_\nu x}
\end{aligned} \tag{4.18}$$

where M is the nucleon mass, m_l is the outgoing lepton mass. The variables $x = -q^2/(2M(E_\nu - E_l))$ and $y = (E_\nu - E_l)/E_\nu$ are Bjorken scaling parameters, where E_ν and E_l are the energy of incoming neutrino and outgoing lepton in the laboratory frame, respectively, and the nucleon structure functions F_2 and xF_3 are taken from GRV94 [131].

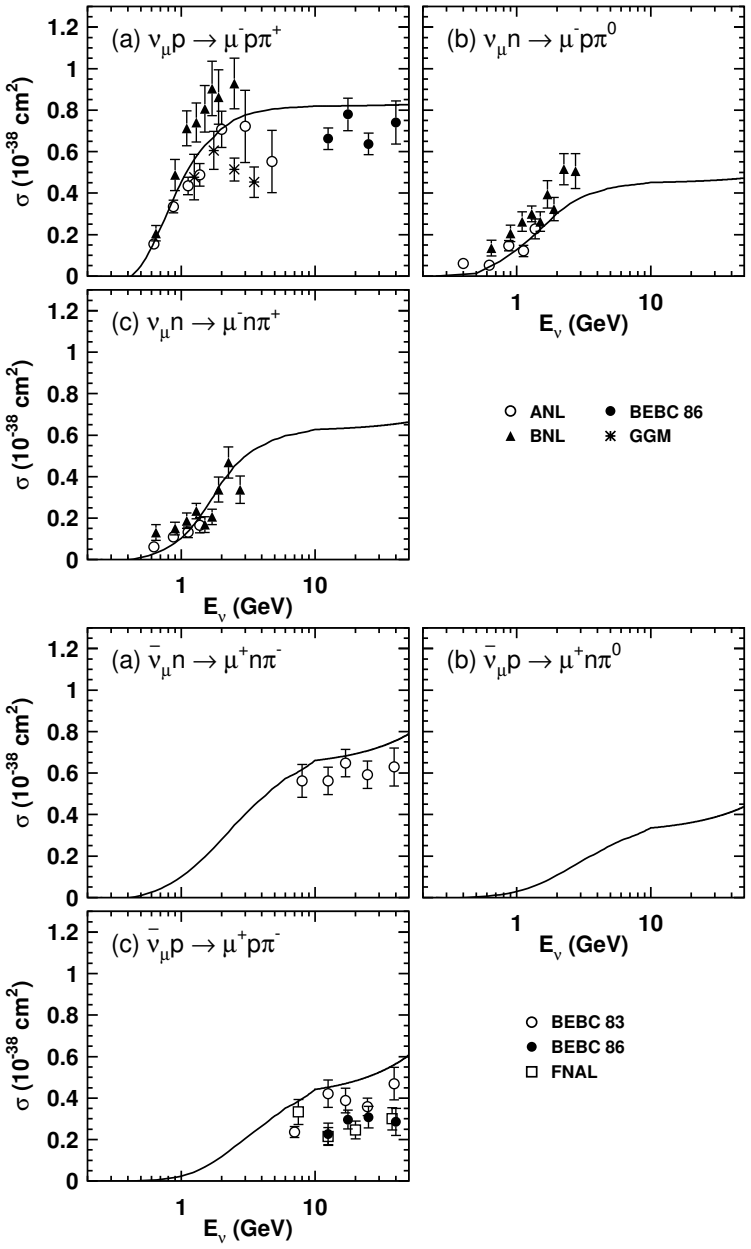

Figure 4.7: Cross sections of charged current single-meson productions for ν_μ (top) and $\overline{\nu}_\mu$ (bottom). The experimental data are from ANL [125], BNL [126], BEBC [127] and Gargamelle [128] for ν_μ (top) and BEBC [127, 129] and FNAL [130] for $\overline{\nu}_\mu$ (bottom). The solid lines are the cross section calculated by our simulation.

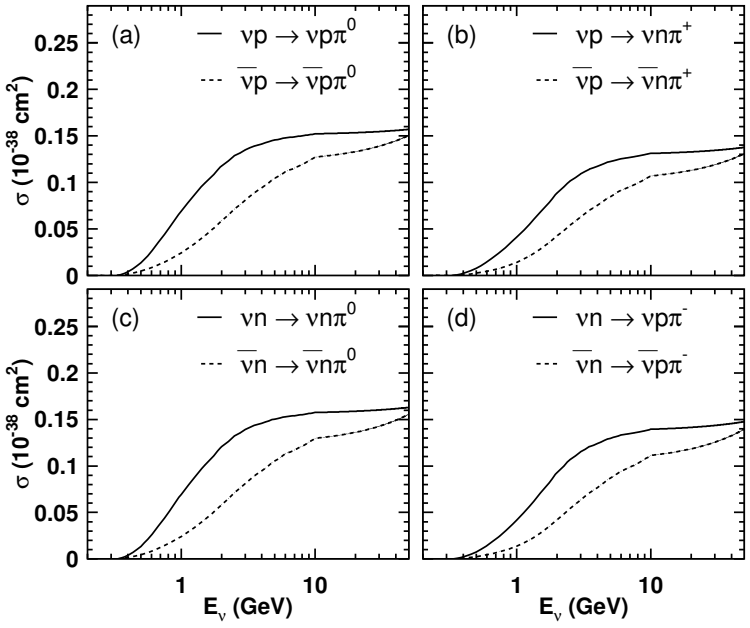

Figure 4.8: Cross sections of neutral current resonant single-meson production. The solid (dashed) lines are the cross section for ν_μ ($\overline{\nu}_\mu$) calculated by our simulation.

For $1.3\,\mathrm{GeV} < W < 2.0\,\mathrm{GeV}$, a custom-made program is used, in which the final state hadrons are set to be only pions [134]. The mean multiplicity of pions is estimated using the Fermilab 15-foot bubble chamber experiment [135] :

$$\langle n_\pi \rangle = 0.09 + 1.83 \ln(W^2). \tag{4.19}$$

For an individual Monte Carlo event, the number of pions is determined by using KNO (Koba-Nielsen-Olsen) scaling [136]. The multiplicity of pions are restricted to $n_\pi \geq 2$ since single-pion production is separately simulated as described in Section 4.2.2. The forward-backward asymmetry of pion multiplicity in the hadronic center of mass system is included using the results from BEBC experiment [137] :

$$\frac{n_\pi^F}{n_\pi^B} = \frac{0.35 + 0.41 \ln(W^2)}{0.5 + 0.09 \ln(W^2)} \tag{4.20}$$

For neutral current interactions, the cross section in the $1.3\,\mathrm{GeV} < W < 2.0\,\mathrm{GeV}$ energy range is determined using the following relations estimated from experimental results [138, 139] :

$$\frac{\sigma(\nu N \to \nu X)}{\sigma(\nu N \to \mu^- X)} = \begin{cases} 0.26 & (E_\nu < 3\,\mathrm{GeV}) \\ 0.26 + 0.04\,(E_\nu/3 - 1) & (3 \leq E_\nu < 6\,\mathrm{GeV}) \\ 0.30 & (E_\nu \geq 6\,\mathrm{GeV}) \end{cases} \tag{4.21}$$

$$\frac{\sigma(\bar{\nu} N \to \bar{\nu} X)}{\sigma(\bar{\nu} N \to \mu^+ X)} = \begin{cases} 0.39 & (E_\nu < 3\,\mathrm{GeV}) \\ 0.39 - 0.02\,(E_\nu/3 - 1) & (3 \leq E_\nu < 6\,\mathrm{GeV}) \\ 0.37 & (E_\nu \geq 6\,\mathrm{GeV}) \end{cases} \tag{4.22}$$

For the hadronic invariant mass W greater than $2.0\,\mathrm{GeV/c^2}$, the kinematics of the hadronic system is calculated by PYTHIA/JETSET package [132], in which not only pions but also other mesons such as K, η, ρ are considered.

Total charged current cross sections including quasi-elastic scattering, resonant single-meson productions, and deep-inelastic scattering for neutrinos and anti-neutrinos are shown in Figure 4.9.

4.2.4 Coherent Pion Production

The coherent pion production is a neutrino interaction with a oxygen nucleus, which remains intact, and one pion with the same charge as the incoming weak current is produced. Since very little momentum is transferred to the oxygen nucleus, the angular distributions of the outgoing leptons and pions

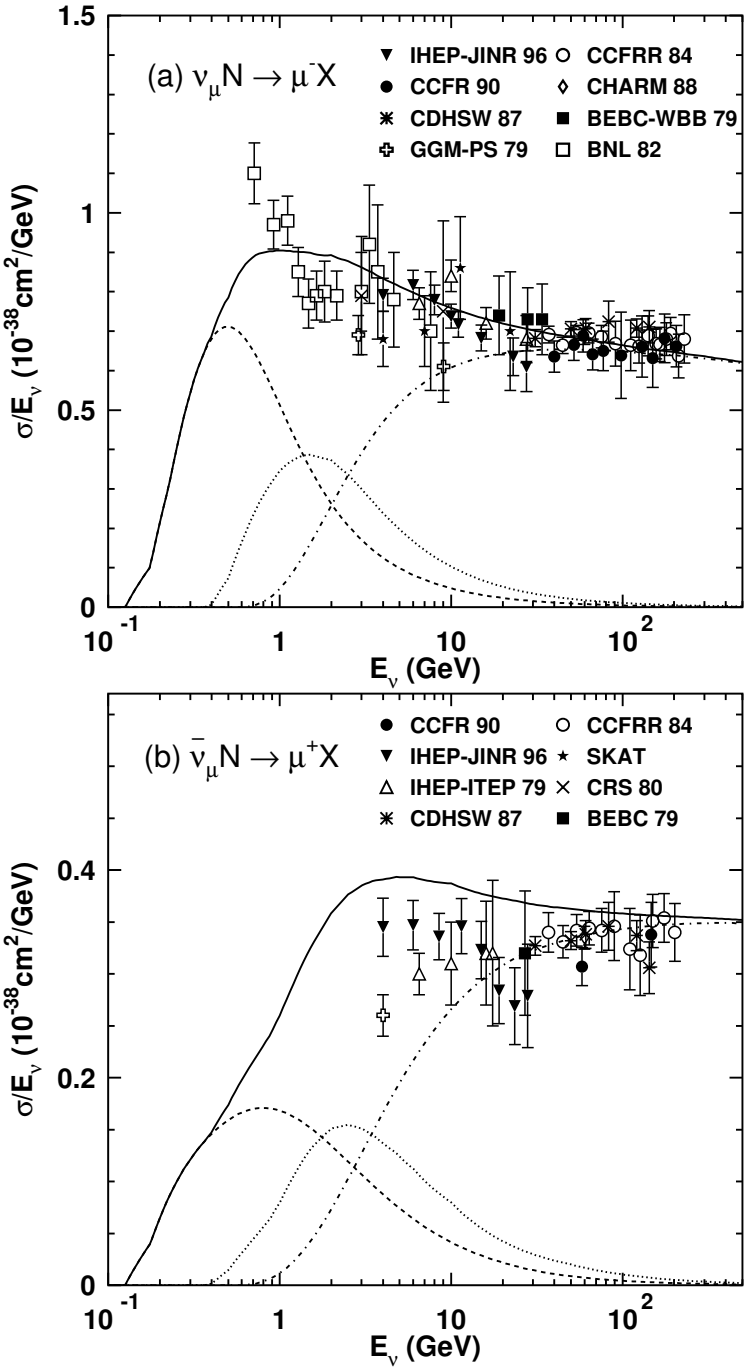

Figure 4.9: Total cross sections of charged current divided by E_ν for (a) ν_μ and (b) $\overline{\nu}_\mu$. The solid line shows the calculated cross section. The dashed, dotted, and dash-dotted lines show quasi-elastic scattering, resonant single-meson productions, and deep inelastic scattering, respectively. The experimental data are taken from IHEP-JINR [140], CCFR [141], CDHSW [142], Gargamelle [143, 144], CHARM [145], CRS [146], BEBC-WBB [147], BNL [148], IHEP-ITEP [149], CCFRR [150] and SKAT [151].

are peaked in the forward direction. The formalism developed by Rein and Sehgal [152] is used to simulate the interactions, and the differential cross section is given by :

$$\begin{aligned}\frac{d^3\sigma}{dQ^2dydt} &= \beta \times \frac{G_F^2 M}{2\pi^2} f_\pi^2 A^2 E_\nu (1-y) \frac{1}{16\pi} (\sigma_{total}^{\pi N})^2 \\ &\quad \times (1+r^2)(\frac{M_A^2}{M_A^2+Q^2})^2 e^{-b|t|} F_{abs} \qquad (4.23) \\ r &= Re(f_{\pi N}(0))/Im(f_{\pi N}(0)) \qquad (4.24)\end{aligned}$$

where β is the axial vector couping constant and is 1 (2) for neutral current (charged current) interactions, G_F is the weak coupling constant, M is the nucleon mass, f_π is pion decay constant and is $0.93\, m_\pi$, A is the atomic number ($=16$ for oxygen), E_ν is the neutrino energy, y is the lepton fractional energy loss, $\sigma_{total}^{\pi N}$ is the averaged pion-nucleon cross section, b is in the order of the nucleus transverse dimensions and is $80\,\mathrm{GeV}^{-2}$, M_A is the axial-vector mass, Q^2 is the square of the four–momentum transfer of the lepton, and t is the square of the four-momentum transfer to the nucleus, F_{abs} is a factor to account for the absorption of pions in the nucleus. $f_{\pi N}(0))$ in r is the πN scattering amplitude. The cross sections of the coherent pion production for the CC and NC interactions are shown in Figure 4.10.

4.2.5 Nuclear Effect

It is also important to simulate the secondary interactions of mesons produced in neutrino interactions with nucleons inside the ^{16}O nuclei. All of the mesons produced within the ^{16}O nuclei are tracked from their production points until they exit or are absorbed in the nuclei. This is done for π, K, η, and ω by using a cascade model in our simulation. The interactions of pions are especially important since the cross section for pion productions are large for $E_\nu > 1\,\mathrm{GeV}$, and the pion-nucleon interaction cross section is also large. The pion interactions in ^{16}O nuclei considered in our simulation are : inelastic scattering, charge exchange, and absorption. First, the initial pion production point in the nucleus, where neutrino-nucleon interactions occur, is determined by the Wood-Saxon density distribution [153] :

$$\rho(r) = \frac{Z}{A}\rho_0 \frac{1}{1+\exp(\frac{r-c}{a})} \qquad (4.25)$$

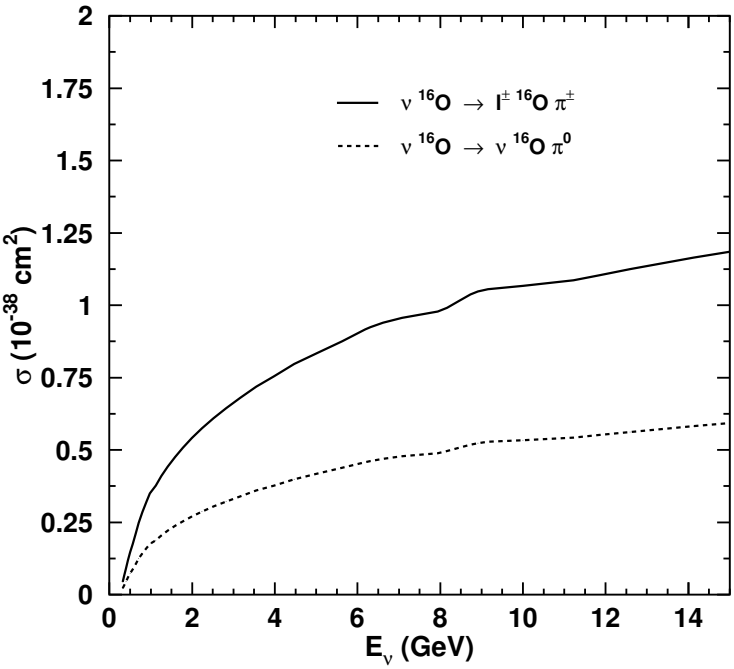

Figure 4.10: The coherent pion production cross section calculated by our Monte Carlo simulation, NEUT. The CC (NC) interactions are shown by the solid (dashed) line.

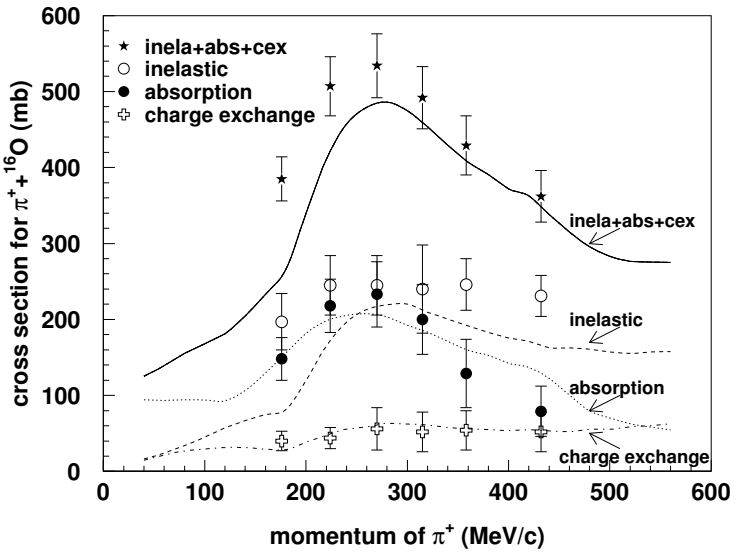

Figure 4.11: The cross section of π^+-^{16}O scattering as a function of π^+ momentum. The lines are the cross section calculated by our simulation for each interaction mode, and the experimental data points are taking from Ref. [157].

where ρ_0 is the average density of the nucleus, a and c are the density parameters, Z is the atomic number, and A is the mass number. For ^{16}O nucleus : $\rho_0 = 0.48\, m_\pi^3$, $a = 0.41$ fm, $c = 2.69$ fm, $Z = 8$ and $A = 16$. The pion interaction is determined from the calculated mean-free path of each interactions, which is modeled by L. Salcedo *et al.* [154]. The mean-free path of pions depends on their momenta and positions in the nucleus. In the interactions, the Fermi motion of the nucleus and the Pauli blocking are considered, and the outgoing nucleon must have the energy above the Fermi surface momentum defined by :

$$p_F(r) = \left(\frac{3}{2}\pi^2\rho(r)\right)^{\frac{1}{3}}. \tag{4.26}$$

The angular and momentum distributions of the outgoing pions are determined by using the results of a phase shift analysis from π - N scattering experiments [155]. The pion interaction simulation is tested using the experimental data for the following three interactions : π - ^{12}C scattering, π - ^{16}O scattering, and pion photo-production ($\gamma + ^{12}\mathrm{C} \rightarrow \pi^- + X$) [156, 157] as shown in Figure 4.11.

For kaons, the elastic scattering and charge exchange interactions are considered using the results from the cross section measured by the $K^\pm$-N scatter-

ing experiments [158, 159, 160]. For η mesons, the absorption ($\eta N \to N^* \to \pi(\pi)N$) is considered [161]. These pions are tracked as described above.

In our simulation, the nucleon re-scattering inside the oxygen nucleus is also considered using the cascade model, which is similar to that for the pion simulation. With the cross sections obtained from nucleon-nucleon scattering experiments [162], the interactions of elastic scattering and a single or two delta production process for nucleon traveling through the ^{16}O nucleus are simulated in NEUT [163]. The pions from delta decay are traced by the method described above.

4.3 Detector Simulation (Particle Tracking)

Once particles are produced using the NEUT program, they are fed into the Super-Kamiokande detector simulation program, which simulates the propagation of particles as well as the secondary interactions of the particles with water, the generation and propagation of Cherenkov photons, the PMT response, and the ADCs and the TDCs of the Super-K electronics.

The detector simulation has been developed by using GEANT package [164], which is a toolkit for the simulation of the passage of particles through matter. The processes during the propagation of particles through the detector considered in the simulation are listed in Table 4.1. The hadronic interactions in water are simulated using CALOR [165]. For the pions with $p_\pi \leq 500\,\mathrm{MeV/c}$, a custom program [166] based on the experimental results of π-^{16}O scattering [167] and π-p scattering [168] is used and treats elastic and inelastic scattering, charge exchange, and absorption processes. The number of Cherenkov photons at each wavelength is determined by Equation 2.2. Although Cherenkov photons are generated during the propagation of charged particles using GEANT, those Cherenkov photons are transmitted through water by a custom program, which include the Rayleigh scattering, the Mie scattering, and the absorption as shown in Figure 3.11. The attenuation coefficients for each of these processes is tuned by the calibrations as described in Section 3.2.1.

The reflection and absorption on black sheets are simulated using the measured probability function depending on the incident angle of Cherenkov photons. The reflection of photons off the PMT surface is also modeled using the measured probability.

For the PMT response in the detection of photons, the quantum efficiency of the PMT shown in Figure 2.8 is considered. Then, the charge output for each PMT is calculated according to the measured single p.e. distribution

Table 4.1: List of the processes considered in our detector simulation.

Particle	Process in the simulation
γ	(e^+, e^-) pair production
	Compton scattering
	Photoelectric effect
$e^{\pm}$	Multiple scattering
	Ionization and δ-rays production
	Bremsstrahlung
	Annihilation of positron
	Generation of Cherenkov radiation
$\mu^{\pm}$	Decay in flight
	Multiple scattering
	Ionization and δ-rays production
	Bremsstrahlung
	Direct (e^+, e^-) pair production
	Nuclear interaction
	Generation of Cherenkov radiation
Hadrons	Decay in flight
	Multiple scattering
	Ionization and δ-rays production
	Hadronic interactions
	Generation of Cherenkov radiation

shown in Figure 3.5. The timing of each hit PMT is simulated by smearing with the measured timing resolution as a function of detected p.e's as shown in Figure 3.8. The dark noise of the PMTs is also simulated according to the measured dark noise rate. For the electronics, all of the specifications such as triggers are considered. In order to simulate the detector precisely, the number of dead PMTs and the relative water transparency are used by the detector simulation.

The simulated MC "data" are also written in the same ZBS format as the real data as explained in Section 2.6.5 so that the data reduction and the event reconstruction processes can be run on both data and MC sets.

4.4 Tau Neutrinos Simulation

In our tau neutrino (ν_τ) interaction MC, the same program, NEUT (see section4.1), is used, and only charged current ν_τ interaction is simulated. Figure 4.12 shows the cross sections for CC ν_τ and $\overline{\nu}_\tau$ interactions. Since the cross sections of ν_τ and $\overline{\nu}_\tau$ are not well known, this leads to a large systematic uncertainty, which will be discusses in Chapter 7. CC ν_τ interactions are mostly deep-inelastic scattering due to the high energy threshold ($\sim$3.5 GeV) for tau lepton production because the mass of tau lepton is $\sim$ 1.78 GeV. Figure 4.13 shows the comparison of the cross sections for ν_τ ($\overline{\nu}_\tau$) and ν_μ, ν_e ($\overline{\nu}_\mu$, $\overline{\nu}_e$).

The tau leptons have a short lifetime of 290 femtoseconds and decay immediately into many different final states. The primary decay modes of tau leptons simulated in tau neutrino MC are summarized in Table 4.2. The decays of tau leptons are simulated by the tau lepton decay library, TAUOLA (Version 2.6) [170]. The polarization of tau leptons produced via CC ν_τ interactions is also implemented from calculations by Hagiwara *et al.* [171].

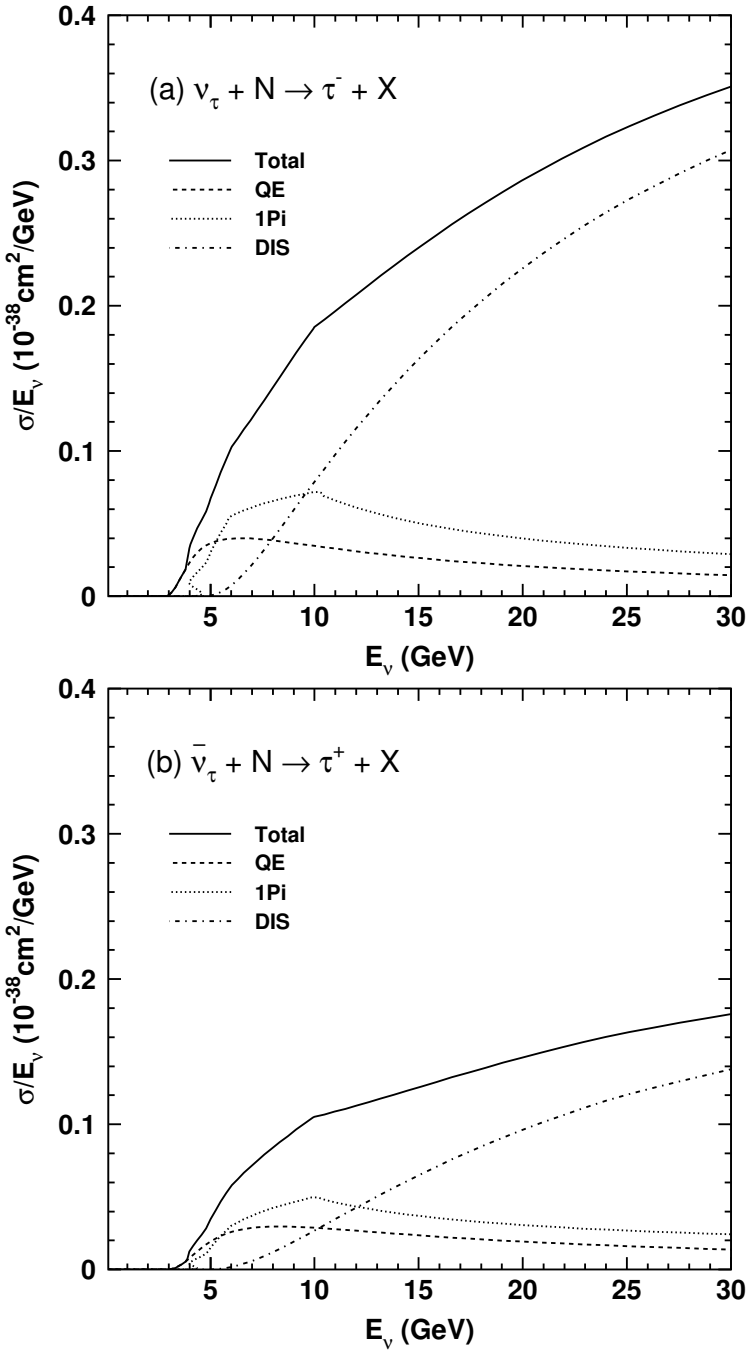

Figure 4.12: The cross sections of charged current interactions for (a) ν_τ and (b) $\overline{\nu}_\tau$ calculated by NEUT. The solid line shows the calculated total cross section. The dashed, dotted, and dash-dotted lines show quasi-elastic scattering, resonant single-meson productions, and deep inelastic scattering, respectively.

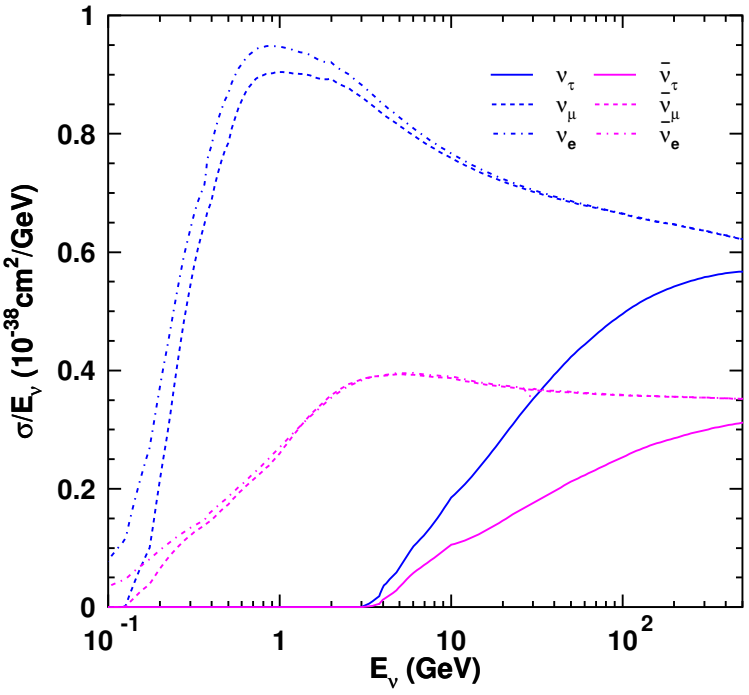

Figure 4.13: The total cross sections of CC interactions for ν_τ, ν_μ, ν_e (blue) and $\overline{\nu}_\tau$, $\overline{\nu}_\mu$, $\overline{\nu}_e$ (pink) interactions calculated by NEUT. The solid line shows ν_τ ($\overline{\nu}_\tau$) cross section, and he dashed and dash-dotted lines show ν_μ ($\overline{\nu}_\mu$) and ν_e ($\overline{\nu}_e$) cross sections.

Table 4.2: Summary for primary decay modes of tau leptons simulated in tau neutrino MC.

Decay channel	Branching Ratio
Leptonic Decay:	
$\tau^- \rightarrow e^- \overline{\nu}_e \nu_\tau$	17.81 %
$\tau^- \rightarrow \mu^- \overline{\nu}_\mu \nu_\tau$	17.37 %
Hadronic Decay:	
$\tau^- \rightarrow \nu_\tau \pi^-$	11.08 %
$\tau^- \rightarrow \nu_\tau \pi^0 \pi^-$	25.84 %
$\tau^- \rightarrow \nu_\tau \pi^0 \pi^0 \pi^-$	9.25 %
$\tau^- \rightarrow \nu_\tau \pi^+ \pi^- \pi^-$	9.00 %
$\tau^- \rightarrow \nu_\tau K^-$	0.71 %
$\tau^- \rightarrow \nu_\tau K^{*-}$	1.29 %
$\tau^- \rightarrow \nu_\tau \pi^- \pi^- \pi^+ \pi^0$	4.35 %
$\tau^- \rightarrow \nu_\tau \pi^- \pi^0 \pi^0 \pi^0$	1.11 %

Chapter 5

Data Reduction

The Super-Kamiokande detector collects about 10^6 events per day (except for the super low energy trigger events), and most of the events are cosmic ray muons and low energy background from radioactivities such as radon decay. Among these events, only the atmospheric neutrino events are selected by the data reduction processes. For this analysis, all of the reduction processes are essentially automated and are the same for SK-I and SK-II except for some of the event selection criteria because of the difference in the number of the ID PMTs.

5.1 Event Class

The atmospheric neutrino events observed in the Super-Kamiokande detector are classified into four event classes : fully contained (FC), partially contained (PC), upward stopping muon, and upward through-going muon as shown in Figure 5.1.

For FC events, the vertices of neutrino interactions are required to be within a fiducial volume, 2 m from the ID PMT surface, and all of the energy (i.e. Cherenkov photons emitted by charged particles) is deposited in the ID region. For PC events, the vertices are inside the fiducial volume of the ID and at least one particle exits the ID, depositing energy in the OD region. The parent neutrinos of the PC events are almost always muon neutrinos. The upward-going muons are produced by the atmospheric muon neutrinos via charged-current interactions in the rock surrounding the Super-K detector. Since the downward-going neutrino-induced muons cannot be distinguished from the cosmic ray muons, only muons traveling in the upward-going direction are selected. The upward stopping muons enter from outside the detector and stop inside the ID, while the upward through-going muons enter the detector

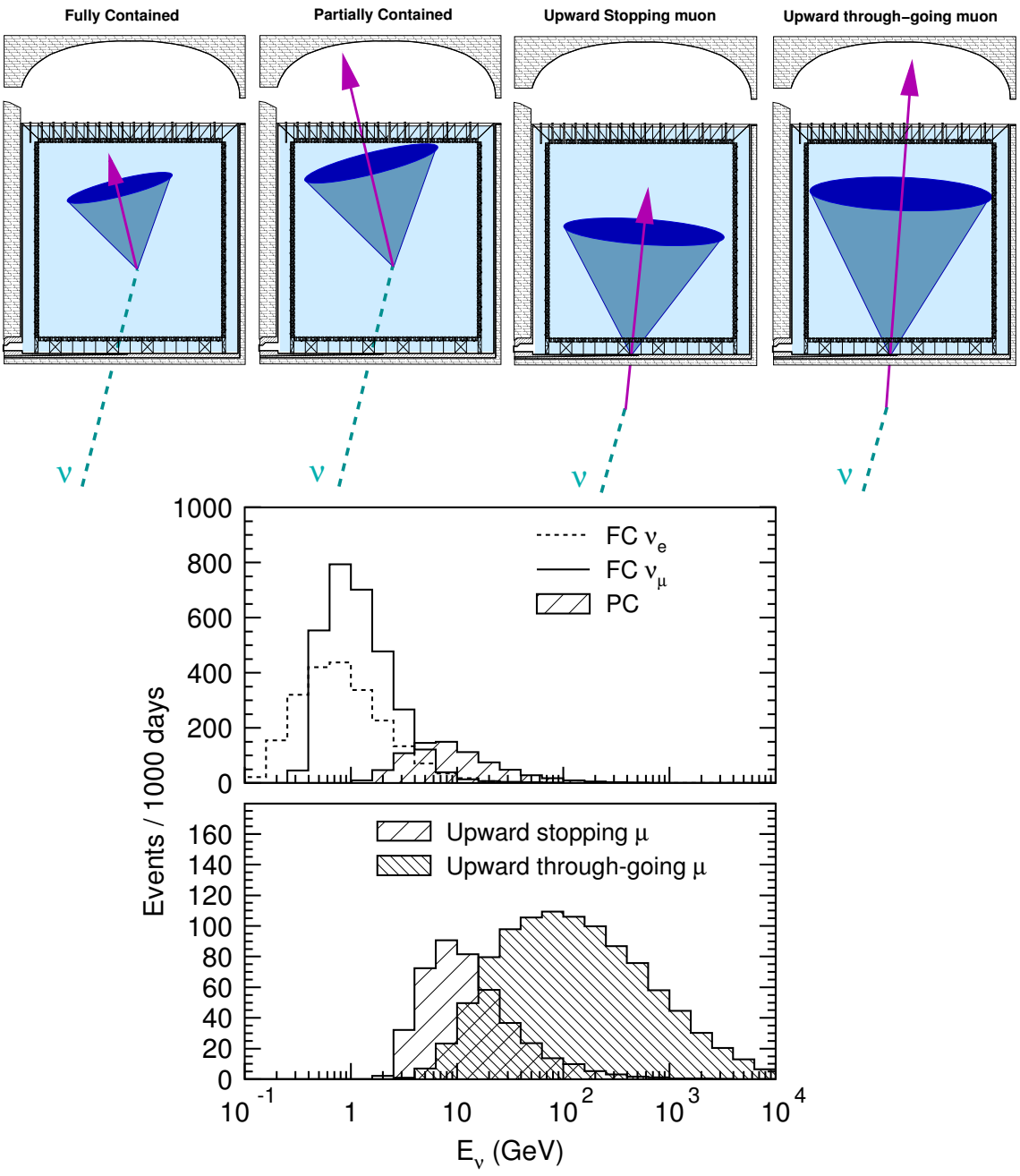

Figure 5.1: The top figure shows the atmospheric neutrino event classes in Super-Kamiokande: fully contained (FC), partially contained (PC), upward stopping muon, and upward through-going muon events. The bottom figure shows the expected parent neutrino energy distributions for each event class.

and exit the ID. The neutrino energy range for each event class are : $\sim$1 GeV for FC, $\sim$10 GeV for PC, $\sim$10 GeV for upward stopping muons, and $\sim$100 GeV for upward through-going muons. Figure 5.1 shows the expected number of neutrino events in each event category as a function of neutrino energy. The atmospheric neutrino events observed in Super-K span five decades in neutrino energy.

Besides atmospheric neutrino events, there are cosmic ray muons as the largest background to the atmospheric neutrino events, which go through the OD and enter the ID. Other backgrounds are electronic background events, so-called "flasher" events, an electric discharge in a PMT that randomly emits light due to a problem with the dynode structure, and low energy background events from radioisotopes such as ^{222}Rn.

A data sample for each event class goes through a different data reduction process. Since only the FC event sample is used for the analysis in this thesis, the data reductions for PC and upward-going muons events are not described here. A detailed description of the data reduction process for PC and upward-going muons can be found elsewhere [46, 47].

5.2 Reduction for Fully Contained Sample

The reduction process for fully contained event sample is performed in five steps as shown in Figure 5.2. The primary background, cosmic ray muons, can be removed very efficiently using the OD. The number of events are reduced from 10^6 events/day to 8 events/day. All of five steps are fully automated. The data reduction criteria for SK-II, which differ from SK-I are indicated in parentheses.

5.2.1 First Reduction

The FC first reduction is a set of simple and efficient selection criteria to quickly reduce the data to a manageable size. The criteria are :

- $PE_{300} \geq 200$ p.e. (SK-II: 100 p.e.)
  The maximum number of the total charge observed by the ID PMTs in a sliding 300 ns time window (PE_{300}) must be greater than or equal to 200 p.e's, which corresponds to the visible energy of 23 MeV (or the electron momentum of 22 MeV/c). This cuts the low energy background events from radioisotopes.

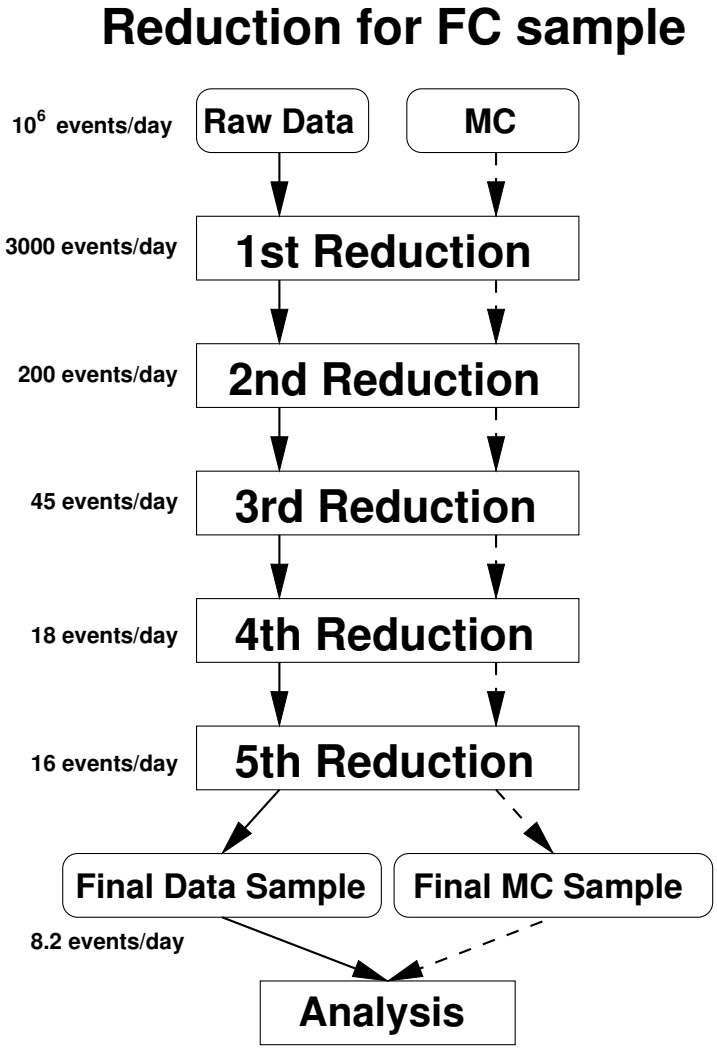

Figure 5.2: Fully contained (FC) data reduction process. About 8 atmospheric neutrino FC events/day are selected out of 10^6 events in raw data after all of the reduction processes.

- $\mathrm{NHITA}_{800} \leq 50$
  The number of the hit OD PMTs in a fixed 800 ns time window from -400 ns to $+400$ ns from the trigger timing (NHIT_{800}) must be less than or equal to 50. This removes a large amount of the cosmic ray muon events because of the activity in the OD.

- TDIFF $> 100\,\mu$s
  The time interval from the preceding event (TDIFF) should be greater than $100\,\mu$s. This rejects the decay electrons from cosmic ray muons.

At the end of the first reduction, the events within $30\,\mu$s after the FC event candidates are saved as "sub" events to later examine if there is a decay electron from muons produced in neutrino interactions.

The event rate from 10^6 events/day to 3000 events/day by the FC first reduction.

5.2.2 Second Reduction

The FC second reduction is aim to further reject the low energy events and cosmic ray muons by applying the tighter cuts :

- $\mathrm{NHITA}_{800} \leq 25$ if the total number of p.e's detected in the ID ($\mathrm{PE}_{\mathrm{tot}}$) $< 100{,}000$ p.e. (SK-II: 50,000 p.e.)
  This further cuts the cosmic ray muon background.

- $\mathrm{PE}_{\mathrm{max}}/\mathrm{PE}_{300} < 0.5$
  The ratio of the maximum number of p.e's detected by any single ID PMT ($\mathrm{PE}_{\mathrm{max}}$) to PE_{300} must be less than 0.5. This removes low energy events and some of electronic background flasher events, in which the flashing PMT records a large amount of charge. More rigorous criteria for flasher events are applied in next reduction steps.

After the FC second reduction, the event rate is down to 200 events/day.

5.2.3 Third Reduction

The third reduction is to remove cosmic ray muon events with little activity in the OD, flasher events, accidental coincidences of low energy and cosmic ray muon events. Also, further low energy events from electronics noise and radioactivities are eliminated.

Through-going muons

The through-going muons are very energetic and deposit a lot of charge in the ID. To eliminate these events, a special through-going muon fitter is applied if the number of p.e's in any single PMT is larger than 230 p.e's. This fitter selects the entrance point, which is the point of the earliest hit PMT with some neighboring hit PMTs and the exit point, which is defined the center of the saturated ID PMTs. Then, if the goodness of the fit is greater than 0.75, and the number of hit OD PMTs are more than 9, the events are found to be through-going muons. The rejection criteria are :

- $\mathrm{PE_{max}} > 230\,\mathrm{p.e.}$
- Goodness of through-going muon fit > 0.75
- $\mathrm{NHITA_{ent}} \geq 10$ or $\mathrm{NHITA_{exit}} \geq 10$
  The number of hit OD PMTs within 8 m from the defined entrance or exit point in a fixed 800 ns time window is greater than or equal to 10.

Stopping muons

To eliminate stopping muons, a stopping muon fitter is applied, which finds the entrance point in the same way as through-going muon fit. The events satisfying the following criteria are classified as stopping muons and removed :

- $\mathrm{NHITA_{ent}} \geq 10$

or

- $\mathrm{NHITA_{ent}} \geq 5$ (SK-II: 10) if the goodness of stopping muon fit > 0.5

Cable hole muons

Some of cosmic ray muons pass though the cable holes, where the cables for PMTs are bundled and sent up to the top of the tank. Four holes out of twelve are directly above the ID and block the OD. Cosmic ray muon going through these hole would not leave any OD activity and could be detected as neutrino events. To remove this mis-identification possibility, a set of veto counters (2 m $\times$ 2.5 m plastic scintillation counters) were installed in April, 1997. The rejection criteria for cable hole muons are :

- One veto counter hit

- The distance between the cable hole to the reconstructed vertex is less than 4 m.

Flasher events

Flasher events usually have broad timing distribution while the neutrino events (and cosmic ray muon events) have relatively sharp timing profile. The flasher events are removed by looking at the number of hit ID PMTs in a sliding 100 ns time window ($NHIT_{100}$) from +300 ns to +800 ns. The rejection criteria are :

- $NHIT_{100} \geq 15$

or

- $NHIT_{100} \geq 10$ if the number of hit ID PMTs is less than 800.

For SK-II :

- $NHIT_{100} \geq 20$

Accidental coincidences

The accidental coincidence occurs when a low energy event starts the trigger and a cosmic ray muon event follows, which deposit the charge in the ID without the triggered OD activities. These events can be removed by the number of hit OD PMTs ($NHIT_{acci}$) and p.e's (PE_{acci}) in a fixed 500 ns time window from from +400 ns to +900 ns of the trigger time. The rejection criteria are :

- $NHIT_{acci} \geq 20$

and

- $PE_{acci} > 5000$ p.e. (SK-II: 2500 p.e.)

Low energy events

The remaining low energy events from the decay of radioisotopes and the electrical noise are eliminated by looking at the number of hit ID PMTs in a sliding 50 ns time window ($NHIT_{50}$), and the criterion is :

- $NHIT_{50} < 50$ (SK-II: 25)
  $NHIT_{50} = 50$ corresponds to a visible energy of 9 MeV.

After the FC third reduction, the event rate is 45 events/day.

5.2.4 Fourth Reduction

Fourth reduction is dedicated to further remove flasher events. Flasher events usually repeat with similar hit patterns in the detector in the course of hours and days. These repeated events are not likely to be caused by neutrinos. The algorithm is developed to look for any similar charge pattern and is applied to 10,000 events before and after the flasher event candidate.

The event rate after the FC 4th reduction is 18 events/day.

5.2.5 Fifth Reduction

In the last reduction stage, all of the cuts are specialized for each kind of background events.

Stopping muons

The remaining stopping muons are removed if the number of hit OD PMTs within 8 m of the entrance point in a sliding 200 ns time window from 400 ns before and after the event trigger is greater than or equal to 5. For SK-II, no stopping muon cut is applied.

Invisible muons

Invisible muon events are caused by cosmic ray muons with momenta less than the Cherenkov threshold and subsequent decay electrons, which emit Cherenkov light.

- $PE_{tot} < 1{,}000$ p.e. (SK-II: 500 p.e.)
  The total number of the p.e. detected by the ID is less than 1000 p.e.
- $NHITAC_{off} > 4$
  The maximum number of hit OD PMTs in the cluster in a sliding 200 ns time window from $-8{,}900$ ns to -100 ns.
- $NHITAC_{off} + NHITAC_{500} > 9$ if the distance between two hit OD clusters is less than 500 cm.
  or
  $NHITAC_{off} > 9$
  $NHITAC_{500}$ is the number of hit OD PMTs in the cluster in a fixed 500 ns time window from -100 ns to $+400$ ns.

Coincidence muons

The remaining coincidence muon events are removed by :

- $PE_{500} < 300$ p.e. (SK-II: 150 p.e.)
  The total number of the p.e. detected by the ID in a fixed 500 ns time window from -100 ns to $+400$ ns is less than 300 p.e.

- $NHITA_{200} \geq 20$
  The maximum number of the hit OD PMTs in a 200 ns sliding time window from +1,300 ns to +2,500 ns is greater than or equal to 20.

Long-tail flasher events

- Goodness of point fit < 0.4

and

- $NHITMIN_{100} > 5$
  The maximum number of the hit ID PMTs in a 100 ns sliding time window from +300 ns to +800 ns is greater than 5.

For SK-II, in addition to the criteria above, the extra cuts are applied :

- Goodness of point fit < 0.3

and

- $NHITMIN_{100} < 6$

We have 16 events/day after the FC 5th reduction.

5.2.6 Fully Contained Cut

Finally, the fully contained neutrino events are selected by applying the FC event cuts :

- Vertex of neutrino interactions must be inside the fiducial volume (2 m from the ID PMT surface).

- The number of hit PMTs in the highest charge OD cluster (NHITAC) must be less than or equal to 9 (SK-II: 15).

- Visible energy (E_{vis}) should be greater than 30 MeV.

The rate of FC neutrino events are 8.2 events/day for SK-I and SK-II. Table 5.1 shows the number of events for data and MC after each FC reduction process and the FC event cuts.

Table 5.1: Number of events for data and MC (efficiency) after each FC reduction process and FC event cuts for SK-I.

Reduction step	Data	Monte Carlo
Trigger	1,889,599,293	14013.9 (100.00 %)
First reduction	4,591,659	14006.3 (99.95 %)
Second reduction	301,791	14006.1 (99.94 %)
Third reduction	66,810	13993.3 (99.85 %)
Fourth reduction	26,937	13898.1 (99.17 %)
Fifth reduction	23,984	13895.3 (99.15 %)
FC event cuts	12,180	13676.7 (97.59 %)

Chapter 6

Event Reconstruction

The atmospheric neutrino data and MC samples go through the event reconstruction procedure to determine the event properties such as vertex positions, momenta, number of Cherenkov rings, and particle identification. After the events are reconstructed, the FC events are categorized into :

- Based on the Number of rings:
  Single-ring events: number of Cherenkov rings = 1
  Multi-ring events: number of Cherenkov rings > 1
- Based on Particle Identification:
  e-like events: showering events ($e^{\pm}, \gamma$)
  μ-like events: non-showering events ($\mu^{\pm}, \pi^{\pm}$)
- Based on Visible energy:
  Sub-GeV events: $E_{vis} \leq 1.33$ GeV
  Multi-GeV events: $E_{vis} > 1.33$ GeV

All of the processes are automated.

6.1 Vertex Fitting

The event reconstruction process starts from the vertex fitting. The vertex position is reconstructed using the timing information of each hit PMTs in three steps. First, assuming the Cherenkov light is emitted from a point-like source, a rough vertex position is found by minimizing the timing residual distribution. The timing residual is the arrival time of Cherenkov photons subtracted by the time-of-flight (TOF). The goodness of the fit, G_p is defined and maximized :

$$G_p = \frac{1}{N}\sum_i \exp\left(-\frac{(t_i - t_0)^2}{2\,(1.5\times\sigma)^2}\right) \tag{6.1}$$

where N is the number of hit PMTs, t_i is the time residual of the i-th PMT, t_0 is the mean time residual, and σ is the timing resolution of the PMTs (2.5 ns). Once the vertex is determined, a rough particle direction is estimated by summing up the charge-weighted vector from the vertex to each hit PMT. Second, the outer edge of the most energetic Cherenkov ring is estimated by calculating the observed charge as a function of the Cherenkov opening angle from the particle direction. By changing the direction, the sharpest ring is found. In the final step, instead of assuming a point-like source, the track length of the charged particle and the scattered Cherenkov photons are considered by modifying the goodness with the the light inside and outside of the Cherenkov rings, which account for the track length and the scattered photons, respectively. For the single-ring events, the vertex is more precisely fitted by the algorithm described in Section 6.4.

6.2 Ring Counting

Once the event vertex and the first Cherenkov ring is found, a ring counting algorithm is applied to search for any other Cherenkov ring in the event. In the data sample used in this thesis, the neutrino energy is high enough to produce multiple particles such as pions, which can emit Cherenkov light and thus multiple Cherenkov rings are created.

Cherenkov ring candidates are searched by an algorithm using a Hough transformation [173]. The basic idea of the algorithm is illustrated in Figure 6.1. Basically, the center of a possible ring can be identified by putting a ring around the hit PMT with Cherenkov opening angle of 42 ° from the event vertex. In the algorithm, this is done by mapping the charge distribution on a (Θ, Φ) plane for each hit PMT as shown in Figure 6.2. The peaks are the directions of the identified Cherenkov rings.

After ring candidates are found, they are tested using six evaluation functions to determine if they are true rings. The evaluation functions are :

- L_1 : The probability that the observed charge distribution (p.e's) would match the expected p.e's with or without a candidate ring.
- L_2 : The charge density at the peak of the candidate rings.

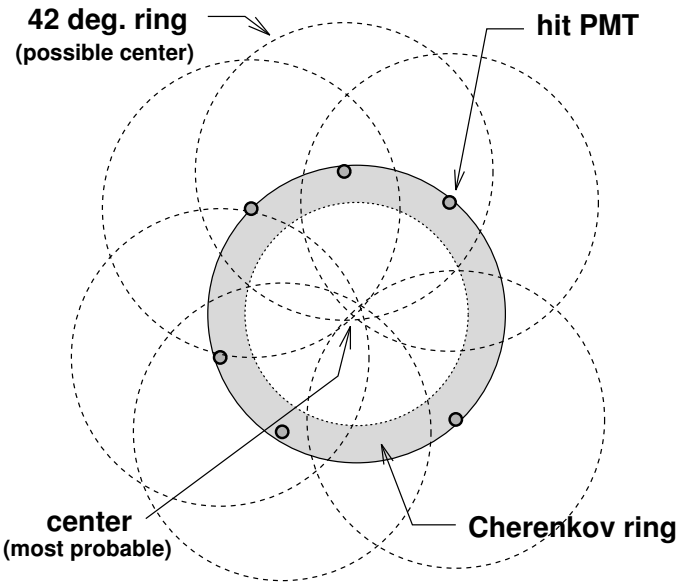

Figure 6.1: A basic idea of finding ring candidates is shown. By drawing rings around the hit PMT with Cherenkov opening angle of 42° from the vertex, the center of the actual Cherenkov ring can be identified.

L_3 : The difference in p.e's between the peak of a candidate ring and the outside of the peak. The larger L_3 is, the more likely the candidate is to be a true ring.

L_4 : The difference in p.e's between the peak of a candidate ring and the average of inside and outside the ring. The larger L_4 is, the more probable the candidate is to be a true ring.

L_5 : The residual p.e's, which is a vector sum of the charge over all PMTs, between the observed p.e's and the expected p.e's of the rings already found.

L_6 : The azimuthal symmetry of a ring with respect to the direction of the ring. A single-ring event is more symmetric than a multi-ring event.

For SK-I, the likelihood is a linear combination of six evaluation functions with optimized weights (α_i) :

$$\mathcal{L}_{\mathrm{SK-I}} = \sum_{i=1}^{6} [\alpha_i L_i] \tag{6.2}$$

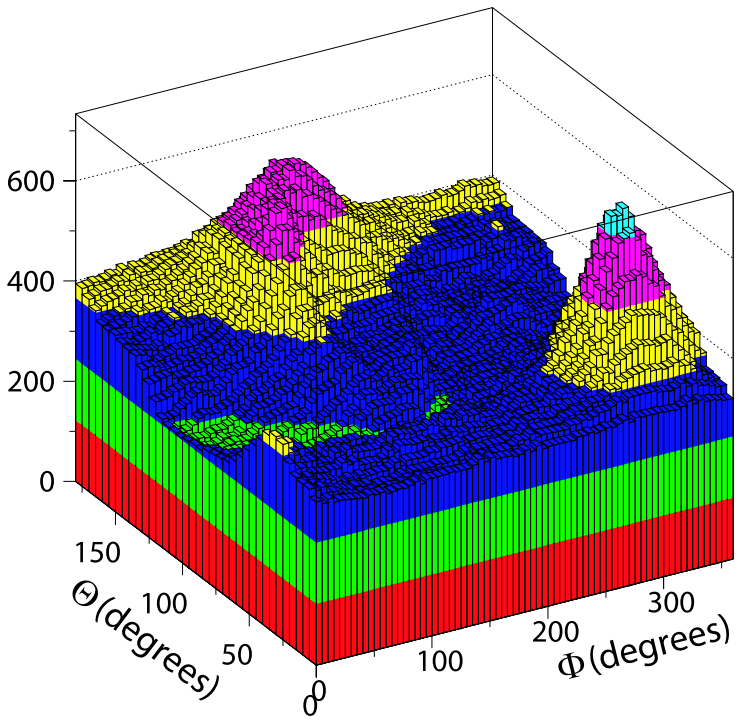

Figure 6.2: A charge map from Hough transformation algorithm for a typical two ring events. The peaks are the direction of the Cherenkov rings.

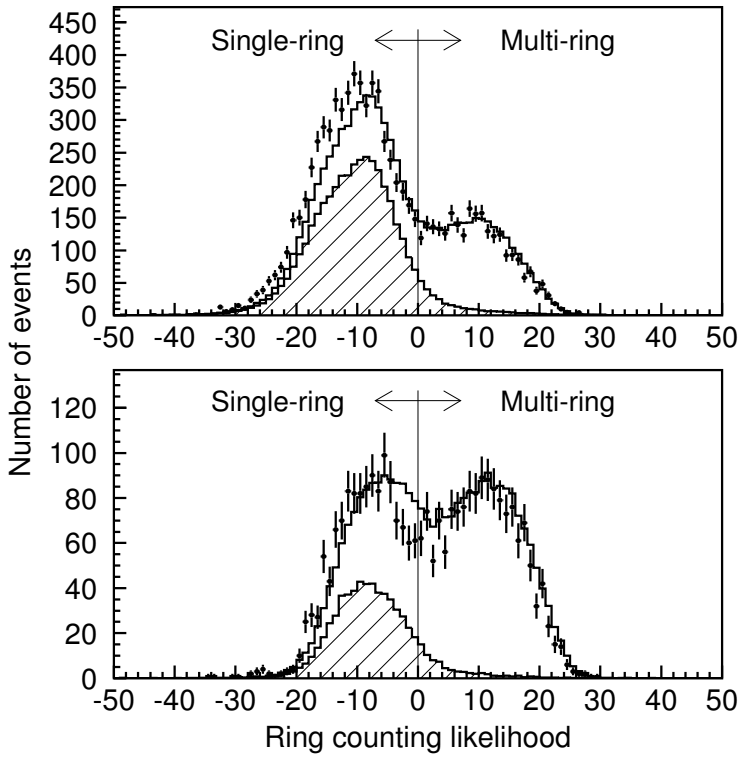

Figure 6.3: The ring-counting likelihood distributions of for Sub-GeV events (top) and Multi-GeV events (bottom). The points are SK data and the histograms are atmospheric neutrino MC events considering the neutrino oscillations with SK-I best-fit oscillation parameters ($\sin^2 2\theta$, Δm^2) = (1.00, 2.1 $\times$ 10^{-3} eV^2). The hatched histograms show the CC QE interactions.

For SK-II, the ring counting is modified to use a true log likelihood method. Using MC samples of single-ring and multi-ring events, the probability density functions (PDFs) for each evaluation function are determined, and the likelihood is calculated as :

$$\mathcal{L}_{\mathrm{SK-II}} = \sum_{i}^{6} log\left[(\mathcal{P}_i)\right] \tag{6.3}$$

$$= \sum_{i}^{6} \{log\left[(\mathcal{P}_i)_{multi}\right] - log\left[(\mathcal{P}_i)_{single}\right]\} \tag{6.4}$$

where $\mathcal{P}_i$ is the probability density function for i-th evaluation function, and $\mathcal{P}_{multi}$ and $\mathcal{P}_{single}$ are the probability for multi-ring and single-ring events.

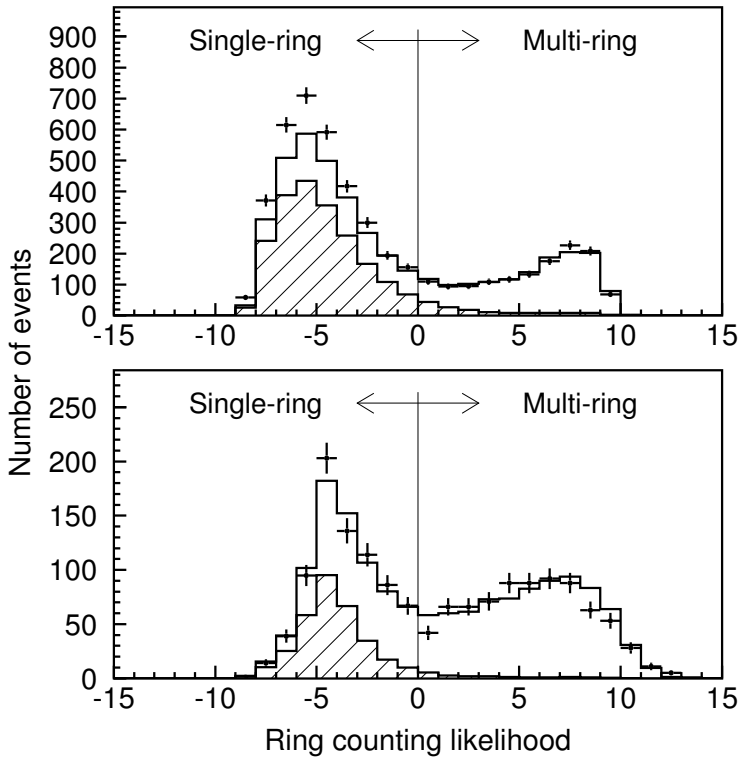

Figure 6.4: The ring-counting likelihood distributions of for Sub-GeV events (top) and Multi-GeV events (bottom) for SK-II. The points are SK data and the histograms are atmospheric neutrino MC events considering the neutrino oscillations with SK-I+SK-II best-fit oscillation parameters ($\sin^2 2\theta$, Δm^2) = (1.00, 2.5×10^{-3} eV^2). The hatched histograms show the CC QE interactions.

The ring-counting process is repeated until no other rings are found. The maximum number of rings, which can be found, is set to be five. The more details can be found in Ref. [47, 174].

6.3 Particle Identification

A particle identification (PID) program is applied to identify the final state particles. All of the Cherenkov rings are classified into two types: showering (e-like) or non-showering (μ-like). Due to the electromagnetic shower and multiple scattering, electrons or gamma-rays produce e-like rings, which give diffused (fussier) ring patterns. Non-showering (μ-like) rings are produced

by muons or charged pions and have sharper ring edges. Figure 6.5 shows the event display of electron and muon neutrino MC events as an example. Each small circle on the figure represents a hit PMT, and the size of a circle corresponds to the number of photons detected. In addition, the Cherenkov rings from electrons and gamma-rays have the Cherenkov opening angle of 42 °, but the Cherenkov rings from muons or charged pions can have smaller angles if they are not highly relativistic ($\beta = v/c \ll 1$) and when they lose energy. The PID algorithm exploits these differences in the patterns and the opening angles of the Cherenkov rings.

Using MC simulations, expected photoelectron distributions and expected opening angle of Cherenkov rings from electrons and muons are calculated for each PMT by considering different vertex positions, light attenuation length, and PMT acceptance with different energies. By comparing the observed rings with the above, the probability for the ring pattern and the opening angle, ($P^{\text{pattern}}(e \text{ or } \mu)$) and ($P^{\text{angle}}(e \text{ or } \mu)$) can be obtained. The probability functions of the PID for single-ring events and multi-ring events are defined as :

$$P_{single}(e,\mu) = P_{single}^{\text{pattern}}(e,\mu) \times P_{single}^{\text{angle}}(e,\mu) \quad \text{(Single-ring event)} \quad (6.5)$$

$$P_{multi}(e,\mu) = P_{multi}^{\text{pattern}}(e,\mu) \quad \text{(Multi-ring event)} \quad (6.6)$$

For multi-ring events, only $P_{multi}^{\text{pattern}}(e \text{ or } \mu)$ is used since the opening angle is not estimated precisely. This algorithm was tested by a beam test experiment at KEK [175]. The distributions of PID likelihood, $P_{PID} \equiv \sqrt{-\log P(\mu)} - \sqrt{-\log P(e)}$, for single-ring events and multi-ring events are shown in Figure 6.6. $P_{PID} < 0$ is e-like and $P_{PID} \geq 0$ is μ-like. Also, Figure 6.7 shows the PID likelihood distributions for SK-II.

The misidentification probabilities are estimated to be 0.8 % and 0.7 % for ν_e and ν_μ using CC quasi-elastic scattering simulation events.

6.4 Precise Vertex Fitting (MS-fit)

For single-ring events, the vertex resolution in the longitudinal directions fitted by vertex fitting algorithm described in Section 6.1 is not optimized since it only uses the timing information. This can be improved by refitting the vertex position using the ring pattern. The MS-fit modifies the vertex position and the particle direction by calculating the PID likelihood, and the vertex position is adjusted perpendicularly to the particle direction using the first vertex fitter with the timing information. This process is iterated until

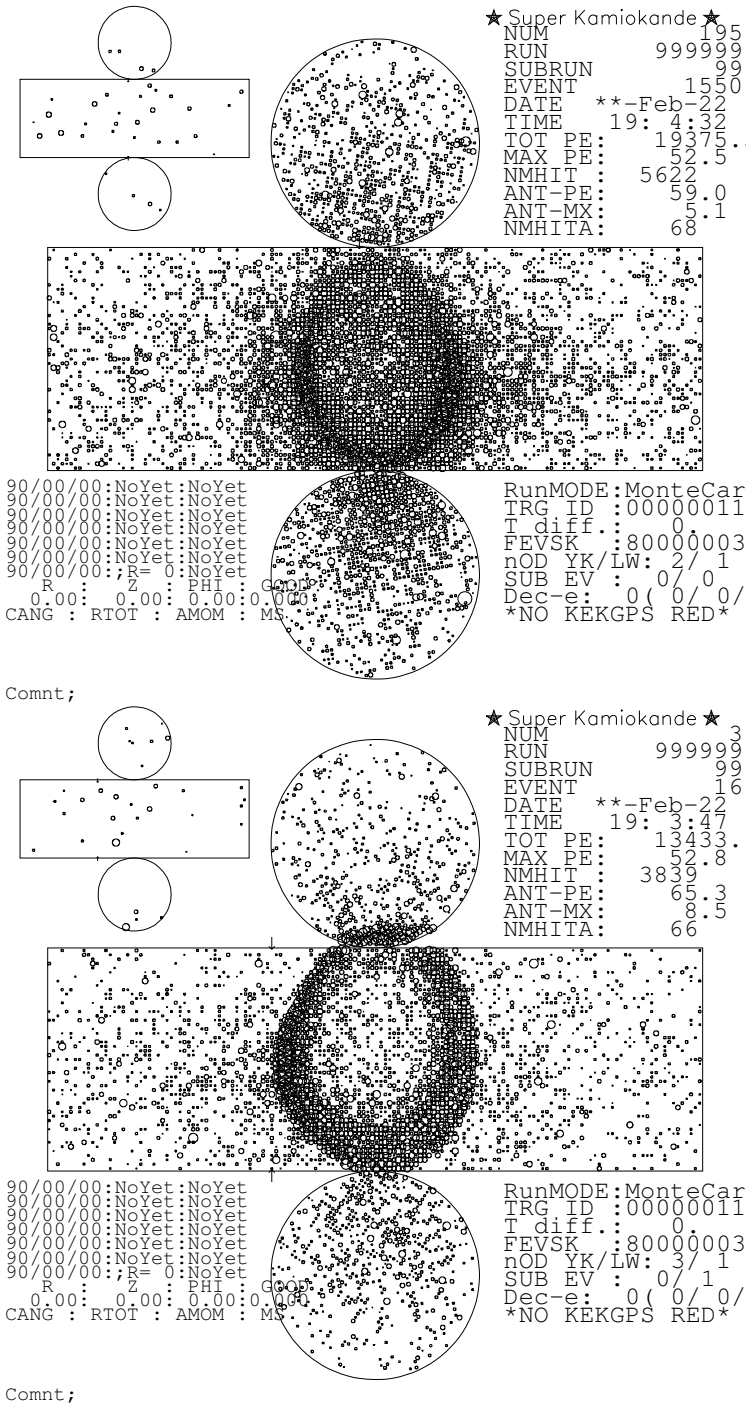

Figure 6.5: Event display of single-ring electron (top) and single-ring muon (bottom) neutrino MC event. Each small circle on the figure represents a hit ID PMT, and the size of a circle corresponds to the number of photons detected. Electron event gives diffused ring pattern, and muon event has sharp ring edges.

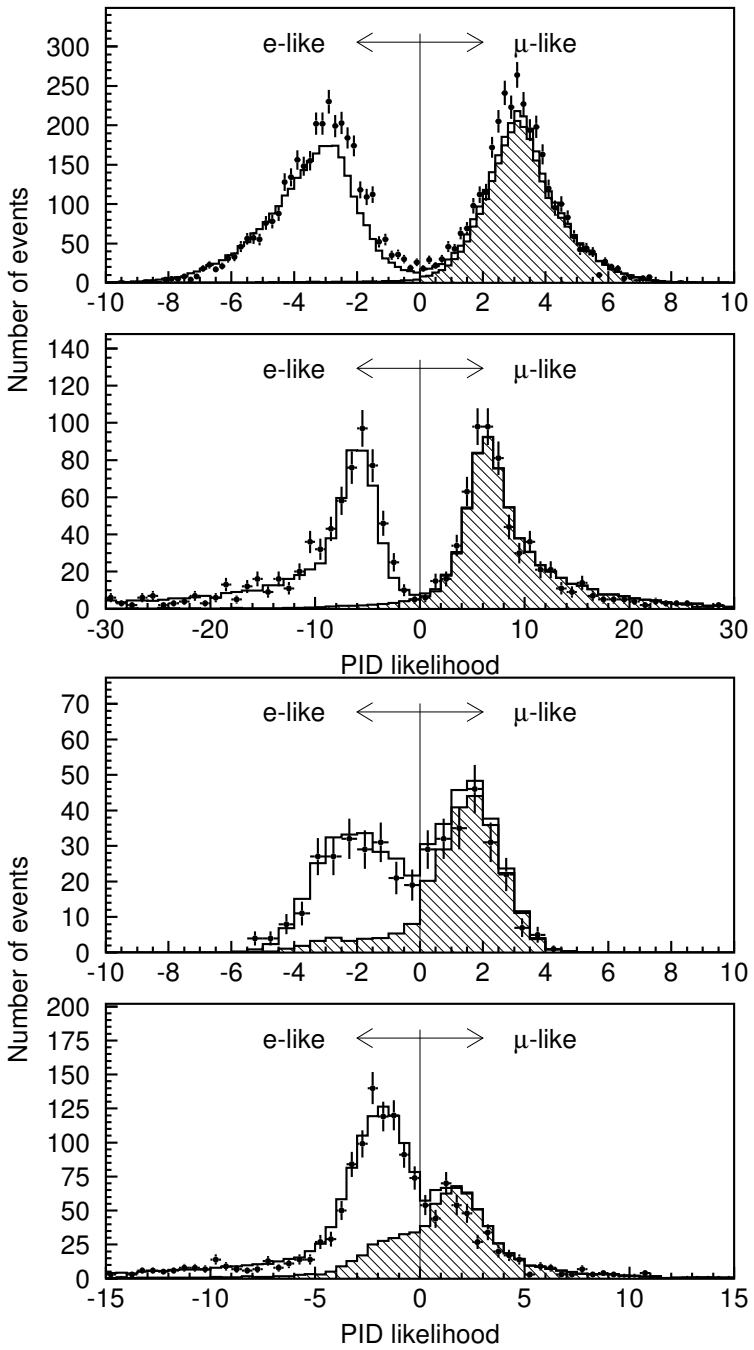

Figure 6.6: The SK-I PID likelihood distributions of Sub-GeV and Multi-GeV events for single-ring events (top) and multi-ring events (bottom). The points are SK-I data and the histograms are atmospheric neutrino MC events considering the neutrino oscillations with SK-I best-fit oscillation parameters $(\sin^2 2\theta,\ \Delta m^2) = (1.00,\ 2.1 \times 10^{-3}\ \mathrm{eV}^2)$. The hatched histograms show the ν_μ CC interactions.

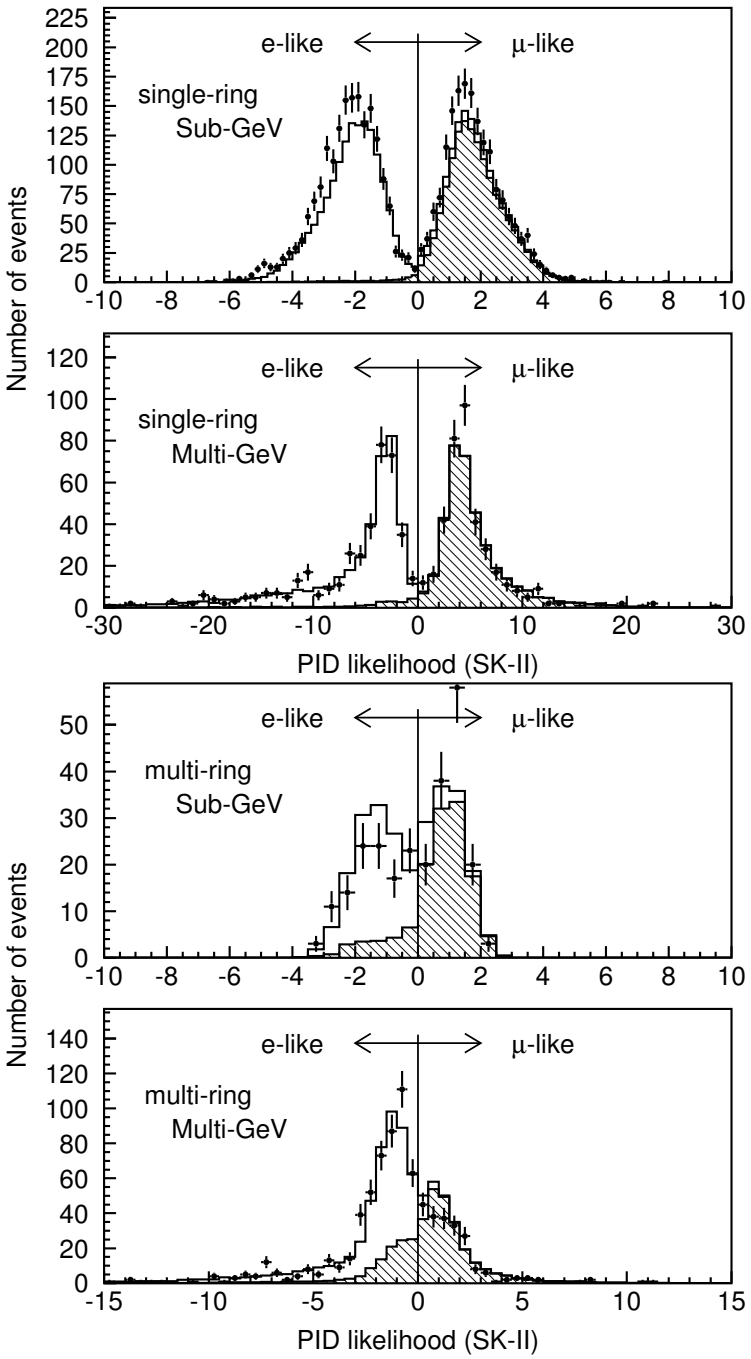

Figure 6.7: The SK-II PID likelihood distributions of Sub-GeV and Multi-GeV events for single-ring (top) and multi-ring (bottom). The points are SK-II data and the histograms are atmospheric neutrino MC events considering the neutrino oscillations with SK-I+SK-II best-fit oscillation parameters ($\sin^2 2\theta$, Δm^2) = (1.00, 2.5 $\times$ 10^{-3} eV^2). The hatched histograms show the ν_μ CC interactions.

the changes in the vertex position and the particle direction is less than 5 cm and 0.5 degrees. The vertex resolution for single-ring events is approximately 30 cm.

6.5 Momentum Reconstruction

The momentum of each particle is determined by summing up all of the p.e's inside a 70 ° half-angle cone, which is defined by the vertex position and the particle direction for each ring. The total number of p.e's for each ring is corrected by taking into account the light attenuation and the PMT acceptance. The total p.e's are calculated in the timing window from -50 ns to $+250$ ns of the events to avoid the electrons from muon decays.

6.6 Ring Correction

As the last step in the event reconstruction process, the number of rings is corrected using the energy and angle information obtained for each ring, and mis-fit rings are removed. The criteria for the correction to remove the i-th ring are :

- The momentum of i-th ring is less than another ring, j ($p_i < p_j$; i $\neq$ j), the separation, θ_{ij} between i-th and j-th rings is less than 30 degrees, and the i-th ring has the momentum less than 60 MeV perpendicular to j-th ring direction ($p_i \, cos\theta_{ij} < 60$ MeV/c).
- The momentum of i-th ring is less than 40 MeV/c and also less than 5 % of the total momentum.

In SK-I, the momentum for the ring correction is determined without using the PID information, but in SK-II, the momentum is calculated using the PID information.

Chapter 7

Tau Neutrino Appearance Analysis

As described in Chapter 1, atmospheric neutrino oscillations have been observed by Super-K and other experiments. The most favored hypothesis for these experimental observations is $\nu_\mu \leftrightarrow \nu_\tau$ oscillations. However, all results rely on the disappearance of muon neutrinos from the atmospheric neutrino flux, and there is still no explicit observation of tau neutrino appearance through their charged-current (CC) weak interactions.

This chapter describes the analysis to search for ν_τ appearance via CC interactions using the Super-K atmospheric neutrino data. The main difference between this analysis and the previous atmospheric neutrino analyses is that this analysis is conducted in the "appearance" mode (Section 1.3.1). The observation of ν_τ charged-current interactions in Super-K would also be an unambiguous confirmation for $\nu_\mu \leftrightarrow \nu_\tau$ oscillations.

7.1 Overview

The appearance of tau neutrinos in the atmospheric neutrinos has never been observed mainly because the detection of ν_τ CC interactions is challenging due to two reasons. First, the mass of tau leptons is 1.78 GeV, and thus the neutrino energy threshold for tau lepton production is approximately 3.5 GeV. The atmospheric neutrino flux above this energy is relatively low. Figure 7.1 shows the energy of the atmospheric neutrino and ν_τ CC events. Assuming two flavor maximal mixing of $\nu_\mu \leftrightarrow \nu_\tau$ with $\Delta m^2 = 2.4 \times 10^{-3}\,\mathrm{eV}^2$, approximately one ν_τ CC event is expected to occur in an atmospheric neutrino detector per kiloton-year of exposure. This corresponds to an estimated total of 78 ν_τ events in the SK-I atmospheric neutrino data (1489.2 live-days) and 43 ν_τ events in the SK-II data (803.9 live-days). Previous atmospheric neutrino experiments have observed the disappearance of ν_μ in the atmospheric neutrino

flux. This is because most of ν_μ have the energy less than 3.5 GeV and ν_τ from ν_μ oscillations do not have enough energy to produce tau leptons.

Second, the tau lepton has a short lifetime (290 femtoseconds) and decays immediately into many different final states. These final decay products consist of electrons, muons, or one or more pions (plus always a tau neutrino) as shown in Table 7.1. The recoiling hadronic system may also produce multiple particles. Water Cherenkov detectors such as Super-K are not well suited for identifying individual ν_τ CC interactions as there are generally multiple Cherenkov rings with no easily identifiable leading lepton. Unlike electrons or muons, which can be observed directly in the detector, tau leptons can only be observed by detecting their decay particles. An event display of a tau neutrino MC event is shown in Figure 7.2.

Since the expected signal to noise ratio is about 0.5 % and this analysis is background-dominated, a likelihood technique is employed to discriminate ν_τ events from atmospheric neutrino events on a statistical basis.

Table 7.1: Summary for primary decay modes of tau leptons simulated in tau neutrino MC.

Decay channel	Branching Ratio
Leptonic Decay:	
$\tau^- \rightarrow e^- \overline{\nu}_e \nu_\tau$	17.81 %
$\tau^- \rightarrow \mu^- \overline{\nu}_\mu \nu_\tau$	17.37 %
Hadronic Decay:	
$\tau^- \rightarrow \nu_\tau \pi^-$	11.08 %
$\tau^- \rightarrow \nu_\tau \pi^0 \pi^-$	25.84 %
$\tau^- \rightarrow \nu_\tau \pi^0 \pi^0 \pi^-$	9.25 %
$\tau^- \rightarrow \nu_\tau \pi^+ \pi^- \pi^-$	9.00 %
$\tau^- \rightarrow \nu_\tau K^-$	0.71 %
$\tau^- \rightarrow \nu_\tau K^{*-}$	1.29 %
$\tau^- \rightarrow \nu_\tau \pi^- \pi^- \pi^+ \pi^0$	4.35 %
$\tau^- \rightarrow \nu_\tau \pi^- \pi^0 \pi^0 \pi^0$	1.11 %

7.2 Data and MC set

In this analysis, the fully-contained Multi-GeV neutrino events of the atmospheric neutrino data accumulated during the SK-I period (from May, 1996 to July, 2001; 1489.2 live-day exposure) and the SK-II period (from January, 2003

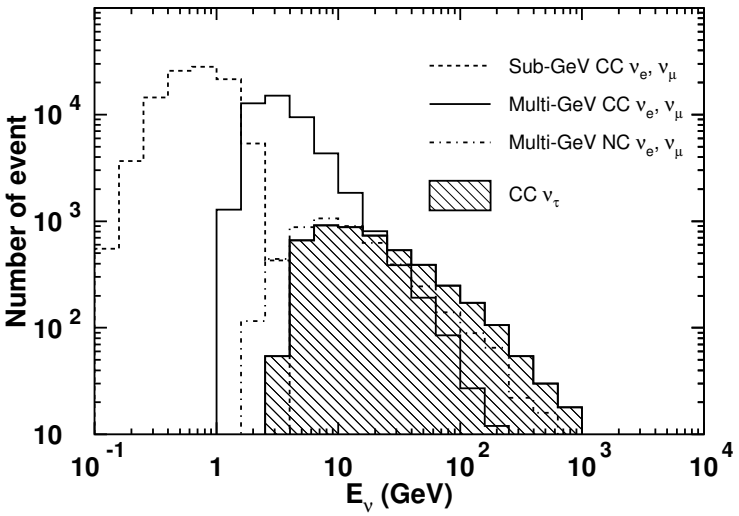

Figure 7.1: Energy spectrum of the FC Sub-GeV CC and FC Multi-GeV CC/NC atmospheric neutrino (ν_e and ν_μ) events, and CC ν_τ events.

to October, 2005; 803.9 live-day exposure) are used. The amount of Monte Carlo events generated for the atmospheric neutrinos and tau neutrinos are equivalent to an exposure of 100 years and 200 years of SK-I, and an exposure of 60 years and 200 years of SK-II, respectively. Two sets of atmospheric neutrino and tau neutrino MC events are generated; one for the likelihood function calculation and the other for the analysis as listed in Table 7.2.

The event selection criteria are :

- Fully-contained events:

  (1) The vertex is reconstructed within the 22.5 kton fiducial volume (2 m from the ID PMT surface).

  (2) Little or no activity in the OD region; # of hit PMTs in the OD hit cluster NHITAC, < 10 (16 for SK-II).

- Multi-GeV events:

  (3) Visible energy (E_{vis}) > 1.33 GeV.

First, the SK-I and SK-II data are analyzed separately, and later, an analysis is carried out to combine both SK-I and SK-II data as described in Section 7.7.

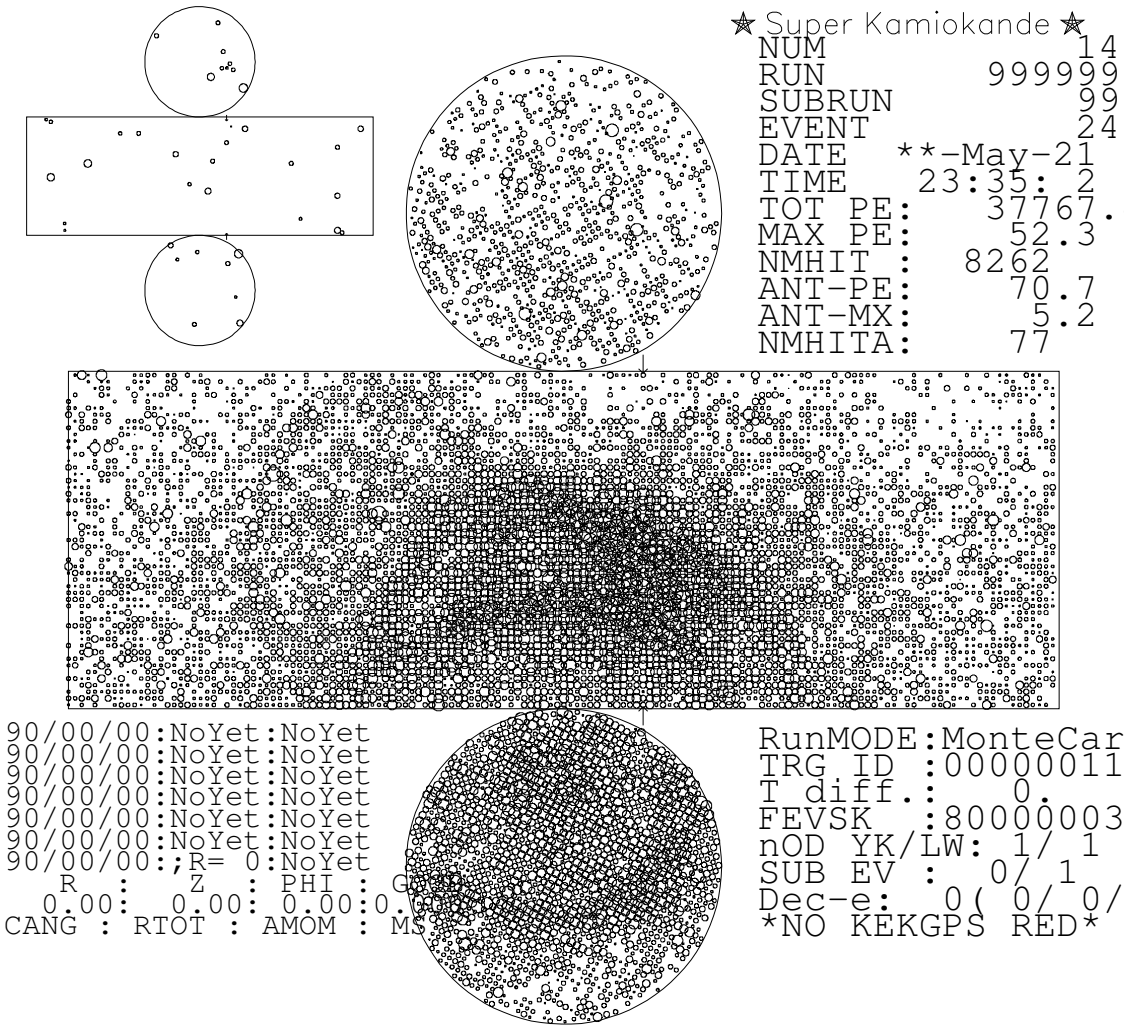

Figure 7.2: Event display of typical tau neutrino MC event. Each small circle represents a hit PMT, and its size corresponds to the number of photoelectrons detected. In this event, $\tau^- \rightarrow \nu_\tau \pi^0 \pi^-$.

Table 7.2: Data and the atmospheric neutrino (ν_e, ν_μ) and the tau neutrino MC sets for SK-I and SK-II ν_τ appearance analysis. Extra MC sets are used to construct the likelihood functions for SK-I and SK-II (See section 7.5).

	Data	$\nu_{e,\mu}$ BKG MC	ν_τ MC	Use
SK-I	-	100 yr	200 yr	Likelihood calculation
	1489.2 days	100 yr	200 yr	Analysis
SK-II	-	60 yr	200 yr	Likelihood calculation
	803.9 days	60 yr	200 yr	Analysis

7.3 Tau Neutrino Events

The ν_τ event signatures are characterized by the decays of tau leptons produced through ν_τ CC interactions. As listed in Table 7.1, the fractions of leptonic and hadronic decays of tau leptons are 35 % and 65 %, and approximately 83 % of tau lepton decays are "showering" due to electrons and hadron showers. Also, some pions are usually associated with a ν_τ event since more than 50 % of ν_τ interactions are deep-inelastic scattering. Hence, for Multi-GeV events, 95 % of ν_τ events are associated with at least one pion, and 80 % of leptonic tau lepton decays produce one or more pions. On average, six pions are produced in ν_τ events. Therefore, ν_τ events have a high multiplicity resulting primarily in hadronic shower, i.e. e-like events. However, the leptonic decays of tau leptons cannot be easily distinguished from the atmospheric neutrino CC events. Thus, the analysis in this thesis concentrates on the hadronic decays of tau leptons.

The primary backgrounds for ν_τ signals are atmospheric neutrinos (ν_e and ν_μ) producing multiple pions via CC/NC deep-inelastic scattering. [1] Tau neutrinos can be also produced in the atmosphere. However as described in Section 4.1, the number of those tau neutrinos are negligible.

Because of high multiplicity and large mass of tau leptons, the shape of events containing a tau lepton decay has a more spherical topology than that of the backgrounds. To find ν_τ events, the extra pions produced in tau lepton decays can also be tagged by looking for their decays and ring signatures in the Super-K detector. As mentioned in Chapter 1, the depletion of muon neutrinos in the atmospheric neutrino flux is observed in the upward-going direction, i.e. the zenith angle $\cos\theta < 0$. Hence tau neutrino events are

[1] In the previous disappearance analyses, the atmospheric neutrinos are studied as signals, but in the present analysis, they become backgrounds.

expected to be upward-going.

Based on the different characteristics between the signal and background events described above, the following event selection cut is applied on FC Multi-GeV events to reduce the atmospheric neutrino backgrounds :

Initial tau neutrino event selection cut :

The most energetic ring must be e-like (showering).

This initial event cut can reduce approximately 90% of the background while keeping 60% of the signals. The effects of the event selection criteria are summarized in the top 3 lines of Table 7.3 for SK-I and Table 7.4 for SK-II.

7.4 Variables for Distinguishing tau-like events

In accordance with the event shape and characteristics of tau lepton decays, a set of five variables are defined to further discriminate ν_τ signals from backgrounds and construct a likelihood function :

(a) Visible energy (E_{vis})

(b) Maximum distance between the primary vertices of ν_τ CC interactions and electron vertices from pion and then muon decays

(c) Number of ring candidates

(d) Sphericity in the laboratory frame

(e) Clustered sphericity in the center of mass frame

The first two variables are Super-K standard variables. The visible energy (E_{vis}) is defined as the total energy deposited from all of the Cherenkov rings in an event assuming that all rings are produced by electrons. The visible energy for ν_τ events are higher than that for the atmospheric neutrino events. The second variable is to tag extra pions in tau lepton decays. The number of ring candidates is determined by a ring-finding algorithm, which is based on the Hough transformation (Section 6.2) and is sensitive to ring-fragments. The last two variables, sphericity and clustered sphericity, are derived from a special "energy flow" analysis, which is an event fitting procedure utilizing a jet-based event shape analysis often used in collider physics experiments. The energy flow analysis uses Cherenkov patterns to deconvolve the measured light distribution in the Super-K detector. By associating the deconvoluted

power spectrum with pseudo particles, "jets" are reconstructed, and event shape variables such as sphericity are obtained. The details of the energy flow analysis are described in Appendix B. Sphericity ($0 < S < 1$) measures the spherical symmetry of an event and equals one if the event is spherically symmetric. It also has a quadratic momentum dependence giving more weight to higher momentum particles [176, 177]. Clustering is therefore a good way to examine events in different energies. The sphericity in the lab frame and in the center of mass frame is not strongly correlated since it is not invariant under the Lorentz transformation. The sphericity calculated with different clustering and reference frames probes different event characteristics.

The expected distributions of each variable after applying the initial ν_τ event selection criteria for both signal and background events are plotted in Figure 7.3 for SK-I and Figure 7.4 for SK-II.

The background MC is compared with downward-going data, where no tau neutrino appearance signal is expected as the probability for ν_μ oscillating into ν_τ is very small for the given path length and the measured atmospheric Δm^2. The agreement of the downward-going data and background MC indicates the variables chosen for this analysis are well modeled by our MC simulation. The small discrepancy in log(Sphericity) between the data and the atmospheric neutrino MC is consistent with the systematic uncertainty in the vertex position.

The difference in the variable distributions between SK-I and SK-II is due to the difference in the number of PMTs in the ID for SK-I and SK-II (SK-II has only 47 % of ID PMTs compared to SK-I). SK-II has slightly worse resolution, and events detected in the SK-II detector have less multiplicity. Figure 7.5 shows the distributions of the number of rings for SK-I and SK-II Multi-GeV atmospheric neutrino MC events, and the number of rings found in SK-II is less than that of SK-I.

7.5 The Likelihood

A likelihood function is constructed using the five variables described above. The data sample is divided into 5 energy bins : (1) $E_{vis} < 2.0$, (2) $2.0 \leq E_{vis} < 3.0$, (3) $3.0 \leq E_{vis} < 6.0$, (4) $6.0 \leq E_{vis} < 12.0$, (5) $12.0 \leq E_{vis}$ [GeV].

The probability density functions (PDFs) are built for each variable by defining probability functions, $\mathcal{P}_{\rm tau}$ for ν_τ signals and $\mathcal{P}_{\rm bkg}$ for the atmospheric neutrino background. The log likelihood is given by :

$$log(\mathcal{L}) \;=\; \sum_{i=1}^{5} log\left(\frac{\mathcal{P}_{\rm tau}}{\mathcal{P}_{\rm bkg}}\right)_i$$

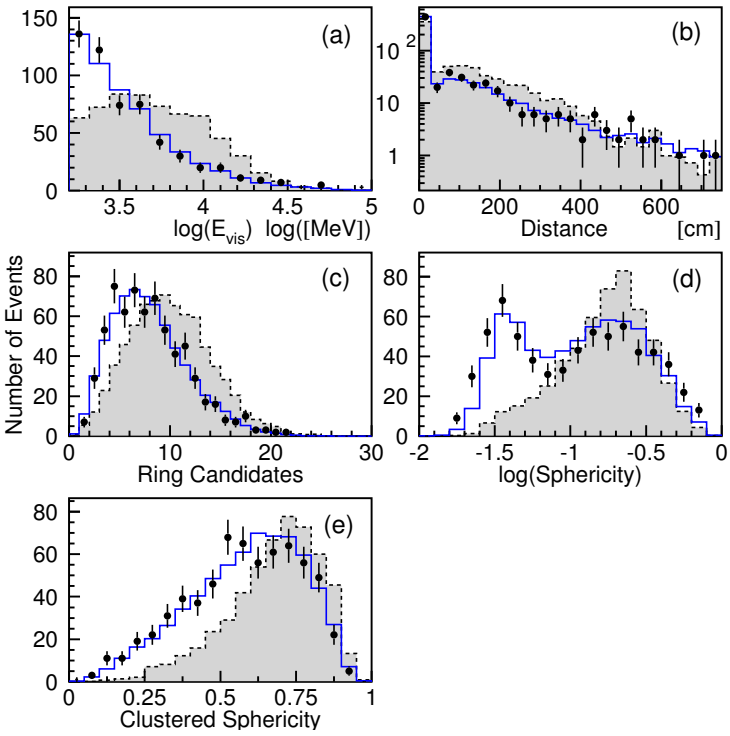

Figure 7.3: The distributions of likelihood variables after applying the initial ν_τ event selection criteria for downward-going data (points), ν_τ MC (shaded histogram), and atmospheric $\nu_{e,\mu}$ background MC events (solid histogram) : (a) Visible energy, (b) Maximum distance between the primary interaction and electron vertices from pions and then μ decays, (c) Number of ring candidates, (d) Sphericity in the laboratory frame, and (e) Clustered sphericity in the center of mass (The histograms of ν_τ MC are normalized arbitrarily.). In the likelihood analysis, the data sample is divided into 5 energy bins.

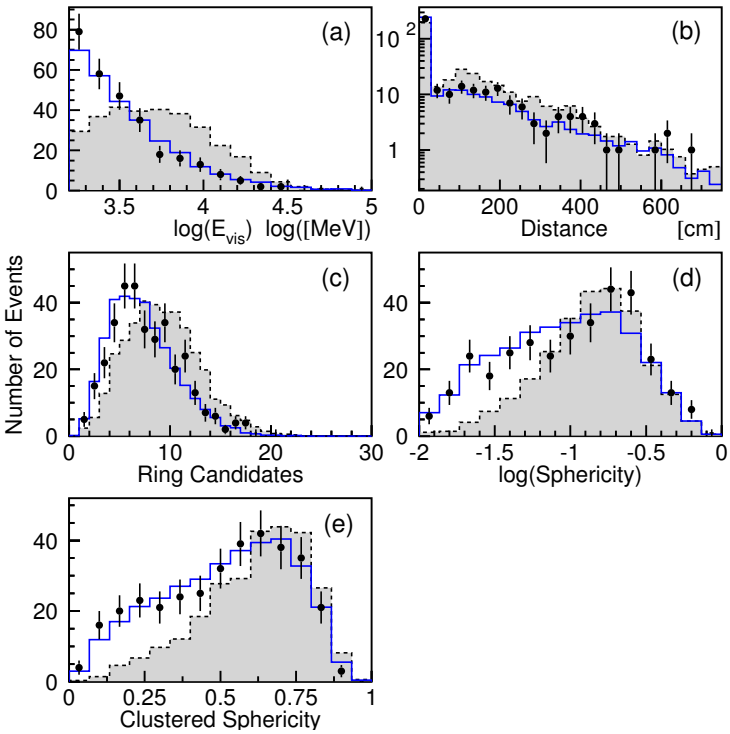

Figure 7.4: The distributions of variables after applying the initial ν_τ event selection criteria for downward-going data (points), ν_τ MC (shaded histogram), and atmospheric $\nu_{e,\mu}$ background MC events (solid histogram) : (a) Visible energy, (b) Maximum distance between the primary interaction and electron vertices from pions and then μ decays, (c) Number of ring candidates, (d) Sphericity in the laboratory frame, and (e) Clustered sphericity in the center of mass (The histograms of ν_τ MC are normalized arbitrarily.). In the likelihood analysis, the data sample is divided into 5 energy bins.

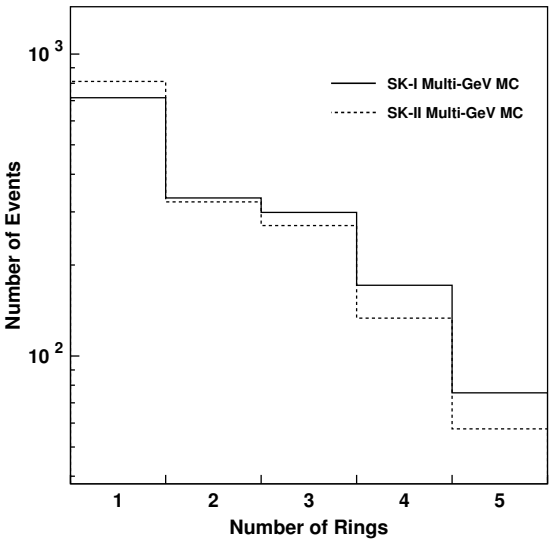

Figure 7.5: The distributions of the number of rings for SK-I (solid) and SK-II (dashed) atmospheric neutrino MC events.

$$= \sum_{i=1}^{5} \Big[log(\mathcal{P}_{\rm tau})_i - log(\mathcal{P}_{\rm bkg})_i \Big] \tag{7.1}$$

where index i is for each variable. As mentioned in Section 7.2, the extra set of atmospheric neutrino and ν_τ MCs are generated to construct the likelihood function without introducing any bias.

The likelihood distributions for downward-going and upward-going events are shown in Figure 7.6 for SK-I and Figure 7.7 for SK-II.

The events for likelihood $\mathcal{L} > 0$ are defined to be tau-like. The sensitivity of the likelihood cut ($L > 0$) is tested as shown in Figure 7.8.

The likelihood distributions of data and background MC events agree for downward-going events, which validates our analysis method. Table 7.3 and Table 7.4 summarize the number of data, atmospheric neutrino background MC, and ν_τ MC events after applying all of the event selection criteria. The overall efficiency to select ν_τ events is estimated to be 43 % for SK-I and 40 % for SK-II.

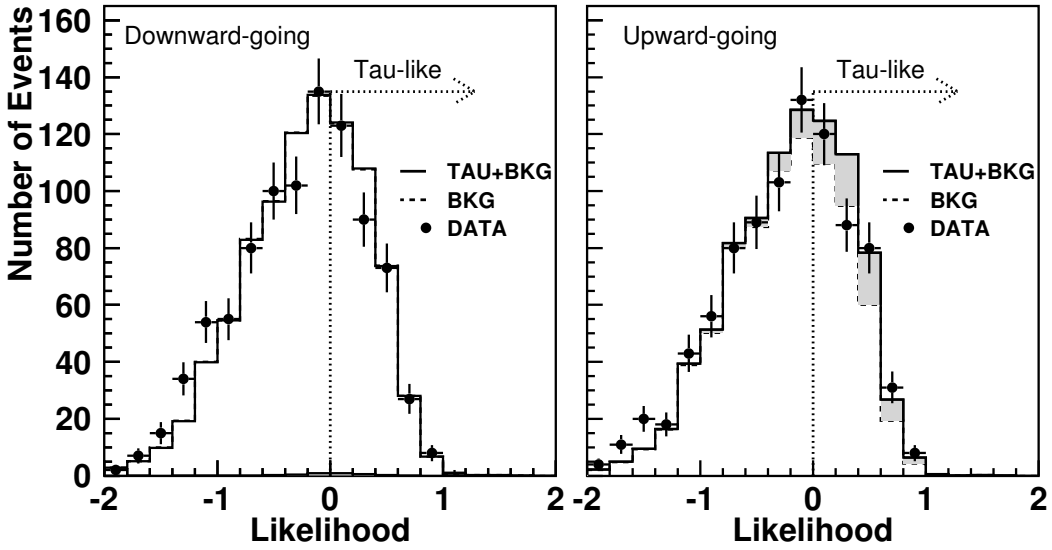

Figure 7.6: The SK-I likelihood distributions of downward-going (left) and upward-going (right) events for data (points), atmospheric neutrino background MC (dashed histogram), and the best fit including tau neutrino and backgrounds (solid histogram). The shaded area shows a fitted excess of tau neutrino events in the upward-going direction. The events for likelihood $\mathcal{L}$ > 0.0 are defined to be tau-like.

Table 7.3: Summary for the numbers of events in SK-I data, atmospheric neutrino ($\nu_{e,\mu}$) background MC, and ν_τ MC after applying each of tau neutrino event selection criteria and the likelihood cut analysis. Neutrino oscillation is considered in the MCs with the oscillation parameters: $\Delta m^2 = 2.4 \times 10^{-3}$ eV^2 and $\sin^2 2\theta = 1.0$, and the numbers are normalized by the live time of the SK-I data sample.

SK-I	Data	$\nu_{e,\mu}$ BKG MC	CC ν_τ MC
Generated in fiducial volume	–	17135 (100 %)	78.4 (100 %)
$E_{vis} > 1.33$ GeV	2888	2943 (17.2 %)	51.5 (65.7 %)
Most energetic ring e-like	1803	1765 (10.3 %)	47.1 (60.1 %)
Likelihood > 0.0	649	647 (3.8 %)	33.8 (43.1 %)

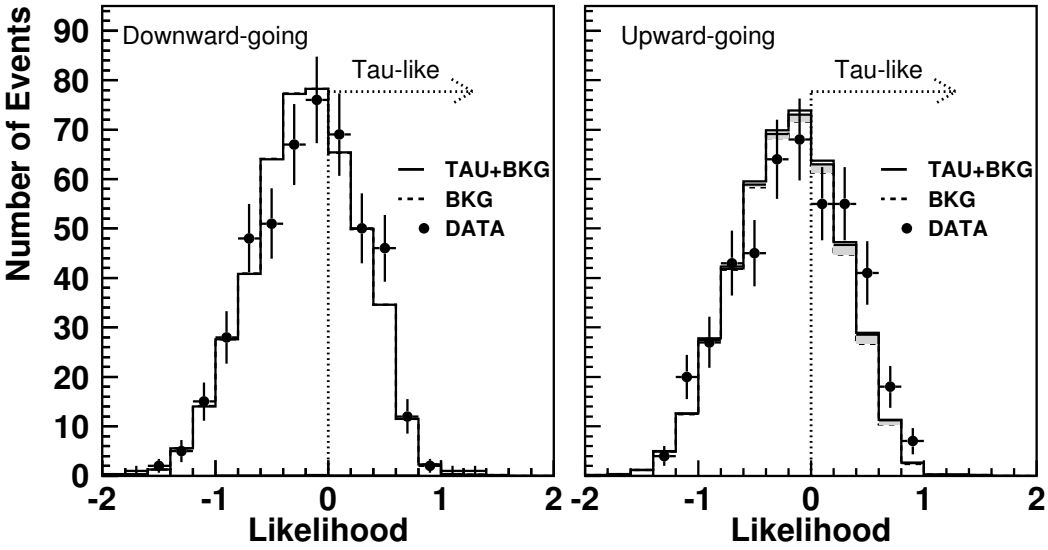

Figure 7.7: The SK-II likelihood distributions of downward-going (left) and upward-going (right) events for data (points), atmospheric neutrino background MC (dashed histogram), and the best fit including tau neutrino and backgrounds (solid histogram). The shaded area shows a fitted excess of tau neutrino events in the upward-going direction. The events for likelihood $\mathcal{L}$ > 0.0 are defined to be tau-like.

Table 7.4: Summary for the numbers of events in SK-II data, atmospheric neutrino ($\nu_{e,\mu}$) background MC, and ν_τ MC after applying each of tau neutrino event selection criteria and the likelihood cut. Neutrino oscillation is considered in the MCs with the oscillation parameters: $\Delta m^2 = 2.4 \times 10^{-3}$ eV^2 and $\sin^2 2\theta = 1.0$, and the numbers are normalized by the live time of the SK-II data sample.

SK-II	Data	$\nu_{e,\mu}$ BKG MC	CC ν_τ MC
Generated in fiducial volume	–	9040 (100 %)	42.7 (100 %)
$E_{vis} > 1.33$ GeV	1493	1553 (17.2 %)	28.5 (66.7 %)
Most energetic ring e-like	921	930.5 (10.3 %)	25.9 (60.7 %)
Likelihood > 0.0	357	318.2 (3.5 %)	17.3 (40.5 %)

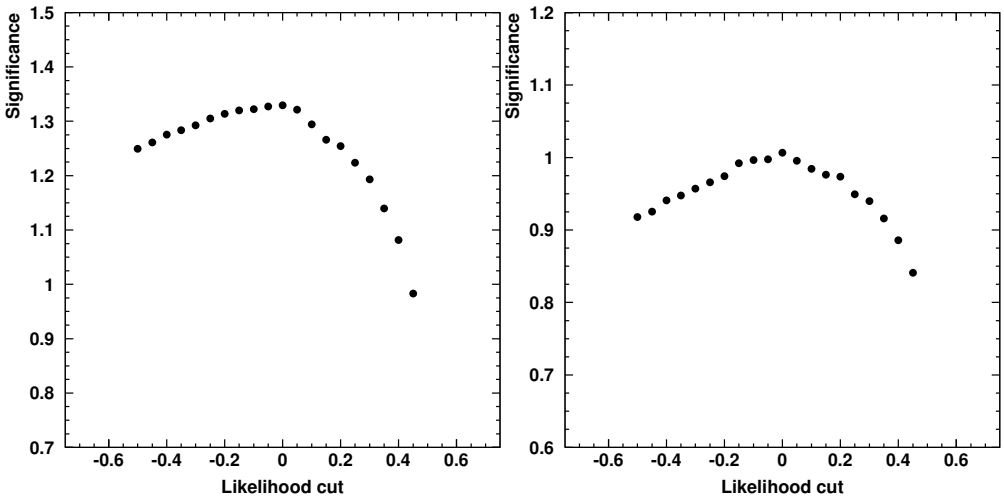

Figure 7.8: The sensitivity of the likelihood cut for SK-I (left) and SK-II (right) are shown and is tested by shifting the cut value from -0.5 to 0.5. The likelihood cut at $\mathcal{L} = 0.0$ is optimal.

7.6 Zenith Angle Fit

After selecting the tau-enriched sample by applying the ν_τ event selection criteria with the likelihood ($\mathcal{L} > 0$) cut, the zenith angle distribution is fitted with a combination of the expected ν_τ signals resulting from oscillations and the predicted atmospheric neutrino background events including oscillations. The fitted zenith angle distribution and the χ^2, which is minimized, are given by :

$$N_{\rm total}(\cos\theta) = \alpha N_{\rm tau} + \beta N_{\rm bkg}, \tag{7.2}$$

$$\chi^2 = \sum_{i=1}^{10} \frac{\left(N_i^{\rm obs} - \alpha N_i^{\rm tau} - \beta N_i^{\rm bkg}\right)^2}{\sigma_i^2}, \tag{7.3}$$

where $N_i^{\rm obs}$ is the number of the observed events, $N_i^{\rm tau}$ is the number of expected ν_τ MC events, $N_i^{\rm bkg}$ is the MC predicted number of atmospheric neutrino background events, and σ_i is the statistical error for the i-th bin. The sample normalizations, α and β are allowed to vary freely. The zenith angle distribution is divided into 10 bins, from -1 to 1 ($\cos\theta = -1$ ($\cos\theta = 1$) refers to upward-going (downward-going) events). The results of the fit are shown in Figure 7.9 for SK-I and Figure 7.10 for SK-II.

The minimum χ^2 for the zenith angle fit for SK-I and SK-II are χ^2_{min} = 7.6/8 DOF and 7.5/8 DOF, and the χ^2 assuming no tau neutrino appear-

Table 7.5: Fraction of neutrino interaction modes in atmospheric neutrino background MC events after applying all the ν_τ event selection criteria for SK-I and SK-II.

		SK-I	SK-II
CC $\nu_e + \overline{\nu}_e$	QE	2.3%	3.8%
	Single meson	8.2%	8.5%
	DIS	41.4%	40.0%
	total	51.9%	52.3%
CC $\nu_\mu + \overline{\nu}_\mu$	QE	<0.1%	<0.1%
	Single meson	0.6%	0.5%
	DIS	19.9%	20.0%
	total	20.6%	20.6%
NC		27.5%	27.1%

ance are 16.3/9 DOF and 7.9/9 DOF. The normalizations of the best fit are $\alpha = 1.76 \pm 0.61$ and $\beta = 0.90 \pm 0.05$ for SK-I and $\alpha = 0.43 \pm 0.83$ and $\beta = 1.07 \pm 0.07$ for SK-II. After correcting for efficiencies, these correspond to a best fit tau neutrino appearance signal of 138 ± 48 (stat.) and 18.4 ± 35.5 (stat.) for SK-I and SK-II analyses. For SK-I, an excess of tau neutrino signals is observed in the upward-going direction, and the data distribution agrees better with the prediction including tau neutrino appearance estimated by MC as can be seen in Figure 7.9. For SK-II, the normalization of tau signals is small, but since the statistics is rather limited and the uncertainty is large, it is still consistent with SK-I.

The backgrounds that remain after applying all of the ν_τ event selection criteria are mostly deep-inelastic scattering; for SK-I, CC DIS: 61.4 % and NC DIS: 27.1 %, and for SK-II, CC DIS: 60.0 % and NC DIS: 26.8 %. Table 7.5 summaries the interaction modes in the background events.

A similar analysis is also conducted with an alternate statistical method utilizing neural network (NN) by another Super-K collaborator. A neural network is trained with the same five variables. The network has 6 input neurons, 10 hidden neurons, and one sigmoid output neuron and is trained using back-propagation by use of the MLPFIT neural network package [178]. The results are shown in Ref. [179].

A study to check dependency on Monte Carlo neutrino interaction models is performed using another model, NUANCE [181]. The difference in the results is negligible.

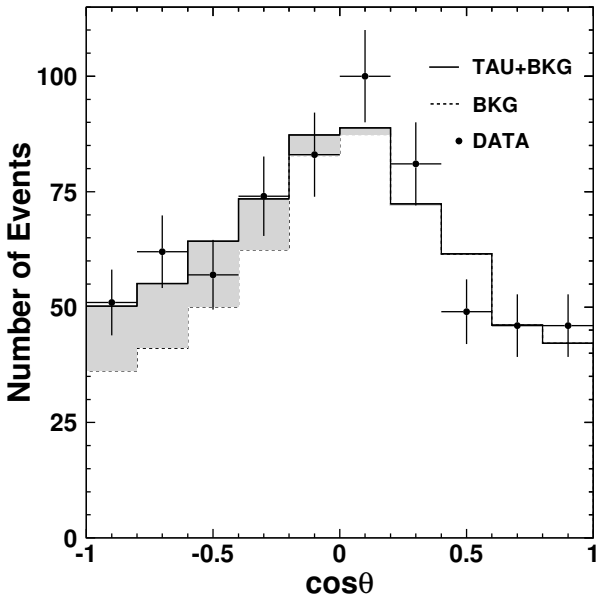

Figure 7.9: The zenith angle distribution for SK-I. The zenith angle $\cos(\theta)$ $= -1$ ($\cos(\theta) = +1$) indicates upward-going (downward-going). Assuming neutrino oscillation with ($\sin^2 2\theta$, Δm^2) = (1.0, 2.4×10^{-3} eV^2), the data are fitted after ν_τ event selection criteria and the likelihood cut are applied. The solid histogram shows the best fit including ν_τ, and the dashed histogram shows the background events of ν_e and ν_μ from atmospheric neutrinos. A fitted excess of tau-like events in the upward-going direction is shown in the shaded area.

Table 7.6: Summary of tau and background normalization for zenith angle fit.

	Tau norm.(α)	Bkg norm.(β)	χ^2/DOF
SK-I	1.76 ± 0.61	0.90 ± 0.05	7.6/8
SK-II	0.43 ± 0.83	1.07 ± 0.07	7.5/8
SK-I+SK-II	1.34 ± 0.49	0.96 ± 0.02	19/18

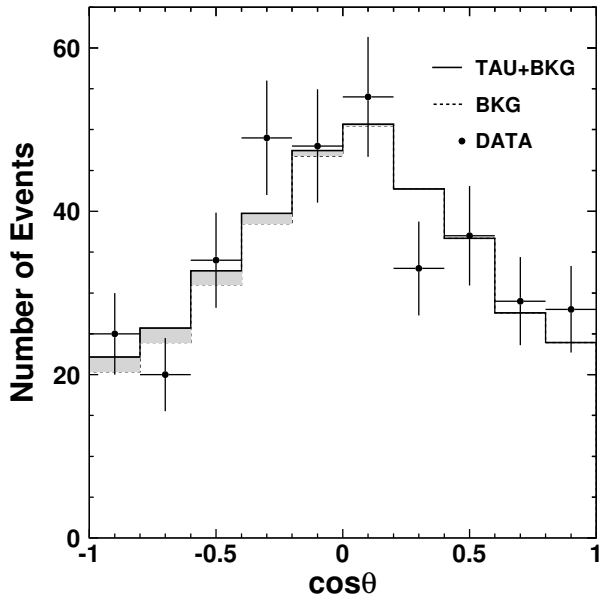

Figure 7.10: The zenith angle distribution for SK-II. The zenith angle $\cos(\theta) = -1$ ($\cos(\theta) = +1$) indicates upward-going (downward-going). Assuming neutrino oscillation with $(\sin^2 2\theta,\ \Delta m^2) = (1.0,\ 2.4 \times 10^{-3}\ \mathrm{eV}^2)$, the data are fitted after ν_τ event selection criteria and the likelihood cut are applied. The solid histogram shows the best fit including ν_τ, and the dashed histogram shows the background events of ν_e and ν_μ from atmospheric neutrinos. A fitted excess of tau-like events in the upward-going direction is shown in the shaded area.

7.7 Zenith angle fit with SK-I and SK-II data

To combine both SK-I and SK-II data, a zenith angle distribution is fitted with common tau and background sample normalizations with 20 zenith angle bins; the first 10 bins are for SK-I data and the second 10 bins are for SK-II data. Since the detector responses and the event selection efficiencies are different in SK-I and SK-II, both data sets can not be simply added together. The chi-squared, which is minimized, is given by :

$$\chi^2_{\mathrm{SK-I+SK-II}} = \sum_{i=1}^{10} \left[\frac{\left(N_i^{\mathrm{obs}} - \alpha N_i^{\mathrm{tau}} - \beta N_i^{\mathrm{bkg}} \right)^2}{\sigma_i^2} \right]_{\mathrm{SK-I}} + \sum_{i=11}^{20} \left[\frac{\left(N_i^{\mathrm{obs}} - \alpha N_i^{\mathrm{tau}} - \beta N_i^{\mathrm{bkg}} \right)^2}{\sigma_i^2} \right]_{\mathrm{SK-II}}, \tag{7.4}$$

where the index i is for SK-I and SK-II zenith bins; $1 \leq i \leq 10$ for SK-I and $11 \leq i \leq 20$ for SK-II, N_i^{obs} is the number of the observed events, N_i^{tau} is the number of expected ν_τ events, N_i^{bkg} is the MC predicted number of atmospheric neutrino background events, and σ_i is the statistical error. The sample normalizations, α and β are common to SK-I and SK-II and are allowed to vary freely.

The minimum χ^2 for the zenith angle fit for the combined data set of SK-I and SK-II is $\chi^2_{min} = 19/18$ DOF, and the χ^2 assuming no tau neutrino appearance is 30.2/19 DOF. The normalizations of the best fit for the fit are $\alpha = 1.34 \pm 0.49$ and $\beta = 0.96 \pm 0.02$. After correcting for efficiencies, these correspond to a best fit tau neutrino appearance signal of 162.3 ± 59.3 (stat.) for SK-I + SK-II. Figure 7.11 shows the combined zenith angle fit for the SK-I and the SK-II data.

The systematic errors from the neutrino flux and neutrino interactions as well as the oscillation parameters are in common for SK-I and SK-II, but the detector responses and efficiencies in event selections and reconstructions are treated independently for SK-I and SK-II.

7.8 Systematic Uncertainties

Each systematic error term in this analysis is described in this section. Since the event sample used in this analysis is FC Multi-GeV events, the uncertainties only relevant to those events are considered.

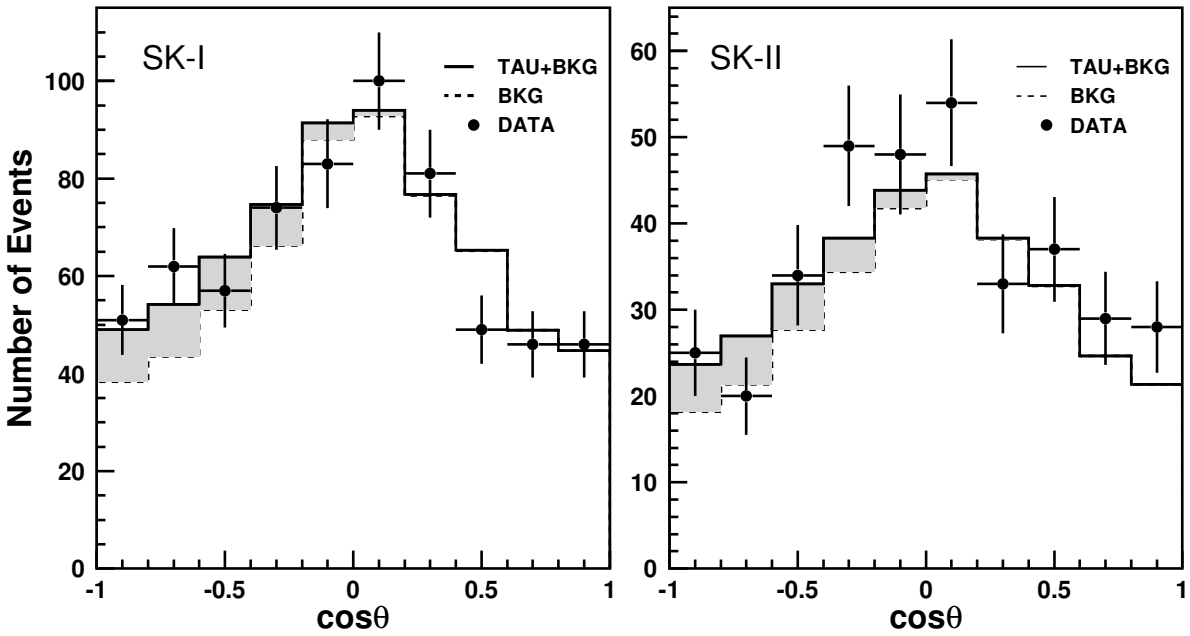

Figure 7.11: The zenith angle distributions of the combined fit for the SK-I (left) and the SK-II (right) data. The zenith angle $\cos(\theta) = -1$ ($\cos(\theta) = +1$) indicates upward-going (downward-going). Assuming neutrino oscillation with $(\sin^2 2\theta,\ \Delta m^2) = (1.0,\ 2.4 \times 10^{-3}\ \mathrm{eV}^2)$, both SK-I and SK-II data are fitted together after ν_τ event selection criteria and the likelihood cut are applied. The solid histogram shows the best fit including ν_τ, and the dashed histogram shows the background events of ν_e and ν_μ from atmospheric neutrinos. A fitted excess of tau-like events in the upward-going direction is shown in the shaded area.

The systematic uncertainties for the observed number of ν_τ events are indicated by "For the observed number of ν_τ events" in parentheses. The estimated values for each error is summarize in Table 7.7 - 7.11.

7.8.1 Systematic Uncertainties in Atmospheric Neutrino Flux

- **Absolute flux normalization :**
  Absolute flux normalization uncertainty in the atmospheric neutrino flux calculations is estimated to be 20 % below 100 GeV and 30 % above 100 GeV. This originates from the uncertainty in the primary cosmic ray flux and the hadronic interaction models used in the calculations. In this analysis, the uncertainty due to the absolute flux normalization is set to be 20 %.

- **Flavor ratio :**

  - $(\nu_\mu + \overline{\nu}_\mu)/(\nu_e + \overline{\nu}_e)$ for $E_\nu < 5\,\mathrm{GeV}$
  - $(\nu_\mu + \overline{\nu}_\mu)/(\nu_e + \overline{\nu}_e)$ for $E_\nu > 5\,\mathrm{GeV}$

  The flavor ratio $(\nu_\mu + \overline{\nu}_\mu)/(\nu_e + \overline{\nu}_e)$ in the atmospheric neutrino flux is calculated within approximately 5 % by different models. The systematic error is 3 % for $E_\nu < 5\,\mathrm{GeV}$. For $E_\nu > 5\,\mathrm{GeV}$, the error increases linearly with $\log E_\nu$ from 3 % (5 GeV) to 10 % (100 GeV). In the low energy range, the uncertainty is due to the pion spectrum in the primary hadronic interactions. In the high energy range, the uncertainty is mainly due to the K/π production ratio.

- **Anti-neutrino/neutrino ratio :**

  - $\overline{\nu}_e/\nu_e$ for $E_\nu < 10\,\mathrm{GeV}$
  - $\overline{\nu}_e/\nu_e$ for $E_\nu > 10\,\mathrm{GeV}$
  - $\overline{\nu}_\mu/\nu_\mu$ for $E_\nu < 10\,\mathrm{GeV}$
  - $\overline{\nu}_\mu/\nu_\mu$ for $E_\nu > 10\,\mathrm{GeV}$

  Systematic uncertainty of anti-neutrino to neutrino ratio is due to π^+/π^- ratio in hadronic interactions predicted by the cosmic ray flux calculations. The uncertainty in $\overline{\nu}_e/\nu_e$ and $\overline{\nu}_\mu/\nu_\mu$ is estimated to be 5 % for $E_\nu < 10\,\mathrm{GeV}$. For $E_\nu > 10\,\mathrm{GeV}$, the error in $\overline{\nu}_e/\nu_e$ increases linearly with $\log E_\nu$ from 5 % (10 GeV) to 10 % (100 GeV), and the error in $\overline{\nu}_\mu/\nu_\mu$ increases linearly with $\log E_\nu$ from 5 % (10 GeV) to 25 % (100 GeV).

- **Up/down ratio :** (For the observed number of ν_τ events)
  The systematic uncertainties of up/down ratio are estimated by comparing independent flux models, which predict zenith angle distributions in Super-Kamiokande. Although only FC Multi-GeV event sample is used in this analysis, the up/down uncertainty in the neutrino flux is assumed to be fully correlated with each event samples of Sub-GeV and PC, that is all of the samples are simultaneously varied by the systematic error factors. For FC Multi-GeV events, the uncertainty is 1.5 % (e-like), 0.8 % (μ-like), and 0.7 % (Multi-ring μ-like).

- **Horizontal/vertical ratio :** (For the observed number of ν_τ events)
  The systematic uncertainties of horizontal/vertical ratio is due to the difference in the 3D calculation methods for each models for neutrino energy below 10 GeV and is due to the predicted K/π ratio in hadronic interactions in the atmosphere. This uncertainty is also assumed to be correlated with each event sample. For FC Multi-GeV events, the error is 2.8 % (e-like), 1.9 % (μ-like), and 1.3 % (Multi-ring μ-like).

- **K/π ratio :** (For the observed number of ν_τ events)
  The uncertainty in K/π production ratio in cosmic ray interactions in the atmosphere is estimated to be 20 %.

- **Energy Spectrum above 100 GeV :**
  The energy spectrum of primary cosmic ray is proportional to E^γ with the spectral index for the primary proton flux, $\gamma = 2.74$. For the energy above 100 GeV, the uncertainty in the energy spectral index is 0.05.

- **Solar activity :**
  The flux of primary cosmic rays is affected by solar activity changing in every 11 year period, and the atmospheric neutrino flux calculations considers the solar activity. The uncertainty is estimated to be 0.2 % for SK-I and 0.5 % for SK-II by introducing $\pm$ 1 year of uncertainty to the modulation of solar activity.

7.8.2 Systematic Uncertainties in Neutrino Interactions

As described in Chapter 4, the neutrino cross sections and kinematics are calculated theoretically and measured by several experiment. The error terms considered are listed in the following.

- **Quasi-elastic scattering and single-meson production (M_A) :**
  The axial vector mass M_A is set to be 1.11 in our simulation (Chapter 4),

which is estimated by the experimental measurements. The uncertainty in the M_A affects the angular correlations between incident neutrinos and outgoing leptons and is set to be 10 %.

- **Quasi-elastic scattering (Model dependence in nuclear effect) :**
  The uncertainty in the QE nuclear effect is estimated by comparing two models by Ref. [110] and Ref. [112], and is set to be 1-σ.

- **Quasi-elastic scattering (Total cross section) :**
  The uncertainty in the QE cross section is estimated to be 10 %.

- **Single-meson production (Total cross section) :**
  The uncertainty in the single-meson production cross section is estimated to be 10 %.

- **Deep-inelastic scattering (Model dependence in a few GeV region) :**
  For neutrino energy above a few tens of GeV, the cross section calculation agree with the experimental measurements within 5 %, but in the lower energy region, the uncertainties are large. The uncertainty in the DIS is estimated by taking the difference between the models by Ref. [133] and by A. Bodek and U. K. Yang [180]. The difference in these two models depends on the square of 4-momentum transfer q^2 and is quite large in a few GeV energy region. The uncertainty is 1-σ.

- **Deep-inelastic scattering (Total cross section) :**
  The uncertainty in the DIS total cross section is estimated to be 5.0 %.

- **Coherent-pion production (Total cross section) :**
  The uncertainty in the Coherent-pion production total cross section is estimated to be 30 %.

- **NC/CC ratio :** (For the observed number of ν_τ events)
  The systematic uncertainty in the NC/CC ratio is estimated to be 20 %.

- **Nuclear Effect in ^{16}O nucleus :**
  The systematic uncertainty in the mean free path of hadrons produced via neutrino interactions in the ^{16}O nucleus is estimated to be 30 %.

- **Nuclear Effect in pion spectrum :**
  The difference in the predicted pion energy spectrum by NEUT [107] and NUANCE [108] interaction models is taken to be 1-σ.

- **Charge-current ν_τ interaction :**
  The systematic uncertainty in the ν_τ cross sections for CC interactions is estimated to be 25 % by comparing two models of NEUT [107] and Hagiwara *et al.* [171].

7.8.3 Systematic Uncertainties in Event Selection

- **Reduction efficiency for FC events :**
  The systematic uncertainty in the FC reduction efficiency is estimated to be 0.2 % (SK-I) and 0.19 % (SK-II) by changing the event selection cuts.

- **FC/PC separation :**
  The FC and PC events are separated by the number of hit PMTs in the OD hit PMT cluster (NHITAC). The systematic uncertainty in the FC/PC separation is estimated to be 0.9 % (SK-I) and 0.5 % (SK-II) from the difference between data and MC NHITAC distributions.

- **Hadron simulation :**
  The uncertainty in the hadron simulation is estimated by comparing the model used in our detector simulation, CALOR [165], and the FLUKA model. The uncertainty affects the contamination of NC interactions in single-ring μ-like, i.e. hadrons (mostly pions) in NC interactions are identified as μ-like events. The uncertainty is 1-σ for both SK-I and SK-II.

- **Non-ν background :**

  – Multi-GeV e-like

  – Multi-GeV μ-like

  The backgrounds for Multi-GeV e-like events and for Multi-GeV μ-like events are flasher PMTs and cosmic ray muons, respectively. The uncertainties in the e-like and for μ-like are 0.2 % and 0.1 % (SK-I), and 0.7 % and 0.1 % (SK-II).

7.8.4 Systematic Uncertainties in Event Reconstruction

- **Ring separation (single-ring/multi-ring separation) :**

  – Multi-GeV e-like

  - Multi-GeV μ-like

  The ring-counting algorithm is described in Section 6.2. The systematic error in single-ring/multi-ring separation is due to the uncertainties in water transparency and tracking of hadrons in water. The uncertainties are estimated by comparing the ring counting likelihood distributions for the observed data with that for the Monte Carlo events. The uncertainties in the Multi-GeV e-like and in the Multi-GeV μ-like are 15.9 % and 6.2 % (SK-I), and 3.7 % and 1.5 % (SK-II).

- **Particle Identification :**

  - Multi-GeV e-like
  - Multi-GeV μ-like
  - Multi-GeV multi-ring μ-like

  The systematic errors in the particle identification are estimated by taking the difference in the PID likelihood distributions between data and MC (see Section 6.3). The uncertainties in the Multi-GeV e-like, Multi-GeV μ-like, and Multi-GeV multi-ring μ-like are 0.4 %, 0.4 %, and 4.7 % (SK-I), and 0.2 %, 0.2 %, and 9.1 % (SK-II).

- **Energy Calibration for FC events (Absolute energy scale) :**
  Absolute energy scale is calibrated as described in Chapter 3, and the systematic uncertainty is estimated to be 2 % (SK-I) and 2.5 % (SK-II).

- **Up/down symmetry of energy calibration :** (For the observed number of ν_τ events)
  The difference in the energy scale for upward-going and downward-going events is measured using decay electrons from cosmic ray stopping muons. The up/down asymmetry of the energy scale is estimated to be 0.6 % for SK-I and SK-II.

7.8.5 Systematic Uncertainties in ν_τ Appearance analysis

- **ν_τ selection cut efficiency :**
  Before calculating the tau likelihood function, the initial ν_τ selection cut (the most energetic ring is e-like) is applied. The uncertainty in the cut efficiency is estimated by shifting the PID distribution for Multi-GeV multi-ring e-like events by $\pm$ 0.42.

- **Tau likelihood selection efficiency :**
  The uncertainty in the tau likelihood selection ($\mathcal{L} > 0.0$) is estimated by shifting the cut value by $\pm$ 0.02.

- **Polarization of Tau leptons :**
  The uncertainty is estimated by comparing two MC sets; one with the polarization from the calculation by Hagiwara *et al.* [171] and the other with fully polarized tau leptons.

7.8.6 Systematic Uncertainties in Oscillation Parameters

- **Mass-squared difference Δm^2_{23} :**
  The uncertainties in Δm^2_{23} are estimated by using 68 % C.L. allowed parameter region obtained by the L/E analysis from Super-K [49, 47] and $0.0020\,\mathrm{eV}^2 < \Delta m^2_{23} < 0.0027\,\mathrm{eV}^2$.

- **Mixing angle θ_{23} :**
  The uncertainties in θ_{23} are also estimated by using 68 % C.L. allowed parameter region obtained by the L/E analysis from Super-K, and $0.93 < \sin^2 2\theta_{23} < 1.00$.

- **Mixing angle θ_{13} :**
  The uncertainties in θ_{13} are estimated by using the limit obtained by the CHOOZ reactor neutrino experiment [182], and $0.0 < \sin^2 2\theta_{13} < 0.15$.

Table 7.7: (Common to SK-I and SK-II) Summary of systematic uncertainties in the prediction of the atmospheric neutrino flux and neutrino interactions. Estimated uncertainty and the best-fit value are listed for each error.

Uncertainty common for SK-I and SK-II			uncertainty (%)	Best-fit (%)
(A) Systematic uncertainties in neutrino flux				
Absolute normalization			20	20
Flavor ratios:		$E_\nu < 5.0\,\mathrm{GeV}$	3.0	0.5
$(\nu_\mu + \overline{\nu}_\mu)/(\nu_e + \overline{\nu}_e)$		$E_\nu > 5.0\,\mathrm{GeV}$	3.0 - 10.0	0.5
$\overline{\nu}/\nu$ ratio:	$\overline{\nu}_e/\nu_e$	$E_\nu < 10.0\,\mathrm{GeV}$	5.0	0.1
		$E_\nu > 10.0\,\mathrm{GeV}$	5.0 - 10.0	0.4
	$\overline{\nu}_\mu/\nu_\mu$	$E_\nu < 10.0\,\mathrm{GeV}$	5.0	0.5
		$E_\nu > 10.0\,\mathrm{GeV}$	5.0 - 10.0	0.4
Up/down ratio			0.4 - 2.1	8.6
Horizontal/vertical ratio			0.3 - 2.8	4.7
K/π ratio			20	2.9
Energy spectrum			0.05	0.6
(B) Systematic uncertainties in neutrino interaction				
QE scattering and single-meson production (M_A)			10.0	0.3
QE scattering (model dependence)			1.0	<0.1
QE scattering (total cross-section)			10.0	0.6
Single-meson production (total cross-section)			10.0	0.1
DIS (model dependence: a few GeV region)			1.0	1.8
DIS (total cross-section)			5.0	0.4
Coherent pion production (total cross-section)			30.0	<0.1
NC/CC ratio			20.0	4.7
Nuclear effect in ^{16}O nucleus			30.0	1.4
Nuclear effect in pion spectrum			1.0	<0.1
Charged-current ν_τ interaction (ν_τ CC cross-section)			Neut vs Hagiwara	25
Hadron Simulator			Calor vs Fluka	<0.1

Table 7.8: (For only SK-I) Summary of systematic uncertainties in event selection. Estimated uncertainty and the best-fit value are listed for each error.

Systematic uncertainties only for SK-I			uncertainty (%)	Best-fit (%)
(C) Systematic uncertainties in event selection				
Reduction for fully contained event			0.2	0.2
FC/PC relative normalization			0.9	<0.1
Non-ν background	Multi-GeV	e-like	0.2	0.1
		μ-like	0.1	<0.1
(D) Systematic uncertainties in event reconstruction				
Ring separation	Multi-GeV	e-like	15.9	1.6
		μ-like	6.2	1.6
Particle identification	Multi-GeV	e-like	0.4	0.3
		μ-like	0.4	0.3
	Multi-GeV	Multi-ring μ	4.7	0.5
Energy calibration for FC event			2.0	0.8
Up/down symmetry of energy calibration			0.6	1.3
(E) Systematic uncertainties only related to ν_τ appearance analysis				
Tau Likelihood selection efficiency			LH$\pm$0.02	2.5
ν_τ event selection efficiency			PID-LH$\pm$0.42	0.4
Tau Lepton Polarization			Full vs Partial	3.1

Table 7.9: (For only SK-II) Summary of systematic uncertainties in event selection. Estimated uncertainty and the best-fit value are listed for each error.

Systematic uncertainties only for SK-II			uncertainty (%)	Best-fit (%)
(C) Systematic uncertainties in event selection				
Reduction for fully contained event			0.2	<0.1
FC/PC relative normalization			0.5	<0.1
Non-ν background	Multi-GeV	e-like	0.7	0.1
		μ-like	0.1	<0.1
(D) Systematic uncertainties in event reconstruction				
Ring separation	Multi-GeV	e-like	3.7	<0.1
		μ-like	1.5	<0.1
Particle identification	Multi-GeV	e-like	0.2	0.1
		μ-like	0.2	0.1
	Multi-GeV	Multi-ring μ	9.1	0.1
Energy calibration for FC event			2.5	0.2
Up/down symmetry of energy calibration			0.6	0.3
(E) Systematic uncertainties only related to ν_τ appearance analysis				
Tau Likelihood selection efficiency			LH$\pm$0.02	2.3
ν_τ event selection efficiency			PID-LH$\pm$0.42	1.5
Tau Lepton Polarization			Full vs Partial	3.1

Table 7.10: (Common to SK-I and SK-II) Summary of systematic uncertainties in oscillation parameters. Estimated uncertainty and the best-fit value are listed for each error.

Common for SK-I and SK-II	uncertainty (%)	Best-fit (%)
(F) Systematic uncertainties in oscillation parameters		
Δm^2_{23}	0.0020 - 0.0027 eV^2	+6.7/-2.3
$\sin^2 2\theta_{23}$	0.93 - 1.00	-1.3
$\sin^2 2\theta_{13}$	0.0 - 0.15	-30.4

Table 7.11: Summary of systematic uncertainties in solar activity. Estimated uncertainty and the best-fit value are listed for each error.

	uncertainty (%)	Best-fit (%)
(G) Systematic uncertainties in solar activity		
SK-I	0.2	0.1
SK-II	0.5	0.2

The systematic uncertainties are grouped into two; the one, which affects the expected number of ν_τ events and the other that could change the observed number of ν_τ events. For the expected ν_τ signals, the systematic errors in atmospheric neutrino flux, neutrino interactions, and FC event selection are considered. These errors are also considered in the Super-K atmospheric neutrino oscillation analyses [47, 46, 48]. All error terms except for those affecting Sub-GeV, PC, and upward-going muon events are considered since the data sample used in this analysis is only Multi-GeV events. However, in this estimation, the uncertainty in the absolute normalization is assumed to be 20% as mentioned in Section 7.8.1. In addition, the uncertainties related only to the present analysis such as the ν_τ cross section, ν_τ polarization, and the likelihood selection efficiency are taken into account. The dominant uncertainty is due to the ν_τ cross section ($\pm 25\%$) since the cross section depends on theoretical calculations.

In determining the systematic uncertainties for the observed number of ν_τ events, various effects such as flux in up/down, horizontal/vertical, K/π, and NC/CC ratio that could change the up-down asymmetry of the atmospheric neutrino background MC and the data are taken into account. The systematic errors due to uncertainties in the oscillation parameters, Δm^2_{23}, $\sin^2 2\theta_{23}$, and $\sin^2 2\theta_{13}$ are also considered. The systematic error from $\sin^2 2\theta_{13}$ is asymmetric

Table 7.12: Summary of systematic uncertainties for the expected number of ν_τ events (top) and for the observed number of ν_τ events (bottom). The best fit values for each error term is listed. The uncertainties, which are calculated separately for SK-I and SK-II, are indicated by (SK-I) or (SK-II).

Systematic uncertainties for expected ν_τ	Best-fit (%)	
Atmospheric ν Flux and ν interactions (18 error terms)	20.2	
Detector response (9 error terms)	2.8 (SK-I)	0.5 (SK-II)
Tau related:		
Tau neutrino cross section	25.0	
Tau lepton polarization	3.1	
Tau neutrino selection efficiency	0.4 (SK-I)	1.5 (SK-II)
LH selection efficiency	2.5 (SK-I)	2.3 (SK-II)
Total:	32.5 (SK-I)	32.4 (SK-II)

Systematic uncertainties for observed ν_τ	Best-fit (%)	
Atmospheric ν Flux etc:		
Flux up/down ratio	8.6	
Flux horizontal/vertical ratio	4.7	
Flux K/π ratio	2.9	
NC/CC ratio	4.7	
Up/down symmetry of energy calibration	1.3 (SK-I)	0.3 (SK-II)
Oscillation parameters:		
$0.0020 < \Delta m^2_{23} < 0.0027\,\mathrm{eV}^2$	$+6.7/-2.3$	
$0.93 < \sin^2 2\theta_{23} < 1.00$	-1.3	
$0.0 < \sin^2 2\theta_{13} < 0.15$	-30.4	
Total (SK-I):	$+13.2/-32.5$	
Total (SK-II):	$+13.1/-32.5$	

because for non-zero θ_{13}, Multi-GeV electrons are expected to appear in the upward-going directions, which would be additional backgrounds for ν_τ signals. The dominant uncertainty is due to the uncertainty in $\sin^2 2\theta_{13}$.

Since the SK-I and SK-II detector responses are different, the systematic errors due to the event selections and reconstructions are treated independently and estimated separately.

The total systematic uncertainty for the expected number of ν_τ events is $\pm 32.5\%$ for SK-I and $\pm 32.4\%$ for SK-II. The total systematic uncertainty for the observed number of ν_τ events is $^{+13.2}_{-32.5}\%$ for SK-I and $^{+13.1}_{-32.5}\%$ for SK-II. If we assume $\theta_{13} = 0$, The total systematic uncertainty for the observed number of ν_τ events is $^{+13.2}_{-11.6}\%$ for SK-I and $^{+13.1}_{-11.6}\%$ for SK-II. Table 7.12 shows the summary of systematic uncertainties for the combined SK-I + SK-II fit.

7.9 Results

Combining the systematic errors with the fit result, I obtain a best-fit tau neutrino appearance signal of 162 ± 59 (stat.) $^{+21}_{-56}$ (sys.), which disfavors the no tau neutrino appearance hypothesis by 2.1 sigma. Assuming $\theta_{13} = 0$, tau neutrino appearance events are 162 ± 59 (stat.) $^{+21}_{-19}$ (2.6 sigma). The results are consistent with the expected number of tau neutrino events, 121 ± 39 (sys.) for $\Delta m^2 = 2.4 \times 10^{-3}$ eV^2, assuming the full mixing in $\nu_\mu \leftrightarrow \nu_\tau$ oscillations.

In summary, tau neutrino excess events have been observed in the upward-going direction in the Super-Kamiokande detector as expected (Figure 7.11) from a $\nu_\mu \leftrightarrow \nu_\tau$ oscillation hypothesis. Thus, the Super-Kamiokande atmospheric neutrino data are consistent with $\nu_\mu \leftrightarrow \nu_\tau$ oscillations.

Chapter 8

Conclusions and Future

8.1 Conclusions

Super-Kamiokande and several other experiments have established and confirmed atmospheric $\nu_\mu \leftrightarrow \nu_\tau$ oscillations by observing the disappearance of muon neutrinos in the atmospheric neutrino flux. The analysis presented in this thesis demonstrated a search for ν_τ appearance from $\nu_\mu \leftrightarrow \nu_\tau$ oscillations using Super-Kamiokande atmospheric neutrino data collected during SK-I period (1489.2 days exposure) and SK-II period (803.9 days exposure). Although detecting ν_τ appearance in Super-K is challenging, tau neutrino excess events of 162 ± 59 (stat.) $^{+21}_{-56}$ have been observed in the upward-going direction, which disfavors the no tau appearance hypothesis by 2.1 sigma. For $\theta_{13} = 0$, tau neutrino excess events are 162 ± 59 (stat.) $^{+21}_{-19}$ (2.6 sigma). The results are consistent with the expected number of tau neutrino events, 121 ± 39 (sys.) for $\Delta m^2 = 2.4 \times 10^{-3}$ eV^2, assuming the full mixing in $\nu_\mu \leftrightarrow \nu_\tau$ oscillations. The results confirm that the Super-Kamiokande atmospheric neutrino data are consistent with $\nu_\mu \leftrightarrow \nu_\tau$ oscillations.

8.2 Future

A large fraction of the systematic uncertainties in this analysis originates from the absolute flux of the atmospheric neutrinos, tau cross sections, and the uncertainty in the mixing angle, θ_{13}. Although the uncertainties from the absolute flux and tau cross sections could not be improved easily without experimental measurements, the uncertainty in θ_{13} can be improved by upcoming neutrino experiments, which measure θ_{13}, such as Double-CHOOZ [183], Daya

Bay [184] reactor experiments, and T2K [185] [1] long-baseline experiment. It is expected that the current limit of $\sin^2 2\theta_{13}$ will be improved by one order of magnitude.

Also, the 3rd phase of the Super-Kamiokande experiment, Super-Kamiokande-III or SK-III, has been operating for data-taking since June 2006. The tau neutrino appearance analysis with SK-III data combined with SK-I and SK-II data will improve the statistical sensitivity.

An accelerator-based long-baseline experiment, CNGS-OPERA has started in 2006 to look for ν_τ appearance in the ν_μ beams by detecting the tau leptons directly [186]. The ν_μ beams are produced at CERN and delivered to the OPERA detector in the Gran Sasso Laboratory in Italy. The detector utilizes the same technique used in the DONUT experiment for the first direct observation of the ν_τ [6]. In 5 years of data-taking, 10 - 15 ν_τ signals are expected with a very small background of less than one.

For the distant future, the next generation underground water Cherenkov detectors with Mega-ton class volume such as UNO [187, 188] in the US, Hyper-Kamiokande [189] in Japan, and Memphys [190] in France have been proposed. Since the fiducial volume of these proposed detector is about 20 times as large as that of the Super-K, the statistics of the expected ν_τ signals will be sufficient. The rough estimate of the expected number of tau neutrinos per year would be ~ 400 events.

Even though the neutrino oscillations have been established in the last decade, there are still many questions to be answered and parameters to be measured experimentally. The mixing angles and Δm^2's (with their sings) will have to be measured very precisely, and the neutrino cross sections have to be determined with better accuracy. CP violation in the neutrino sector has to be studies. Also, the neutrino masses need to be measured. Currently, there are several on-going neutrino experiments around the world, and in the next coming years, a few new experiments will start. There are many proposed future experiments. The field of neutrino physics will remain very exciting.

[1] Stony Brook NN Group is one of the leading US institutions in the T2K collaboration.

Appendix A

Super-Kamiokande Accident and SK-II and SK-III

A.1 Super-Kamiokande Accident

Super-Kamiokande was shutdown for the maintenance and upgrade work to replace dead PMTs in July, 2001, and the upgrade work was completed in September, 2001. While refilling the Super-K tank on November 12, 2001, one ID PMT on the bottom of the tank imploded, which triggered a cascade of implosions. About 60 % of the ID and OD PMTs in the detector were destroyed. The water level in the tank was up to 3/4 height of the detector, and most of destroyed PMTs were more than 5 meters below the water surface. A summary of damaged to the ID and OD are listed in Table A.1 and Table A.2.

Table A.1: Summary of the damage in the ID of Super-Kamiokande

	Status
Dead PMTs	6,777 (out of 11,146 ID PMTs)
Live PMTs	4,369
Electronics	No damage
HV supply	No damage
Cables	Unknown
PMT support parts	Many damaged
Black sheet	Need replacement
Tank outer wall	Some leak (4.2 ton/hr)

Table A.2: Summary of the damage in the OD of Super-Kamiokande

	Status
Dead PMTs	1,100 (out of 1,885 OD PMTs)
Live PMTs	785
Electronics	No damage
HV supply	Slight damage
Cables	Unknown
PMT support parts	Many damaged
Wavelength shifter plates	700 damaged (out of 1,885)
Tyvek sheet	Need replacement

A.1.1 Cause

All possible causes of the initial PMT implosion were thoroughly investigated [191], and two possible candidate PMTs on the bottom of the ID were identified as the first imploded PMT. The investigation concluded that the cause of the implosion was due to small crack or slight damage made on one of those two PMTs during the upgrade work or in the process of installation and transportation.

The mechanics of chain reaction and propagation of shock wave triggered by an implosion of a single PMT was also investigated. A shock wave pressure generated from the implosion of the first PMT destroyed the neighbor PMTs. This was tested using 9 PMTs (in 3 by 3 lattice) placed at depth of 30 m in the Super-K tank. The experiment was done by destroying the PMT at the center, and using a fast camera, it was observed that all of the adjacent PMTs were destroyed by the shock wave caused by the implosion.

A.1.2 PMT case

To prevent a chain reaction of any implosion of an ID PMT, an acrylic cover was designed to encase all of ID PMTs. A clear 12 mm thick UV-transparent acrylic dome is put over the photo-cathode area of PMTs and the sides of PMTs are protected by the fiberglass shield with holes, which let water flow into the case freely. The tests showed that this acrylic cover defused the implosion shock wave and that PMTs around the imploded one were not damaged. In conclusion, this case can prevent the chain reaction to occur in a case of an implosion.

Table A.3: Super-Kamiokande I, II, and III. The calculated livetime is for atmospheric neutrino analyses.

	Super-K I	Super-K II	Super-K III
Period	Apr. 1996 - Jul. 2001	Dec. 2002 - Oct. 2005	Jul. 2006 -
Livetime	1489.2 days	803.9 days	-
# of ID PMTs	11146	5182	11129
PMT coverage	40 %	19 %	40 %
# of OD PMTs	1885	1885	1885
Acrylic Shields	No	Yes	Yes

A.2 Super-Kamiokande-II

After the accident, the reconstruction of the detector was started in April, 2002. Since the ID PMTs are custom-made and it was not possible to produce enough ID PMTs in a short period of time, the detector was rebuilt with temporarily reduced PMT coverage in the ID (47 % of Super-Kamiokande-I). However, all OD PMTs and the wavelength shifter plates were replaced.

The data-taking resumed in December 2002 as Super-Kamiokande II or SK-II. The Super-K atmospheric neutrino analyses are not affected by the reduced coverage since the neutrino energy is high enough for 20 % of photocathode-coverage in the ID.

SK-II has been operated until October 2005 and was stopped temporarily to restore the detector to the original photocathode-coverage.

A.3 Super-Kamiokande-III

In October, 2005, the Super-K detector was shutdown again for the installation of the PMTs to restore its original ID photo-coverage (40 %) of SK-I. All newly installed ID PMTs are encased in acrylic covers as done for SK-II. In April, 2006, water refilling started and completed in July, 2006. Since then, the detector has been running as Super-Kamiokande III or SK-III.

Table A.3 summarizes the data-taking period, the number of ID and OD PMTs, PMT coverage for SK-I, SK-II and SK-III.

Appendix B

Energy Flow Analysis

In the energy flow analysis, the ID detector is divided into solid angle bins, which are uniformly distributed on a unit sphere. There are several ways to divide a unit sphere into uniform area bins. In this analysis, a binning method "geodesic binning" based on an icosahedron is used. Then, the charge flux going to each geodesic bin can be calculated from the Cherenkov light of an event. The energy flow is deconvolved with the charge flux and Cherenkov patterns, and the event shape variables are calculated. This section describes how this is conducted [192].

B.1 Geodesic binning

Geodesic bins are constructed from vertices of an icosahedron. An icosahedron has 12 vertices and 20 faces, which are equilateral triangles. In geodesic binning, more vertices can be created by adding a new vertex at the middle of each edge, and adding new edges between the neighboring vertices as shown in Figure B.1 and Figure B.2. This subdivides each of the original faces into 4 new isosceles triangles which can be further subdivided. The new geodesic can be characterized by the number of subdivisions (referred to as "splits").

Each vertex of a geodesic is characterized by a unit direction $\vec{d}_i$ and is at the center of a small region of solid angle (a geodesic bin). The analysis for SK-I and SK-II uses geodesic bins with four splits and three splits, respectively.

B.1.1 Charge Flux

Using the geodesic binning, the PMT coverage and the charge in each geodesic bin are calculated. All PMTs (both hit PMTs and PMTs that did not receive light) are considered. Then, the "charge flux" (Φ) and the uncertainty

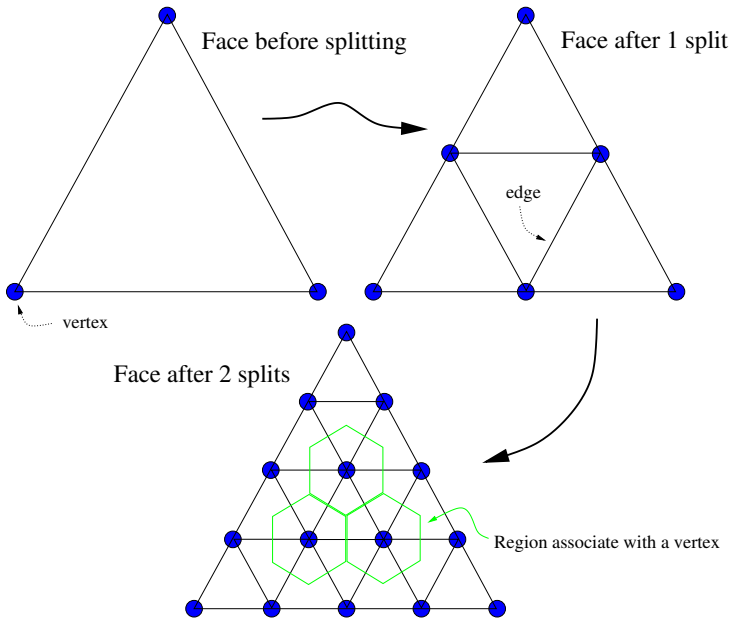

Figure B.1: Example of subdivision of one face with two splits. Each vertex represents each direction.

on the flux (σ_Φ) can be calculated for each bin.

For the bins without any PMT, the amount of light going in those directions can be estimated using neighboring bins to avoid the division by zero in the calculations. The estimated flux is then assigned a large uncertainty.

B.2 Energy Flow

In standard analyses in Super-K, the number of Cherenkov rings in an event is counted during the event reconstruction process, and the momentum of a charged particle is calculated based on the Cherenkov rings found. In this analysis, instead of finding Cherenkov rings, the energy flow of an event is calculated with Cherenkov pattern using the deconvolution :

$$\Phi(\vec{\omega}) = \int_{4\pi} R(\vec{\omega} - \vec{\omega}')\mathcal{P}(\vec{\omega}')d\vec{\omega}'. \tag{B.1}$$

where $\Phi(\vec{\omega})$ is the amount of Cherenkov light going in the direction of $\vec{\omega}$, $R(\delta\theta) = R(\vec{\omega} - \vec{\omega}')$ is the shape of the Cherenkov ring for a particle as a function of the opening angle with respect to the particle direction, $\mathcal{P}(\vec{\omega})$ is

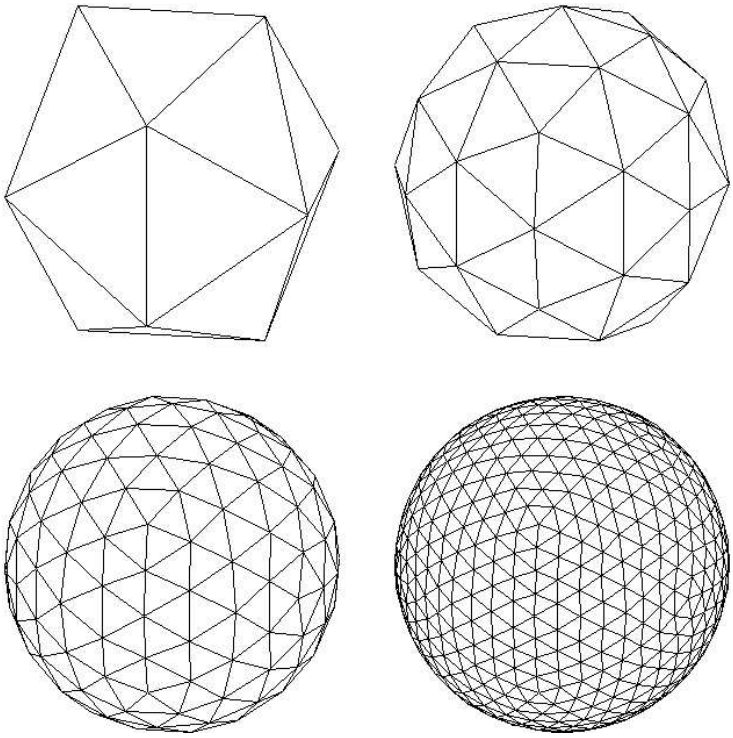

Figure B.2: Example of subdivision of an icosahedron.

the energy flow in the direction of $\vec{\omega}$. As described in Section B.1.1, $\Phi(\vec{\omega})$ can be calculated, and $R(\delta\theta)$ is a know function if we assume a charged particle is an electron.

The energy flow of an event can be obtained by inverting equation B.1. In practice, this integral can be written as a sum :

$$\vec{\Phi} = \Phi_i = \sum_j R_{ij}\mathcal{P}_j = \mathbf{R}\cdot\vec{\mathcal{P}} \tag{B.2}$$

where Φ_i is the charge flux in i-th geodesic bin, R_{ij} is the fraction of charge expected in i-th bin from a Cherenkov ring going in the direction of j-th bin (the matrix is symmetric), and the sum of the energy flow is the visible energy (E_{vis}) :

$$E_{vis} = \sum_i \mathcal{P}_i \tag{B.3}$$

Standard numerical techniques can be use to solve a set of linear equations (Eq. B.2) by minimizing the χ^2 :

$$\chi^2 = \sum_i \kappa_i(\Phi_i - \sum_j R_{ij}\mathcal{P}_j)^2 \tag{B.4}$$

where κ_i is any set of non-zero constants, but it is convenient to take $\kappa_i = 1/\sigma_{\Phi_i}$. For the minimization of χ^2, by defining :

$$\mathbf{A} = A_{ij} = \frac{R_{ij}}{\sigma_{\Phi_i}} \tag{B.5}$$

$$\vec{b} = b_i = \frac{\Phi_i}{\sigma_{\Phi_i}}, \tag{B.6}$$

Eq. B.4 can be written as :

$$\chi^2 = (\mathbf{A}\cdot\vec{\mathcal{P}} - \vec{b})^2, \tag{B.7}$$

which is minimized when

$$\frac{1}{2}\nabla\chi^2 = \mathbf{A}^T\cdot\mathbf{A}\cdot\vec{\mathcal{P}} - \mathbf{A}^T\cdot\vec{b} \tag{B.8}$$

The matrix $\mathbf{A}$ is referred as the *design matrix*. Eq. B.8 defines a sparse linear system, which is solved using the conjugate gradient method given in Numerical Recipes [193].

Although there is an exact solution for $\vec{\mathcal{P}}$, some elements of $\vec{\mathcal{P}}$ can become negative, but the negative values do not have physical meanings. This can

be handled by setting any negative element of $\vec{\mathcal{P}}$ to zero and eliminating the corresponding column from **A**. Eq. B.8 is then solved with the new design matrix. This procedure is repeated until all elements of $\vec{\mathcal{P}}$ are found to be positive. The elements of the energy flow, $\mathcal{P}_i$, represent the momentum of a massless particle going in directions $\vec{d}_i$, and the momentum of a particle is given by:

$$\vec{p}_i = \mathcal{P}_i \vec{d}_i \tag{B.9}$$

$$\vec{p} = \sum_i \vec{p}_i \tag{B.10}$$

B.3 Event Shape Variables

The *sphericity* can be derived from the sphericity tensor (or energy-momentum tensor) given by [132, 176]:

$$S^{ab} = \frac{\sum_i p_i^a p_i^b}{\sum_i p_i^2} \tag{B.11}$$

where a and b are the components of x, y, and z coordinates and the index i is for each particle. By diagonalizing the tensor S^{ab}, three eigenvalues ($\lambda_1 \geq \lambda_2 \geq \lambda_3$ with $\lambda_1 + \lambda_2 + \lambda_3 = 1$) and three eigenvectors ($\vec{s}_1, \vec{s}_2, \vec{s}_3$) are obtained:

The sphericity of an event is then defined as:

$$S = \frac{3}{2}(\lambda_2 + \lambda_3), \qquad 0 \leq S \leq 1 \tag{B.12}$$

The sphericity is a measure of roundness of an event and equals one if the event is spherically symmetric. The eigenvector $\vec{s}_1$ is called the sphericity axes, and the eigenvectors $\vec{s}_1$ and $\vec{s}_2$ spans the sphericity event plane, which usually contains most of the momentum of the event.

Another event shape variable, aplanarity, (which was used in an old tau neutrino appearance analysis but is not used in the present analysis) is defined as:

$$A = \frac{3}{2}\lambda_3, \qquad 0 \leq A \leq \frac{1}{2} \tag{B.13}$$

The aplanarity A measures the transverse momentum component out of the even plane defined by the eigenvectors $\vec{s}_1$ and $\vec{s}_2$ and equals 0 if the event is planar.

The sphericity and aplanarity have the quadratic momentum dependence. The particles with higher momentum are weighted heavily. Both are not Lorentz invariant.

Bibliography

[1] W. Pauli, in Open Letter to Radioactive Ladies and Gentleman (1930).

[2] F. Reines and C.L. Cowan, Nature **178**, 446 (1956).

[3] E. Fermi, Z. Physik, **88**, 161 (1934).

[4] C. L. Cowan, F. Reines, F. B. Harrison, H. W. Kruse and A. D. McGuire, Science **124**, 103 (1956).

[5] M. L. Perl *et al.*, Phys. Rev. Lett. **35**, 1489 (1975).

[6] K. Kodama *et al.*, [The DONUT Collaboration], Phys. Lett. B **504**, 218 (2001).

[7] R. Davis, Harmer and K. C. Hoffman, Phys. Rev. Lett. **21**, 1205 (1968).

[8] K. S. Hirata *et al.*, [The Kamiokande Collaboration], Phys. Rev. Lett. **58**, 1490 (1987).

[9] K. S. Hirata *et al.*, [The Kamiokande Collaboration], Phys. Rev. D **38**, 448 (1988).

[10] R. M. Bionta *et al.*, [The IMB Collaboration], Phys. Rev. Lett. **58**, 1494 (1987).

[11] C. B. Bratton *et al.*, [The IMB Collaboration], Phys. Rev. D **37**, 3361 (1988).

[12] W. M. Yao *et al.*, [Particle Data Group], J. Phys. G **33**, 1 (2006). (http://pdg.lbl.gov)

[13] M. Goldhaber *et al.*, Phys. Rev. **109**, 1015 (1958).

[14] C. Weinheimer, hep-ex/0210050.

[15] C. Weinheimer *et al.*, [Mainz experiment] Eur. Phys. J. C **40**, 447 (2005).

[16] K. Assamagan *et al.*, Phys. Rev. D **53**, 6065 (1996).

[17] J. M. Roney, Nucl. Phys. Proc. Suppl. **91** 287 (2001).

[18] U. Seljak *et al.*, Phys. Rev. D **71**, 103515 (2005).

[19] B. Pontecorvo, Sov. Phys. JETP. **6** 429 (1957). Sov. Phys. JETP. **7** 172 (1958).

[20] Z. Maki, M. Nakagawa, and S. Sakata, Prog. Theor. Phys. **28** 870 (1962).

[21] B. Pontecorvo, Zh. Eksp. Teor. Fiz. **53** 1717 (1967). Sov. Phys. JETP **26** 984 (1968).

[22] D. Casper *et al.*, [The IMB Collaboration], Phys. Rev. Lett. **66**, 2561 (1991).

[23] R. Becker-Szendy *et al.*, [The IMB Collaboration], Phys. Rev. D **46**, 3720 (1992).

[24] K. S. Hirata *et al.*, [The Kamiokande Collaboration], Phys. Lett. B **205**, 416 (1988).

[25] K. S. Hirata *et al.*, [The Kamiokande Collaboration], Phys. Lett. B **280**, 146 (1992).

[26] M. Aglietta *et al.*, [NUSEX Collaboration] Euro. Phys. Lett. **8**, 611 (1989).

[27] K. Daum *et al.*, [The Frejus Collaboration] Z. Phys. C **66**, 417 (1995).

[28] W. W .M. Allison *et al.*, [The Soudan 2 Collaboration], Phys. Lett. B **391**, 491 (1997).

[29] W. W .M. Allison *et al.*, [The Soudan 2 Collaboration], Phys. Lett. B **449**, 137 (1999).

[30] Y. Fukuda *et al.*, [The Kamiokande Collaboration], Phys. Lett. B **335**, 237 (1994).

[31] S. Hatakeyama *et al.*, [The Kamiokande Collaboration], Phys. Rev. Lett. **81**, 2016 (1998).

[32] M. Ambrosio *et al.*, [The MACRO Collaboration], Phys. Lett. B **434**, 451 (1998).

[33] M. Ambrosio *et al.*, [The MACRO Collaboration], Phys. Lett. B **478**, 5 (2000).

[34] W. W. M. Allison *et al.*, [The Soudan 2 Collaboration], Phys. Rev. D **72**, 052005 (2005).

[35] M. Ambrosio *et al.*, [The MACRO Collaboration], Phys. Lett. B **566**, 35 (2003).

[36] M. Sanchez *et al.*, [The Soudan 2 Collaboration], Phys. Rev. D **68**, 113004 (2003).

[37] M. Ambrosio *et al.*, [The MACRO Collaboration], Eur. Phys. J. C **36**, 323 (2004).

[38] P. Adamson *et al.*, [The MINOS Collaboration], Phys. Rev. D **73**, 072002 (2006).

[39] M. H. Ann *et al.*, [The K2K Collaboration], Phys. Rev. D **74**, 072003 (2006).

[40] D. G. Michael *et al.*, [The MINOS Collaboration], Phys. Rev. Lett. **97**, 191801 (2006).

[41] Y. Fukuda *et al.*, [The Super-Kamiokande Collaboration], Phys. Lett. B **433**, 9 (1998).

[42] Y. Fukuda *et al.*, [The Super-Kamiokande Collaboration], Phys. Lett. B **436**, 33 (1998).

[43] Y. Fukuda *et al.*, [The Super-Kamiokande Collaboration], Phys. Rev. Lett. **82**, 2644 (1999).

[44] Y. Fukuda *et al.*, [The Super-Kamiokande Collaboration], Phys. Lett. B **467**, 185 (1999).

[45] Y. Fukuda *et al.*, [The Super-Kamiokande Collaboration], Phys. Rev. Lett. **81**, 1562 (1998).

[46] Y. Ashie *et al.* [The Super-Kamiokande Collaboration], Phys. Rev. D **71**, 112005 (2005).

[47] M. Ishitsuka, *L/E Analysis of the atmospheric neutrino data from Super-Kamiokande* PhD thesis, University of Tokyo (2004).

[48] H. Seo, *A Measurement of $\nu_\mu \leftrightarrow \nu_\tau$ Oscillation Parameters Using Atmospheric Neutrino Observed in Super Kamiokande-I and Super Kamiokande-II* PhD Thesis, Sungkyunkwan University (2006).

[49] Y. Ashie *et al.*, [The Super-Kamiokande Collaboration], Phys. Rev. Lett. **93**, 101801 (2004).

[50] S. Fukuda *et al.* [The Super-Kamiokande Collaboration], Phys. Rev. Lett. **85**, 3999 (2000).

[51] P. A. Cherenkov, Doklady Akad. Nauk SSSR **2**, 451 (1934).

[52] I. Frank and I.Tamm, C. R. Acad. Sci. USSR **14**, 109 (1937).

[53] J. D. Jackson, *Classical Electrodynamics, Second Edition*. John Wiley & Sons (1975).

[54] E. Segrè, *Nuclei and Particles, Second Edition*. Benjamin/Cummings Publishing Company (1977).

[55] Becker-Szendy, *et al.*, Nucl. Instrum. and Methods. A **324**, 363 (1993).

[56] H. Kume *et al.*, Nucl. Inst. and Meth. A **205**, 443 (1983).

[57] A. Suzuki *et al.*, Nucl. Inst. and Meth. A **329**, 299 (1993).

[58] S. Fukuda *et al.*, [The Super-Kamiokande Collaboration], Nucl. Inst. Meth. Phys. Res. Sect. A **501**, 418 (2003).

[59] Y. Takeuchi *et al.*, Nucl. Inst. Meth. Phys. Res. A **421**, 334 (1999).

[60] Y. Takeuchi *et al.*, [The Super-Kamiokande Collaboration], Phys. Lett. **452**, 418 (1999).

[61] C. Mitsuda *et al.*, [The Super-Kamiokande Collaboration], Nucl. Inst. Meth. Phys. Res. A **497**, 414 (2003).

[62] H. Ikeda *et al.*, Nucl. Inst. and Meth. A **320**, 310 (1992).

[63] T. Tanimori *et al.*, IEEE Trans. Nucl. Sci. **NS-36**, 497 (1989).

[64] KEK Data Acquisition Development Working Group, *TKO Specification*, KEK Report 85-10 (1985).

[65] M. Shiozawa, *Data Acquisition System for the Super-Kamiokande experiment* Master Thesis (in Japanese), University of Tokyo (1994).

[66] J. George, *Experimental Study of the Atmospheric ν_μ / ν_e Ratio in the Multi-GeV Energy Range* PhD Thesis, University of Washington (1998).

[67] H. Berns. Super-K OD DAQ - GPS subsystem [online]. Available from: http://neutrino.phys.washington.edu/ 02dcberns/SUPERK/GPS/.

[68] H. Nishihama, *Development of Flash ADC Modules for Super-Kamiokande* Master Thesis, Tokyo Institute of Technology (2002).

[69] R. Nishimura, Master Thesis (in Japanese), Tokyo Institute of Technology (2003).

[70] T. Harada, Master Thesis (in Japanese), Tokyo Institute of Technology (2004).

[71] T. Koike, Master Thesis (in Japanese), Nagoya University (2007).

[72] *The ZEBRA Systen*, CERN Program Library Long Writeups Q100/Q101.

[73] M. Yamada *et al.*, Phys. Rev. D **44**, 617 (1991).

[74] T. Suzuki, D. F. Measday, and J. P. Roalsvig, Phys. Rev. C **35**, 2212 (1987).

[75] M. Nakahata *et al.*, [The Super-Kamiokande Collaboration], Nucl. Inst. Meth. Phys. Res. Sect. A **421**, 113 (1999).

[76] E. Blaufuss *et al.*, [The Super-Kamiokande Collaboration], Nucl. Inst. Meth. Phys. Res. Sect. A **458**, 638 (2001).

[77] M. Honda *et al.*, Phys. Rev. D **52**, 4985 (1995).

[78] M. Honda *et al.*, Phys. Rev. D **64**, 053011 (2001).

[79] M. Honda *et al.*, Phys. Rev. D **70**, 043008 (2004).

[80] V. Agrawal *et al.*, Phys. Rev. D **53**, 1314 (1996).

[81] G. Barr *et al.*, Phys. Rev. D **70**, 0423006 (2004) and also private communication.

[82] G. Battistoni *et al.*, Astropart. Phys. **19** 269 (2003) [Erratum-ibid. **19** 291 (2003)]. (http://www.mi.infn.it/ battist/neutrino.html)

[83] T. K. Gaisser and M. Honda, Annu. Rev. Part. Sci. **52**, 153 (2002)

[84] T. H. Johnson *et al.*, Phys. Rev. **43**, 307 (1933).

[85] A. H. Compton *et al.*, Phys. Rev. **43**, 387 (1933).

[86] T. Futagami *et al.*, [The Super-Kamiokande Collaboration], Phys. Rev. Lett. **82**, 5194 (1999).

[87] W. R. Webber *et al.*, *Proceedings of the 20th International Cosmic Ray Conference* (1987).

[88] P. Pappini *et al.*, [MASS Collaboration], *Proceedings of the 23rd International Cosmic Ray Conference* (1993).

[89] E. S. Seo *et al.*, [LEAP Collaboration], Astrophys. J. **378** 763 (1991).

[90] W. Menn *et al.*, [IMAZX Collaboration], Astrophys. J. **533** 281 (2000).

[91] M. Boezio *et al.*, [CAPRICE Collaboration], Astrophys. J. **518** 457 (1999).

[92] M. Boezio *et al.*, [CAPRICE Collaboration], Astrophys. Phys. **19** 583 (2003).

[93] T. Sanuki *et al.*, [BESS Collaboration], Astrophys. J. **545** 1135 (2000).

[94] S. Haino *et al.*, [BESS Collaboration], Phys. Lett. B **594** 35 (2004).

[95] J. Alcarez *et al.*, [AMS Collaboration], Phys. Lett. B **490** 27 (2000).

[96] M. J. Ryan, J. F. Ormes and V. K. Balasubrahmanyan, Phys. Rev. Lett. **28** 985 (1972).

[97] K. Asakamori *et al.*, [JACEE Collaboration], Astrophys. J. **502** 985 (1998).

[98] A. V. Apanasenko *et al.*, [RUNJOB Collaboration], Astropart. Phys. **16** 13 (2001).

[99] I. P. Ivanenko *et al.*, *Proceedings of the 23rd International Cosmic Ray Conference* (1993).

[100] Y. Kawamura *et al.*, Phys. Rev. D **40** 729 (1989).

[101] http://modelweb.gsfc.nasa.gov/atmos/usstandard.html.

[102] K. Hänssget and J. Ranft, Comput. Phys. **39** 37 (1986).

[103] S. Roesler, R. Engel, and J. Ranft, Phys. Rev. D **57** 2889 (1998).

[104] M. Motoki *et al.*, [BESS Collaboration], Astrophys. Phys. **19** 113 (2003).

[105] M. C. Conzalez-Garcia *et al.*, Phys. Rev. D **55**, 1297 (1997).

[106] L. Pasquali *et al.*, Phys. Rev. D **59**, 093003 (1999).

[107] Y. Hayato, Nucl. Phys. Proc. Suppl. **112**, 171 (2002).

[108] D. Casper, Nucl. Phys. Proc. Suppl. **112**, 161 (2002).

[109] C. H. Llewellyn Smith, Phys. Rep. **3**, 261 (1972).

[110] S. K. Singh and E. Oset, Phys. Rev. C **48**, 1246 (1993).

[111] M. H. Ahn *et al.*, [K2K Collaboration], Phys. Rev. Lett. **90**, 041801 (2003).

[112] R. A. Smith and E. J. Moniz, Nucl. Phys. B **43**, 605 (1972). [Erratum-ibid. B **101**, 547 (1975).]

[113] C. H. Albright *et al.*, Phys. Rev. D **14**, 1780 (1976).

[114] K. Abe *et al.*, Phys. Rev. Lett. **56**, 1107 (1986).

[115] S. Barish *et al.*, Phys. Rev. D **16**, 3103 (1977).

[116] S. Bonetti *et al.*, Nouvo Cimento **38**, 260 (1977).

[117] M. Pohl *et al.*, Nuovo Cimento **26**, 332 (1979);
N. Arimenise *et al.*, Nucl. Phys. B **152**, 365 (1979).

[118] A. S. Vovenko *et al.*, Yad. Fiz. **30**, 1014 (1979).

[119] S. Belikov *et al.*, Z. Phys. **320**, 625 (1985).

[120] J. Brunner *et al.*, Z. Phys. C **45**, 551 (1990).

[121] D. Rein and L. M. Sehgal, Ann. of Phys. **133**, 1780 (1981).

[122] D. Rein, Z. Phys. C **35**, 43 (1987).

[123] R. Feynman *et al.*, Phys. Rev. D **3**, 2706 (1971).

[124] S. K. Singh, M. J. Vicente-Vacas and E. Oset, Phys. Lett. B **416**, 23 (1998).

[125] G. Radecky *et al.*, Phys. Rev. D **25**, 116 (1982).

[126] T. Kitagaki *et al.*, Phys. Rev. D **34**, 2554 (1986).

[127] P. Allen *et al.*, Nucl. Phys. B **264**, 221 (1986).

[128] W. Lerche *et al.*, Phys. Lett. **4**, 510 (1978).

[129] D. Allisia *et al.*, Z. Phys. C **24**, 119 (1984).

[130] S. J. Barish *et al.*, Phys. Lett. B **91**, 161 (1980).

[131] M. Glück, E. Reya and A. Vogt, Z. Phys. D **57**, 433 (1995).

[132] T. Sjöstrand, Comput. Phys. Commun. **82**, 74 (1994).

[133] C. H. Albright and C. Jarlskog, Nucl Phys. B **84**, 467 (1975).

[134] M. Nakahata [Kamiokande Collaboration], J. Phys. Soc. Jpn. **55**, 2786 (1986).

[135] S. J. Barish *et al.*, Phys. Rev. D **17**, 1 (1978).

[136] H. Sarikko, Neutrino **507** (1979).

[137] S. Barlag *et al.*, Z. Phys. C **11**, 283 (1982).

[138] P. Musset and J. P. Vialle, Phys. Rep. C **39**, 1 (1978).

[139] J. E. Kim *et al.*, Rev. Mod. Phys. **53**, 211 (1981).

[140] V. B. Anikeev *et al.*, Z. Phys. C **70**, 39 (1996).

[141] P. S. Auchincloss *et al.*, Z. Phys. C **48**, 411 (1990).

[142] P. Berger *et al.*, Z. Phys. C **35**, 443 (1987).

[143] S. Campolillo *et al.*, Phys. Lett. **84B**, 281 (1979).

[144] O. Erriquez *et al.*, Phys. Lett. **89B**, 309 (1979).

[145] J. V. Allaby *et al.*, Z. Phys. C **38**, 403 (1988).

[146] C. Baltay *et al.*, Phys. Rev. Lett. **44**, 916 (1980). Z. Phys. C **2**, 187 (1979).

[147] D. C. Colley *et al.*, Z. Phys. C **2**, 187 (1979).

[148] N. J. Baker *et al.*, Phys. Rev. D **25**, 617 (1982).

[149] A. S. Vovenko *et al.*, Yad. Fiz. **30**, 187 (1979).

[150] D. B. MacFarlane *et al.*, Z. Phys. C **26**, 1 (1984).

[151] D. S. Baranov *et al.*, Phys. Lett. **81B**, 255 (1979).

[152] D. Rein and L. M. Sehgal, Nucl. Phys. B **233**, 29 (1983).

[153] R. Woods and D. Saxon, Phys. Rev. **95**, 577 (1954).

[154] L. Salcedo *et al.*, Nucl. Phys. A **484**, 557 (1988).

[155] G. Rowe *et al.*, Phys. Rev. C **18**, 584 (1978).

[156] D. Ashery *et al.*, Phys. Rev. C **23**, 2173 (1981).

[157] C. Ingram *et al.*, Phys. Rev. C **27**, 1578 (1983).

[158] B. R. Martin and M. K. Pidcock, Nuc. Phys. B **126**, 266 (1977).

[159] B. R. Martin and M. K. Pidcock, Nuc. Phys. B **126**, 285 (1977).

[160] J. S. Hyslop *et al.*, Phys. Rev. D **46**, 961 (1992).

[161] D. A. Sparrow, Proc. of the Conf. on the intersection between partivle and nuclear physics, 1019 (1984).

[162] H. W. Bertini *et al.*, Phys. Rev. C **6**, 631 (1972).

[163] S. J. Lindenbaum *et al.*, Phys. Rev. **105**, 1874 (1957).

[164] *GEANT Detector Description and Simulation Tool*, CERN Program Library W5013 (1994).

[165] C. Zeitnitz and T. A. Gabriel, Nucl. Inst. and Meth. A **349**, 106 (1994).

[166] M. Nakahata *et al.*, J. Phys. Soc. Jpn. **55**, 3786 (1986).

[167] E. Bracci *et al.*, CERN/HERA 72-1 (1972).

[168] A. S. Carrol *et al.*, Phys. Rev. C **14**, 635 (1976).

[169] ZEBRA, CERN Program Library Long Writeups Q100/Q101 (1995).

[170] S. Jadach *et al.*, Comput. Phys. Commun. **76**,361 (1993).

[171] K. Hagiwara *et al.*, Nucl. Phys. B **668**, 364 (2003).

[172] J. Kameda, *Detailed Studies of Neutrino Oscillation with Atmospheric Neutrinos of Wide Energy Range from 100 MeV to 1000 GeV in Super-Kamiokande* PhD Thesis, University of Tokyo (2002).

[173] E. R. Davies, *Machine Vision: Theory, Algorithms, Practicalities*, Academic Press, San Diego (1997).

[174] S. T. Clark, *Searches for Proton Decay with the Super-Kamiokande Detector*, PhD thesis, Boston University (2007).

[175] S. Kasuga *et al.*Phys. Lett. B **374**, 238 (1996).

[176] J. D. Bjorken and S. J. Brodsky, Phys. Rev. D **1**, 1416 (1970).

[177] G. Hanson *et al.*, Phys. Rev. Lett. **35**, 1609 (1975).

[178] B. Schwindling, J. Mansouli'e and O. Couet, MLPfit (2000), http://schwind.web.cern.ch/schwind/MLPfit.html.

[179] K. Abe *et al.*, [The Super-Kamiokande Collaboration] Phys. Rev. Lett. **97**, 171801 (2006).

[180] A. Bodek and U. K. Uang, Nucl. Phys. Proc. Suppl. **112**, 70 (2002).

[181] D. Casper, Nucl. Phys. Proc. Suppl. **112**, 161 (2002).

[182] M. Apollonio *et al.*, [The CHOOZ Collaboration], Eur. Phys. J. C **27**, 331 (2003).

[183] F. Ardellier *et al.*, [The Double Chooz Collaboration] hep-ex/0606025

[184] Daya Bay Collaboration, *Proposal, A Precision Measurement of the Neutrino Mixing Angle θ_{13} Using Reactor Antineutrinos At Daya Bay* hep-ex/0701029.

[185] Y. Yamada *et al.*, [The T2K Collaboration] Nucl. Phys. Proc. Suppl. **155** 28 (2006).

[186] R. Acquafredda *et al.*, [The OPERA Collaboration] New J. Phys. **8** 303 (2006).

[187] C. K. Jung, *Feasibility of a Next Generation Underground Water Cherenkov Detector: UNO*, Proceedings from the Next Generation Nucleon Decay and Neutrino Detector Workshop (2000).
E-print archive: hep-ex/0005046.

[188] R. J. Wilson, Presentation at Next generation Nucleon decay and Neutrino detectors 2006 : *UNO: Underground Nucleon Decay & Neutrino Observatory* (2006).
http://neutrino.phys.washington.edu/nnn06/

[189] K. Nakamura, Presentation at Next generation Nucleon decay and Neutrino detectors 2006 : *Hyper-Kamiokande* (2006).
http://neutrino.phys.washington.edu/nnn06/

[190] A. Bellefon, Presentation at Next generation Nucleon decay and Neutrino detectors 2006 : *MEMPHYS* (2006).
http://neutrino.phys.washington.edu/nnn06/

[191] Two reports on the Super-Kamiokande accident available at :
http://www-sk.icrr.u-tokyo.ac.jp/cause-committee/index-e.html
http://nngroup.physics.sunysb.edu/

[192] Clark McGrew, Notes on "Tau's Using Energy Flow Sphericity".

[193] W. Press *et al.*, "Numerical Recipes", Edition 1, (1986) Section 2.10 "Sparse Linear Systems".